# Coherent Coupling of a Single Molecule to a Fabry-Pérot Microcavity

Kohärente Kopplung zwischen einem einzelnen Molekül und einem Fabry-Pérot Mikroresonator

Der Naturwissenschaftlichen Fakultät der Friedrich-Alexander-Universität Erlangen-Nürnberg

zur

Erlangung des Doktorgrades Dr. rer. nat.

vorgelegt von

Daqing Wang aus Anhui, China

Als Dissertation genehmigt von der Naturwissenschaftlichen Fakultät der Friedrich-Alexander Universität Erlangen-Nürnberg

Tag der mündlichen Prüfung: 08.02.2019

Vorsitzender des Promotionsorgans: Prof. Dr. Georg Kreimer

Gutachter: Prof. Dr. Vahid Sandoghdar

Prof. Dr. Jean-Michel Raimond Prof. Dr. Arno Rauschenbeutel

#### **Abstract**

Efficient coupling of light with a quantum emitter is a central concept in the fundamentals of light-matter interaction and it is a prerequisite for deterministic quantum information transfer between distant nodes in a quantum network.

In this thesis, we demonstrate nearly perfect coupling of light with a polycyclic aromatic hydrocarbon (PAH) molecule enabled by a Fabry-Pérot microcavity. PAH is a species of solid-state emitter exhibiting remarkable optical properties when doped into an organic matrix and cooled to liquid helium temperatures. Previous experiments have explored coherent linear and nonlinear optical interactions with single PAH molecules. However, the coupling of the electronic transitions of a molecule to its vibrations and the phononic environment of the matrix introduces decoherence and has thus hampered its performance in those experiments. The vibronic and phononic couplings lead to a low branching ratio of the coherent 0-0 zero-phonon line (00ZPL) transition in the order of 30-50%, making a perfect photon-molecule coupling out of reach.

To tackle the problem, we employ an open Fabry-Pérot microcavity consisting of a planar mirror and a curved micromirror. The micromirror is fabricated using focused-ion-beam milling with a radius of curvature (ROC) in the range  $2.5 - 10 \,\mu\mathrm{m}$  on silicon or glass substrates. The small ROC allows the operation of an open, tunable and scannable microcavity with a mode volume as small as  $\lambda^3$ . We first perform room-temperature characterizations of a cavity with a micromirror fabricated on a silicon cantilever and demonstrate its capability in spatially resolved sensing of single gold nanoparticles.

To couple a single molecule to the cavity, we place a thin anthracene crystal doped with dibenzoterrylene molecules on the planar mirror. In combination with a dielectric-coated micromirror, a cavity with a quality factor of 120,000 is achieved. Passive and active vibration-isolation measures are implemented to maintain the stability of the cavity in a liquid-helium cryostat. As a result, we observe strong coherent interaction of the 00ZPL transition of a single molecule with the cavity mode at 4.2 Kelvin. The coupling accelerates the 00ZPL transition by a factor of 38, making it dominate over the decoherence rates. The branching ratio of the 00ZPL transition is modified to 95%, and the emission via the 00ZPL transmission couples to the cavity mode with an efficiency of 97%, i.e. the molecule is converted to a nearly perfect two-level system that couples to the cavity mode with near-unit efficiency.

The highly efficient light-matter coupling gives rise to several unprecedented effects in the molecular system. First, the resonant scattering of the molecule interferes destructively with the cavity field in the forward direction, attenuating the cavity transmission by more than 99%. Second, the molecule imprints a phase shift of up to  $\pm 66^{\circ}$  on a weak laser beam traversing the cavity. Third, the system responds nonlinearly at the level of single-photons, introducing strong correlations to the photons traversing the system. Furthermore, we demonstrate the efficient interaction of the system with single antibunched photons emitted by a second molecule.

The scanning, low mode volume microcavity demonstrated in this work is a promising platform for applications ranging from bio-sensing, optomechanics to cavity quantum electrodynamics. Our achievements in turning a molecule into a coherent two-level system pave the way for realizing quantum photonic networks based on an organic platform, where efficient linear and nonlinear optical interactions will be hosted by single molecules.

#### Zusammenfassung

Eine der elementarsten Problematiken im Forschungsfeld der Licht-Materie-Wechselwirkungen ist die effiziente Kopplung von Licht an einem einzelnen Quantenemitter. Eine hohe Effizienz ist insbesondere Voraussetzung für den deterministischen Transfer von Quanteninformation zwischen entfernten Knotenpunkten eines Quantennetzwerkes.

Die vorliegende Arbeit beschäftigt sich mit der nahezu perfekten Kopplung von Licht und einem einzelnen organischen Farbstoffmolekül mithilfe eines Fabry-Pérot Mikroresonators. Die verwendeten Farbstoffmoleküle entstammen der Gruppe der polyzyklischen aromatischen Kohlenwasserstoffe (PAK), welche bemerkenswerte optische Eigenschaften besitzen, wenn sie in eine organische Matrix eingebettet und auf eine Temperatur von wenigen Kelvin abgekühlt werden. In früheren Experimenten wurde die kohärente lineare und nichtlineare optische Wechselwirkung mit einzelnen PAK-Molekülen untersucht. Die dort beobachteten Effekte waren allerdings nur schwach ausgeprägt, da der elektronisch angeregte Zustand an viele Vibrationsniveaus des Grundzustandes koppelt und diese wiederum mit der phononische Umgebung der Matrix wechselwirken. Die damit verbundene Dekohärenz reduziert den resonanten Wechselwirkungsquerschnitt. Das Verhältnis der 00-Nullphononenlinie zu allen anderen möglichen Emissionspfaden liegt bei den verwendeten PAK Molekülen zwischen 30 und 50%. Aus diesem Grund ist auch bei idealen experimentellen Bedingungen eine perfekte Licht-Molekül-Kopplung unmöglich.

Durch Verwenden eines Fabry-Pérot Mikroresonator können diese fundamentalen Probleme jedoch gelöst werden. Der Resonantor besteht aus einem planen und einem gekrümmten Mikrospiegel. Der gekrümmte Spiegel wurde mit Hilfe eines fokussierten Ionenstrahls auf Silizium- oder Glassubstraten hergestellt. Der Krümmungsradius liegt zwischen 2.5 und 10 Mikrometern. Solch kleine Krümmungsradien erlauben die Realisierung extrem kleiner Modenvolumen ohne die Vorteile einer offenen und durchstimmbaren Bauweise aufgeben zu müssen. Dies wird anhand eines Resonators mit Silizium Cantilever als Substrat für den Mikrospiegel gezeigt und seine Funktionstüchtigkeit mit der räumlich aufgelösten Detektion eines einzelnen Goldnanoteilchens demonstriert.

Um ein einzelnes Molekül an den Resonator zu koppeln, wird ein dünner Anthracenkristall, welcher mit Dibenzoterrylen Molekülen dotiert ist, auf den planaren Spiegel gelegt. In Kombination mit einem hochreflektierenden Mikrospiegel bildet sich ein Resonator mit einer Güte von 120,000. Passive und aktive Schwingungsisolation erlauben die mechanische Stabilität des Resonators auch bei Flüssig-Helium Temperaturen zu erhalten. So wird bei 4 Kelvin eine starke kohärente Wechselwirkung der 00-Nullphononenlinie des Moleküls mit der Resonatormode erreicht. Die Kopplung beschleunigt den Übergang der 00-Nullphononenlinie um den Faktor 38, so dass störende Dekohärenzprozesse eine

untergeordnete Rolle spielen. Dies zeigt sich darin, dass das Molekül nun mit 95%-iger Wahrscheinlichkeit auf dem Übergang der 00-Nullphononenlinie emittiert und diese Photonen mit einer Effizienz von 97% an die Resonatormode koppeln. Das Molekül wurde also in ein nahezu perfektes Zwei-Niveau-System verwandelt, welches äußerst effizient an die Resonatormode koppelt.

Die in dieser Arbeit erreichte hoch-effiziente Licht-Materie-Kopplung erlaubt es in diesem molekularen System einige sehr interessante Effekte zu beobachten. Zum einen interferiert das resonant gestreute Licht des Moleküls destruktiv mit dem Resonatorfeld in der Vorwärtsrichtung. Dies führt zu einer 99%-igen Abschwächung der Resonatortransmission. Zum anderen kann das Molekül die Phase eines schwachen Laserstrahls, welcher durch den Resonator geschickt wird um bis zu 66 Grad verschoben. Das System zeigt außerdem eine starke optische Nichtlinearität auf Einzel-Photonen Level. Dies führt zu starken Korrelationen unter Photonen die den Resonator durchlaufen. Am Ende der Arbeit wird schließlich gezeigt, dass das Molekül im Resonator auch stark mit echten einzelnen Photonen wechselwirkt, welche von einem zweiten Molekül in einem anderen Kryostaten erzeugt wurden.

Der in dieser Arbeit entwickelte, offene und verstimmbare Mikroresonator ist eine vielversprechende Plattform, welche in der Biosensorik, der Optomechanik und der Resonator Quantenelektrodynamik Verwendung finden kann. Die hier gezeigten Ergebnisse sind ein wichtiger Schritt für die Realisierung photonischer Quantennetzwerke auf Basis einer organischen Materialplattform, in denen die linearen und nichtlinearen optischen Wechselwirkungen von einzelnen Molekülen ausgenutzt werden.

# **Contents**

1	Intr	oducti	ion	1
<b>2</b>	The	oretic	al background	5
	2.1	Photo	physics of polycyclic aromatic hydrocarbons	6
	2.2	Cavity	y quantum electrodynamics	9
		2.2.1	The Purcell factor	9
		2.2.2	The Jaynes-Cummings Hamiltonian	12
		2.2.3	Quasi-eigenstate coalescence and strong coupling	14
	2.3	Coher	ent interaction of a molecule with a cavity mode	17
		2.3.1	Transmission and reflection spectra	17
		2.3.2	Purcell effect and Lamb shift	23
		2.3.3	Phase response	25
		2.3.4	Saturation of the system	27
	2.4	Photo	n statistics of the transmitted light	29
		2.4.1	Theoretical model	29
		2.4.2	Probability of two-photon transmission	31
3	Exp	erime	ntal platform	35
	3.1	Single	-molecule sample preparation and detection	36
		3.1.1	Sample preparation	36
		3.1.2	Single-molecule detection	38
	3.2	Cavity	y design	39
	3.3	Micro	mirror fabrication	42
		3.3.1	Focused-ion-beam machining	42
		3.3.2	Mirror coatings	45
	3.4	Room	-temperature setup	47
		3.4.1	Inverted microscope	47
		3.4.2	Room-temperature microcavity assembly	47
	3.5	Cryog	enic setup	49

**vi** Contents

		3.5.1	The cryostat	49		
		3.5.2	Cryogenic microscope	51		
		3.5.3	Low-temperature microcavity on the cryo-insert	54		
		3.5.4	Polarization-mode splitting and cross-polarized detection	57		
	3.6	Vibrat	tion control	58		
4	A c	lassica	l dipole in a microcavity	61		
	4.1	Chara	cterization of the cavity parameters	62		
		4.1.1	Spectra of the cavity	62		
		4.1.2	Mode volume	65		
	4.2	Sensin	g and imaging of single nanoparticles	67		
		4.2.1	Frequency shift by a single dipolar scatterer	67		
		4.2.2	Modifications of finesse	69		
5	Efficient coherent light-matter interaction in a microcavity 73					
	5.1	Coupli	ing of a single molecule to a low-finesse cavity	74		
		5.1.1	Identifying a molecule	74		
		5.1.2	Transmission spectra	76		
		5.1.3	Cavity QED-parameters	78		
	5.2	A high	n-finesse microcavity in the cryogenic environment	80		
		5.2.1	Parameters of the cavity at 4.2 Kelvin	80		
		5.2.2	Analyzing cavity vibration	81		
	5.3	Identif	fying a molecule in transmission	84		
	5.4	Resonant response of the molecule-cavity system				
	5.5	Cavity-QED parameters				
	5.6	Linew	idth modification and Lamb shift	87		
	5.7	Onset	of strong coupling	89		
	5.8	Phase-	-shift	92		
		5.8.1	A two-frequency interferometer	93		
		5.8.2	Experimental implementation	94		
6	Noi	nlinear	ity at the single-photon level	99		
	6.1	Saturation of the system				
	6.2	Photo	n statistics of the transmitted light	102		
		6.2.1	Resonant transmission: strong photon-bunching	102		
		6.2.2	Detuned transmission: from classical to non-classical fluctuations	104		
	6.3	Interfa	acing the molecule with single-photons	108		
7	Cor	nclusio	n and outlook	113		

Contents	vii
Bibliography	115
Acknowledgements	127
Appendix Nummerical simulations	129

viii Contents

# Chapter 1

## Introduction

A photon flies in, a two-level atom is excited. This physical picture is so simple and so fundamental that it appears in many introductory chapters on optics [1,2]. Although the excitation of electronic transitions with light has been studied extensively [3], to make a single photon interact deterministically with a single atom remains a very challenging task. Such a deterministic interaction represents the ultimate control over light-matter interaction and is a crucial prerequisite for realizing a quantum network, where flying photons carry information to bridge distant nodes containing matter qubits for the processing and storage of information [4,5].

Toward this aim, many efforts have been invested in searching for material systems with suitable level structures to facilitate a quantum interface between light and matter. Promising systems such as atoms [6–9] and ions [10–12] in the gas phase and quantum dots [13,14], color centers [15–17] and rare-earth ions [18–21] in the solid state have been identified. Even though these systems pose many interesting functionalities, their efficiencies remain mostly unsatisfactory. The limit to the efficiency traces back to the conversion efficiency of a flying photon to an atomic excitation, i.e. the simple physical picture we introduced at the beginning.

In this thesis, we focus on improving the coupling efficiency of light to an atom-like quantum system. Our system of choice is polycyclic aromatic hydrocarbon (PAH) molecules embedded in a solid-state matrix [22]. PAHs can serve as solid-state emitters with remarkable optical properties, such as near-unity quantum efficiency and indefinite photostability. In particular, they support lifetime-limited 0-0 zero-phonon lines (00ZPL) when cooled to liquid helium temperatures. However, like other emitters in the solid state [23, 24], the electronic transitions in a PAH molecule couple to its internal vibrations and the solid-state environment that surrounds it [22]. As a result,

the 00ZPL transition has a finite branching ratio of about 30% to 50%, limiting the coherent interaction efficiency with a light field.

To overcome the decoherence induced by the vibronic coupling, our method of choice is to selectively enhance the 00ZPL transition using an optical microcavity [25] with a mode volume of a few  $\lambda^3$ . Utilizing the Purcell effect [26], the coherent emission into the 00ZPL can be enhanced by a factor of 40 to dominate over the incoherent transitions, thus converting the molecule to a coherent two-level system. The strong Purcell-enhancement also reshapes the emission pattern of the molecule, enabling a near-unity efficiency with the cavity mode. We note that the use of a microcavity allows us to accelerate an optical transition from megahertz to gigahertz rates without reaching the strong coupling regime [27,28], such that the emission process is greatly enhanced but not limited by the bandwidth of the cavity. This regime is optimal for achieving fast information extraction from the material qubits [21,29–33]. It is thus distinct from the conventional experiments in cavity quantum electrodynamics (cavity QED) using macroscopic cavities, where the strong coupling regime is reached primarily by increasing the photon lifetime in the cavity [34,35].

This thesis is organized as follows. In chapter 2, we present the theoretical background for describing the interaction of a PAH molecule with an optical cavity. We start by introducing the photophysical model of PAH molecules and the fundamentals of cavity QED. An analytical model is set up to derive the transmission spectrum of a coupled molecule-cavity system. In the last section, we discuss the modification of the photon statistics of a laser beam using the coupled system.

Chapter 3 presents the experimental platform. We start by introducing the vaporphase growth of single-molecule doped organic crystals and the experimental methods of single-molecule detection. In section 3.2, we present the design of the cavity and outline the key parameters for achieving a small mode volume. In section 3.3, we explain the principle of focused-ion-beam milling and the fabrication of micromirrors. The different types of coatings applied on the mirrors are also discussed in this section. In the sections 3.4 and 3.5, we introduce the three generations of microcavity assemblies and the optical setups for room-temperature and low-temperature experiments. The experimental setups were developed in an incremental way. The first generation of the microcavity was built for room-temperature operation with the capability of performing spatially resolved nanoparticle sensing. After the room-temperature characterizations, a second cavity assembly was built for cryogenic operations of a cavity with finesse in the order of 200. The third generation has an improved mechanical stability, which allowed the low-temperature operation of a cavity with finesse up to 19,000. In the last

section of this chapter, we outline the measures implemented for passive and active vibration control, which enables the operation of the microcavities in the cryostat.

In chapter 4, we present the characterization of a tunable and scannable Fabry-Perót cavity with sub- $\lambda^3$  mode volume at room-temperature. We also demonstrate spatially resolved nanoparticle sensing using this cavity.

Chapter 5 reports on the observations of coherent interaction of a single molecule with a cavity mode at liquid helium temperatures. We first study the coupling of a molecule to a low-finesse cavity, where the molecule attenuates the transmission of the cavity by 38%. The following sections of the chapter focus on the coupling of a molecule with a high-finesse cavity. The interference of the molecular scattering with the cavity mode strongly modifies the transmission and reflection spectra of the cavity and leads to a large phase shift of a transmitted laser beam.

In chapter 6, we study the nonlinear response of the coupled molecule-cavity system at the single-photon level. The strong nonlinearity leads to modifications of the photon statistics of a weak laser beam. To move one step further towards deterministic singlephoton single-molecule interactions, we perform measurements on the molecule with single photons generated by a second molecule in a neighboring lab.

In the last chapter, we draw a brief conclusion and envision feasible experiments based on the developed experimental platform. We expect the system to be promising for hosting photon-photon interactions, for studying the coupling of a controlled number of emitters via the cavity mode and for enhancing the radiative properties of other species of solid-state emitters such as rare-earth ions.

## Chapter 2

# Theoretical background

In this chapter, we provide the theoretical background for modeling the interaction of a single polycyclic aromatic hydrocarbon (PAH) molecule with an optical microcavity. In section 2.1, we introduce the family of PAH molecules and their photophysical properties. The molecules can be approximated as two-level systems with an additional loss channel induced by the vibrational and phononic couplings of their electronic transitions. In section 2.2, we explain the basic formulations of cavity quantum electrodynamics. We start by deriving the Purcell factor using Fermi's golden rule and the local density of states. We introduce the Jaynes-Cummings Hamiltonian and analyze the eigenstates of the coupled system with and without dissipation. In section 2.3, we model the coupling of a PAH molecule to a single mode of a microcavity. We show that the coupling modifies the transmission and reflection spectra of the cavity and introduces changes in the linewidth and center frequency of the molecule. We also analyze the phase shift of the system on an incident laser beam and discuss the saturation behavior of the system in the nonlinear regime. In the last part of this chapter, we study the dynamic effects in the coupled system, which leads to modifications of the photon statistics of a laser beam traversing it.

## 2.1 Photophysics of polycyclic aromatic hydrocarbons

Polycyclic aromatic hydrocarbons (PAH) are a species of organic molecules which contain only carbon and hydrogen. Resembling cut-out pieces of a graphene sheet, PAH molecules are composed of multiple fused aromatic rings, in which the cyclic conjugated  $\pi$ -electrons can be excited via an optical transition [36]. The transition frequencies of PAHs range from ultraviolet to near infrared, depending on the structure of the molecule. Since the late 1980s, a number of experiments have shown that PAH molecules can behave favorably as single quantum emitters when embedded in organic matrices at liquid helium temperatures ( $T \leq 4.2 \,\mathrm{K}$ ) [22].

The commonly used PAH molecules for single-molecule studies are presented in the upper row of Fig. 2.1. The molecules are doped into an organic matrix with a larger optical band gap (see lower row in Fig. 2.1), such that the dopants act as optically active defect centers with a small concentration and can be detected via high-resolution microscopy and spectroscopy [22].

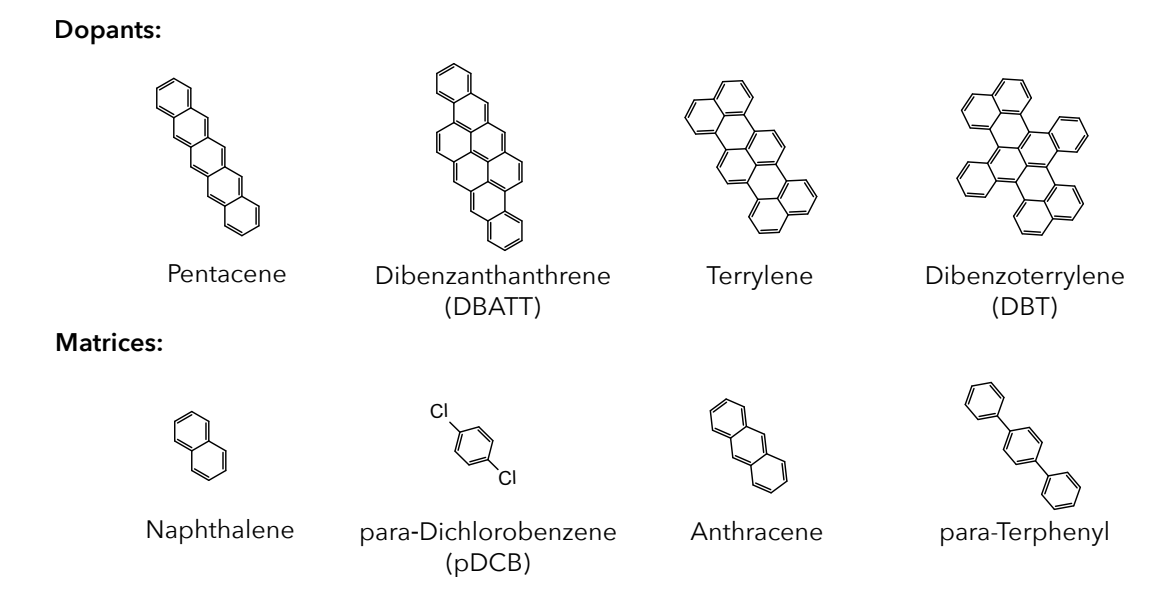


**Figure 2.1:** Molecular structures of commonly used PAH molecules (upper row) and hosting matrices (lower row) for single-molecule optical studies.

The energy levels of a PAH molecule involve electronic and vibrational states. As illustrated in Fig. 2.2 a, the electronic ground state  $|S_0\rangle$  of a PAH molecule is a singlet state, where the two electrons in the highest occupied molecular orbital are paired to give a total spin of zero. An electron in  $|S_0\rangle$  can be excited to the low-lying singlet

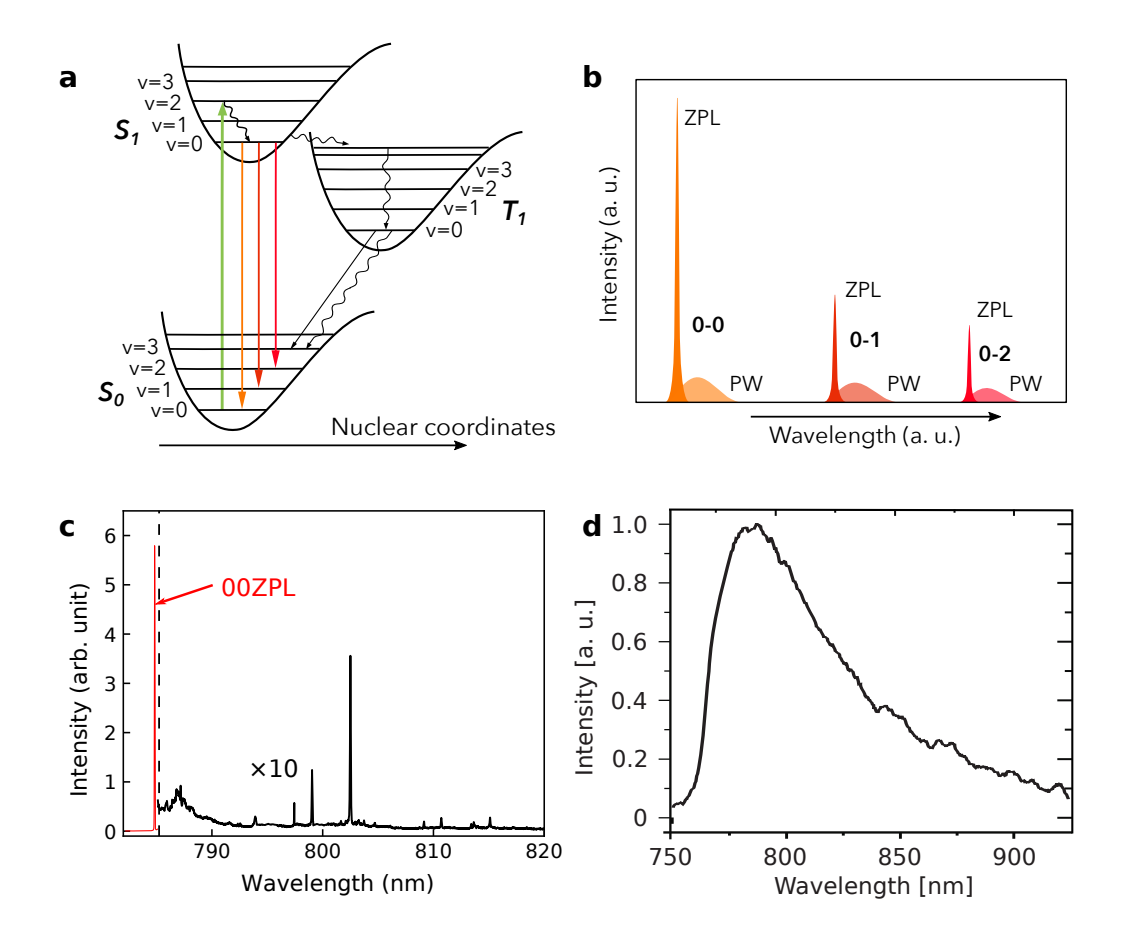


Figure 2.2: a, Schematic representation of the energy levels of a PAH molecule.  $S_0$ : singlet ground state;  $S_1$ : low-lying singlet excited state;  $T_1$ : low-lying triplet excited state. v represents the index of the vibrational sub-levels. The straight arrows denote optical transitions, while the curly arrows stand for non-radiative relaxations. b, Illustration of the emission spectrum from the  $|S_1, v = 0\rangle$  state. See text for details. c, Emission spectrum of a DBT molecule in an anthracene crystal at 4 Kelvin. d, Emission spectrum of a DBT molecule in an anthracene crystal at room temperature. Adopted from Ref. [37] with permission.

excited states  $|S_1\rangle$  via an optical transition (green arrow). A molecule also possesses a large number of vibrational modes, which couple to the electronic states and give rise to vibrational sub-levels. When the molecule is excited to a higher vibrational level of the electronic excited state  $|S_1, v \neq 0\rangle$ , it quickly relaxes non-radiatively to the lowest vibrational level  $|S_1, v = 0\rangle$ , following Kasha's rule [38]. From  $|S_1, v = 0\rangle$ , the molecule can decay to the  $|S_0, v = 0\rangle$  or  $|S_0, v \neq 0\rangle$  levels by emitting a photon. The photon emission process is called fluorescence and the probabilities of decaying to each of the ground-state sub-levels follow the Franck-Condon principle [39,40]. The optical transition connecting the  $|S_1, v = 0\rangle$  and  $|S_0, v = m\rangle$  levels is referred to as the 0-m zero-phonon-line (ZPL) with m = (0, 1, 2, ...). In particular, we denote the  $|S_0, v = 0\rangle$ 

to  $|S_1, v = 0\rangle$  transition as 00ZPL. Being surrounded by the solid-state matrix, the optical transitions are also coupled to the phononic modes of the lattice, giving rise to phonon wings associated with each of the ZPLs. Figure 2.2 **b** illustrates the emission spectrum of a molecule from the  $|S_1, v = 0\rangle$  state. The ZPLs appear as sharp peaks each accompanied by a broad phonon wing. Figure 2.2 **c** displays an emission spectrum from the  $|S_1, v = 0\rangle$  state of a dibenzoterrylene (DBT) molecule embedded in an anthracene crystal measured at 4K. The sharp peak at 784 nm corresponds to the 00ZPL transition. The Stokes-shifted ZPLs and the phonon wings are displayed in black. In comparison, an emission spectrum of a DBT molecule in the same matrix at room-temperature is presented in Fig. 2.2 **d**, where the spectrum broadened to about 60 nm due to the strong dephasing introduced by the thermal excitations in the matrix.

An important coefficient which we will come across often in this thesis is the branching ratio of the 00ZPL emission  $\alpha$ , which is defined as the decay rate from  $|S_1, v = 0\rangle$  to  $|S_0, v = 0\rangle$  normalized to the total decay rate from  $|S_1, v = 0\rangle$ :

$$\alpha = \frac{\gamma_{\text{zpl}}}{\gamma^0},\tag{2.1}$$

where  $\gamma_{\rm zpl}$  and  $\gamma^0$  denote the 00ZPL and total decay rates of  $|S_1, v = 0\rangle$ , respectively.

The transition between  $|S_0\rangle$  and  $|S_1\rangle$  is spin conserving. When an electron is excited to the singlet excited states, there is also a possibility that it undergoes a spin conversion and reaches a triplet state  $|T_1\rangle$  (see Fig. 2.2 a), where the electrons are unpaired and give a total spin of one. This process is called intersystem crossing (ISC) and normally results from spin-orbit coupling [36]. From  $|T_1\rangle$ , the molecule can decay to  $|S_0\rangle$  via another ISC process or by emitting a photon. The emission from  $|T_1\rangle$  to  $|S_0\rangle$  is called phosphorescence. We note that the ISC rate is molecule and host-matrix dependent. For systems like DBT molecules in anthracene crystals, the ISC rate can be as low as  $10^{-7}$  [41].

Despite the complex level structure, the molecule can be approximated as a two-level system when studying the resonant transition between  $|S_0, v = 0\rangle$  and  $|S_1, v = 0\rangle$ . This approximation is valid given the fast relaxations of the  $|S_0, v \neq 0\rangle$  levels and a negligible ISC rate. The incoherent decays to the  $|S_0, v \neq 0\rangle$  levels appear as a reduction of the scattering cross section in the classical treatment of light-matter interaction [42–44] and is considered an additional loss channel in the formulation of cavity quantum electrodynamics (see section 2.3).

## 2.2 Cavity quantum electrodynamics

The radiative property of a single quantum emitter depends on its surrounding electromagnetic environment. In free space, the excited state of a single emitter couples to vacuum fields of an infinite set of modes, giving rise to spontaneous emission at a rate described by the Einstein A coefficient [45, 46]. The situation is different when the emitter is placed in an optical cavity. The frequency selectivity of the cavity allows only a discrete set of electromagnetic modes and modifies the radiative property of the emitter inside [28, 34]. In this section, we introduce the theoretical background of cavity quantum electrodynamics (cavity QED), which describes the interaction of an atom-like quantum emitter with a single mode of a cavity.

#### 2.2.1 The Purcell factor

The first known reference to a cavity QED effect is the formulation by Edward M. Purcell in 1946 on the modification of spontaneous emission rate by a resonant circuit [26]. In his short paragraph in a conference proceedings, Purcell predicted that the nuclear magnetic transitions at radio frequencies could be enhanced via resonant coupling to an electrical circuit, by a factor of

$$F = \frac{3\lambda^3}{4\pi^2} \cdot \frac{Q}{V},\tag{2.2}$$

where  $\lambda$  is the transition wavelength. Q and V are the quality factor and the volume of the electrical circuit, respectively. The enhancement factor F is hence named the Purcell factor.

A simple but yet instructive derivation of the Purcell factor can be obtained using Fermi's golden rule. We follow the derivations in Ref. [2], considering a two-level emitter with a ground state  $|g\rangle$  and an excited state  $|e\rangle$  separated by  $\hbar\omega_0$  in energy. The spontaneous emission rate  $\gamma$  of the emitter can be calculated using Fermi's golden rule

$$\gamma = \frac{2\pi}{\hbar^2} |M_{eg}|^2 \rho(\omega_0) , \qquad (2.3)$$

where  $M_{eg}$  is the transition matrix element and  $\rho(\omega_0)$  is the density of states (DOS) of photons at the location of the emitter<sup>1</sup>. In free space, the photonic density of states

<sup>&</sup>lt;sup>1</sup>The initial and final states consist of both the states of the emitter and the photon. Since the final state of the electron is defined to be the ground state  $|g\rangle$ , after integrating over all the possible final states, only the photonic DOS is present.

 $\rho^0(\omega)$  as a function of frequency  $\omega$  is giving by

$$\rho^{0}(\omega) = \frac{\omega^{2} V_{0}}{\pi^{2} c^{3}}, \qquad (2.4)$$

where c is the speed of light in vacuum and  $V_0$  is a volume applied to free space for field quantization. The transition matrix element can be expressed as

$$M_{eg} = \langle -\boldsymbol{\mu}_{eg} \cdot \boldsymbol{E}_{\text{vac}} \rangle, \tag{2.5}$$

where  $\mu_{eg}$  is the dipole moment of the transition with amplitude  $\mu_{eg} = -e \cdot \langle g|x|e \rangle$ .  $\mathbf{E}_{\text{vac}}$  denotes the electric field of the vacuum modes [47] with amplitude

$$E_{\rm vac} = \left(\frac{\hbar\omega}{2\epsilon_0 V_0}\right)^{1/2} \,, \tag{2.6}$$

with  $\epsilon_0$  the vacuum electric permittivity. Since vacuum fields in free space have no preferential polarization, one needs to include a factor of 1/3 to account for the random orientation of the field with respect to the dipole. The expression of  $|M_{eg}|^2$  becomes:

$$|M_{eg}|^2 = \frac{\mu_{eg}^2 \hbar \omega}{6\epsilon_0 V_0} \,. \tag{2.7}$$

Combining Eqs. 2.3, 2.4 and 2.7, we arrive at the spontaneous emission rate in free space

$$\gamma^0 = \frac{\mu_{eg}^2 \omega_0^3}{3\pi \epsilon_0 \hbar c^3} \,. \tag{2.8}$$

We now calculate the spontaneous emission rate of a two-level emitter placed in the field maximum of a cavity. Assuming the cavity has only one resonance close to the transition frequency of the emitter, the DOS of the cavity mode seen by the emitter is

$$\rho'(\omega_0) = \frac{\kappa/(2\pi)}{(\omega_0 - \omega_c)^2 + (\kappa/2)^2},$$
(2.9)

which is a normalized Lorentzian function with center frequency  $\omega_c$  and full width at half maximum (FWHM)  $\kappa$ . In the expression of  $E_{\text{vac}}$  (see Eq. 2.6), the mode volume  $V_0$  should be replaced by the mode volume of the cavity V. For a cavity placed in vacuum, the mode volume can be calculated as

$$V = \frac{\int_{V_{\text{cav}}} \epsilon_0 |\mathbf{E}(\mathbf{r})|^2 d^3 \mathbf{r}}{\max[\epsilon_0 |\mathbf{E}(\mathbf{r})|^2]},$$
(2.10)

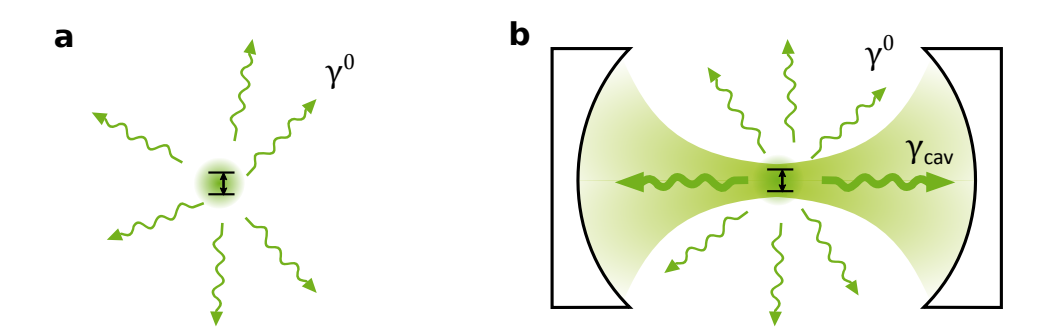


Figure 2.3: a, Spontaneous emission of a two-level system in free space. The direction of emission is random. The total emission rate is denoted as  $\gamma^0$ . b, Spontaneous emission of a two-level system in a cavity. The resonant coupling with the cavity enhances the emission rate into the cavity mode by an amount of  $\gamma_{\text{cav}}$ . The emission rate into free-space modes can be considered as unchanged.

where  $\mathbf{E}(\mathbf{r})$  stands for the electric field at point  $\mathbf{r}$  in the volume of the cavity  $V_{\text{cav}}$ . We also note that the electric field in the cavity can have a defined polarization aligned with the emitter, meaning that the factor of 1/3 can be omitted in the expression of  $|M_{eg}|^2$ . The modified spontaneous emission rate into the cavity mode  $\gamma_{\text{cav}}$  is then

$$\gamma_{\text{cav}} = \frac{2\mu_{eg}^2 Q}{\hbar \epsilon_0 V} \cdot \frac{(\kappa/2)^2}{(\omega_0 - \omega_c)^2 + (\kappa/2)^2},$$
(2.11)

where we have used  $Q = \omega/\kappa$ . Consider that the cavity only affects the DOS within its finite solid angle, one can assume the emission rate into free-space modes unmodified. The total emission rate of the emitter in the cavity  $\gamma'$  can be expressed as

$$\gamma' = \gamma_{\text{cav}} + \gamma^0. \tag{2.12}$$

The ratio of the cavity-modified emission rate to the free-space rate is

$$\frac{\gamma_{\text{cav}}}{\gamma^0} = \frac{3\lambda^3}{4\pi^2} \cdot \frac{Q}{V} \cdot \frac{(\kappa/2)^2}{(\omega_0 - \omega_c)^2 + (\kappa/2)^2}.$$
 (2.13)

When the frequency of the cavity is tuned on resonance with the emitter, Eq. 2.13 simplifies to the form of the Purcell factor given in Eq. 2.2 and Ref. [26]:

$$F = \frac{3\lambda^3}{4\pi^2} \cdot \frac{Q}{V} \,. \tag{2.14}$$

We note that for the simplicity of the derivation, we have only considered an emitter in vacuum. A factor of  $1/n^3$  is thus missing in Eq. 2.14 compared to the more com-

mon form of the Purcell factor [2]. In fact, the treatment of spontaneous emission enhancement for an emitter embedded in a dielectric or plasmonic structure is often complicated, where the expression of V in Eq. 2.10 requires revision. A self-consistent electromagnetic theory which provides the explicit form of V and correctly recovers the expression of F is presented in Ref. [48] (see also the Appendix).

A useful coefficient which describes the efficiency of emission into a particular mode is the  $\beta$ -factor, defined as the ratio of the power emitted into the single mode to the total emitted power [49]. In our case, the  $\beta$ -factor of emission into the cavity mode can be written as

$$\beta = \frac{\gamma_{\text{cav}}}{\gamma'} = \frac{F}{F+1} \,. \tag{2.15}$$

The figure of merit of a cavity for spontaneous emission enhancement is given by Q/V, namely the ratio of its quality factor over its mode volume. It is, thus, desirable to fabricate cavities with a high Q and a small V to achieve a large spontaneous emission enhancement [25].

#### 2.2.2 The Jaynes-Cummings Hamiltonian

Having derived the Purcell factor, we now introduce the Hamiltonian formulation of a coupled emitter-cavity system. At the end of this section, we will comment on the equivalence of the DOS and the Hamiltonian approach in describing the Purcell effect.

The total Hamiltonian of a coupled emitter-cavity system can be written as [28]

$$H = H_{\rm e} + H_{\rm c} + H_{\rm int} \,,$$
 (2.16)

where  $H_e = \hbar \omega_0 (\sigma_+ \sigma_- - \sigma_- \sigma_+)/2$  represents the Hamiltonian of the emitter<sup>2</sup> with  $\sigma_+ = |e\rangle \langle g|$  and  $\sigma_- = |g\rangle \langle e|$  the atomic raising and lowering operators satisfying the anti-commutation relation  $\{\sigma_-, \sigma_+\} = \mathbb{1}$ .  $H_c = \hbar \omega_c a^{\dagger} a$  denotes the Hamiltonian of the cavity mode<sup>3</sup>, in which  $a^{\dagger}$  and a stand for its creation and annihilation operators.  $H_{\rm int}$  is the Hamiltonian describing the interaction between the emitter and the cavity. Considering only the electric dipolar interaction,  $H_{\rm int}$  takes the form

$$H_{\rm int} = -\mu_{eg} \cdot \mathbf{E}_{\rm vac} \,. \tag{2.17}$$

<sup>&</sup>lt;sup>2</sup>We set the zero of the energy in the emitter at the middle of the  $|e\rangle$  and  $|g\rangle$  levels.

<sup>&</sup>lt;sup>3</sup>We set the vacuum energy  $\hbar\omega_c/2$  as the zero of the energy in the cavity mode.

Assuming that the transition dipole of the emitter is aligned with the polarization of the cavity field,  $H_{\text{int}}$  becomes

$$H_{\text{int}} = -\mu_{eg}(\sigma_{-} + \sigma_{+}) \cdot iE_{\text{vac}}(a - a^{\dagger}). \qquad (2.18)$$

Here,  $E_{\text{vac}}$  stands for the amplitude of vacuum electric field in the cavity. After expanding the scalar product, the terms containing  $\sigma_{-}a$  and  $\sigma_{+}a^{\dagger}$  can be negated using the rotating-wave approximation. The interaction Hamiltonian simplifies to

$$H_{\rm int} = -i\hbar g(\sigma_+ a - \sigma_- a^{\dagger}) \tag{2.19}$$

with

$$g = \left(\frac{\mu_{eg}^2 \omega_c}{2\hbar \epsilon_0 V}\right)^{1/2} \tag{2.20}$$

the vacuum Rabi frequency (or the emitter-cavity coupling strength). We restrict our further analysis to the weak-excitation limit, where the system can be assumed to have at most one excitation, corresponding to two possible excited states of  $|e,0\rangle$  and  $|g,1\rangle$ . Here, the first digit in the ket represents the state of the emitter and the second digit denotes the number of photons in the cavity mode. The system Hamiltonian can be expressed in a matrix representation [28]:

$$H = \hbar \begin{bmatrix} \omega_0 & -ig \\ ig & \omega_c \end{bmatrix} - \frac{1}{2}\hbar\omega_0 \mathbb{1}. \tag{2.21}$$

After diagonalizing H, we obtain the two eigenenergies of the excited states

$$E_{\pm} = \hbar \left[ \frac{\omega_c}{2} \pm \sqrt{\left(\frac{\omega_0 - \omega_c}{2}\right)^2 + g^2} \right], \qquad (2.22)$$

and the two corresponding eigenstates

$$|+\rangle = \cos \theta |e, 0\rangle + i \sin \theta |g, 1\rangle ,$$
  
$$|-\rangle = \sin \theta |e, 0\rangle - i \cos \theta |g, 1\rangle ,$$
 (2.23)

with

$$\tan 2\theta = \frac{2g}{\omega_0 - \omega_c} \,. \tag{2.24}$$

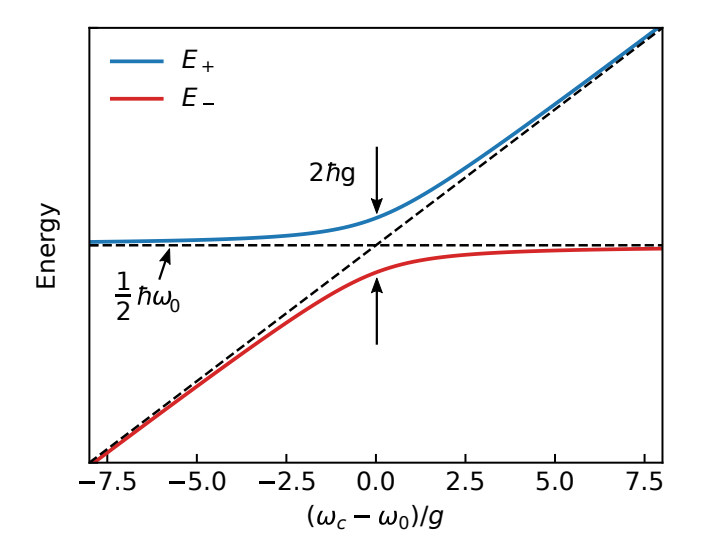


**Figure 2.4:** The two eigenenergies  $E_+$  (blue line) and  $E_-$  (red line) as functions of the emitter-cavity frequency detuning. The dashed lines illustrate the energies of the uncoupled emitter and cavity. The amount of splitting at zero detuning equals  $2\hbar g$ .

One notices that the two excited states of the system  $(|+\rangle, |-\rangle)$  are both entangled states of the emitter and the cavity mode. In Fig. 2.4, we plot the two eigenenergies  $(E_+, E_-)$  as functions of the frequency detuning between the emitter and the cavity. The two eigenenergies show clear avoided crossing and the amount of splitting at zero detuning equals  $2\hbar g$ .

## 2.2.3 Quasi-eigenstate coalescence and strong coupling

So far, we have not considered the dissipation of the system. As a matter of fact, a realistic system always interacts with its environment. For example, the emitter can emit into free-space modes and the cavity field can leak via its mirrors. To account for dissipation, the system can be modeled using a density matrix approach, from which one can define a non-Hermitian Hamiltonian for a more intuitive description. We follow the derivations in Ref. [50] and express the non-Hermitian Hamiltonian as

$$H' = H - i\hbar\gamma^{0}(\sigma_{+}\sigma_{-} - \sigma_{-}\sigma_{+})/2 - i\hbar\kappa a^{\dagger}a/2$$
(2.25)

with H the Hermitian Hamiltonian defined in Eq. 2.16 and  $\kappa$ ,  $\gamma^0$  the cavity linewidth and the spontaneous emission rate of the emitter into free space, respectively. H' can

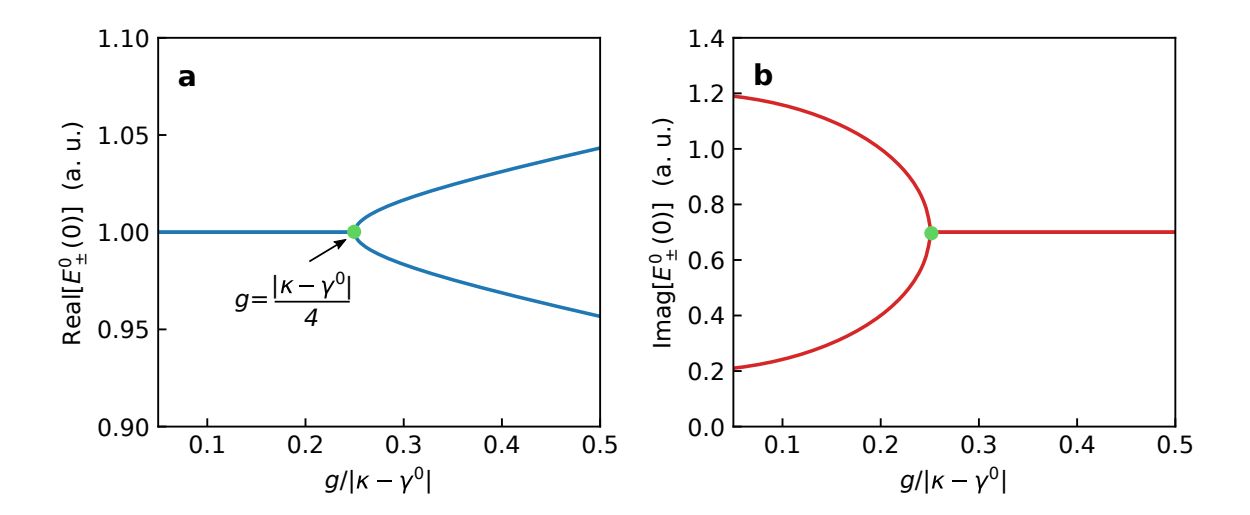


**Figure 2.5:** Real (a) and imaginary (b) parts of  $E'_{\pm}(0)$  as a function of g. The green dots mark the location of the exceptional point.  $(\kappa, \gamma^0)/2\pi = (1.2, 0.2)$  GHz are used for the calculation.

also be expressed in the matrix formulation:

$$H' = \hbar \begin{bmatrix} \omega_0 - i\gamma^0/2 & -ig \\ ig & \omega_c - i\kappa/2 \end{bmatrix} - \frac{1}{2}\hbar\omega_0 \mathbb{1}.$$
 (2.26)

After diagonalizing H', we obtain the quasi-eigenenergies of the system:

$$E'_{\pm}(\omega_0 - \omega_c) = \hbar \left[ \frac{\omega_c - i(\gamma^0 + \kappa)/2}{2} \pm \sqrt{\left(\frac{\omega_0 - \omega_c + i(\kappa - \gamma^0)/2}{2}\right)^2 + g^2} \right]. \quad (2.27)$$

When the cavity and the emitter are coupled resonantly ( $\omega_c = \omega_0$ ), the quasi-eigenenergies simplify to

$$E'_{\pm}(0) = \hbar \left[ \frac{\omega_0}{2} - \frac{i(\gamma^0 + \kappa)}{4} \pm \sqrt{g^2 - \left(\frac{\kappa - \gamma^0}{4}\right)^2} \right]. \tag{2.28}$$

When  $g < |\kappa - \gamma^0|/4$ , the term in the square root is negative and the real part of  $E'_{\pm}(0)$  can only take the value of  $\omega_0$ . In the case of  $g > |\kappa - \gamma^0|/4$ , the real part of  $E'_{\pm}(0)$  can take two different values, representing the energies of two quasi-eigenstates. The point where  $g = |\kappa - \gamma^0|/4$  is thus referred to as the exceptional point (EP). At this point, the two quasi-eigenstates coalesce into a single one [50].

Fig. 2.5 **a** and **b** display the real and imaginary parts of  $E'_{\pm}(0)$  as a function of g (normalized to  $|\kappa - \gamma^0|$ ), respectively. The location of the EP is marked by the green dots. In the limit of  $g \gg |\kappa - \gamma^0|/4$ , the two quasi-eigenenergies approach the values in the non-dissipative case given in Eq. 2.22. The splitting of the eigenenergies is normally a sign of entering the strong-coupling regime of cavity QED. More often, this regime is considered to be reached when a system satisfies  $g \gg (\kappa, \gamma^0)$  [27]. In the strong-coupling regime, the rate of resonant energy exchange between the emitter and the cavity mode is higher than the dissipation rates of the system [28], meaning that the emitter and the cavity can exchange a quantum of excitation for a certain number of rounds within the irreversible dissipation time.

When g is smaller than one of the dissipation rates  $(g < \kappa \text{ or } g < \gamma^0)$ , the system is in the weak-coupling regime. In this regime, the coherent energy exchange between the emitter and the cavity mode is slower than the dissipation of the system. Nevertheless, for an emitter with a linewidth narrower than that of the cavity  $(\gamma^0 < \kappa)$ , its radiative property is still influenced by the cavity, resulting in a modified emission rate (see section 2.2.1).

In the regime where the dissipation rate of the cavity is much larger than the other two rates ( $\kappa \gg 2g$  and  $\kappa \gg \gamma^0$ ), the two quasi-eigenenergies in Eq. 2.28 can be approximated to

$$E'_{+}(0) = \frac{1}{2}\hbar\omega_0 - i\hbar\left(\frac{\gamma^0}{2} + \frac{2g^2}{\kappa}\right),$$
  

$$E'_{-}(0) = \frac{1}{2}\hbar\omega_0 - i\hbar\left(\frac{\kappa}{2} - \frac{2g^2}{\kappa}\right).$$
(2.29)

The first eigenvalue  $E'_{+}(0)$  represents the energy of the emitter, while the second  $(E'_{-}(0))$  represents that of the cavity mode [27]. The imaginary part of  $E'_{+}(0)/\hbar$  corresponds to the half width of the emitter resonance and hence reveals the decay rate of the emitter in the cavity:

$$\gamma' = \gamma^0 + \frac{4g^2}{\kappa} \,. \tag{2.30}$$

The term  $4g^2/\kappa$  stands for the net enhanced emission rate into the cavity mode. The same quantity is denoted by  $\gamma_{\text{cav}} = F \cdot \gamma^0$  in section 2.2.1. Combining Eqs. 2.11, 2.14 and 2.20, one can identify that  $4g^2/\kappa = F \cdot \gamma^0$ . The Hamiltonian and the DOS treatments are thus consistent in describing the Purcell effect in the weak-coupling regime.

Next, we introduce another important parameter in cavity QED, namely the cooperativity C, defined as

$$C = \frac{\gamma_{\text{cav}}}{\gamma^0} = \frac{4g^2}{\kappa \gamma^0} \,. \tag{2.31}$$

We note that for an ideal two-level emitter, F and C are identical. However, F is more commonly used for weakly coupled systems, whereas C appears often in the discussions of the strong-coupling regime.

# 2.3 Coherent interaction of a molecule with a cavity mode

Having introduced the general theoretical background of cavity QED, we now focus on the experimental scenario of a single molecule coupled to a microcavity. Following the model presented in Ref. [51], we derive the complex transmission and reflection coefficients of the coupled system. We first consider the weak-excitation regime, in which we analyze the modifications to the molecular linewidth and center frequency and the phase shift on an incident laser beam. We then study the nonlinear response of the system at higher pump powers. Lastly, we study the photon statistics of the light transmitted through the system.

## 2.3.1 Transmission and reflection spectra

We consider a molecule with a free-space spontaneous emission rate  $\gamma^0$ , which equals the sum of the emission rates via the 00ZPL ( $\gamma_{\rm zpl}$ ) and via all the red-shifted transitions ( $\gamma_{\rm red}$ ). The non-radiative decay and pure dephasing are not considered, since both rates are negligible for PAH molecules at liquid helium temperatures [22,52]. As depicted in Fig. 2.6, the molecule is placed in a microcavity consisting of two mirrors with its resonance frequency  $\omega_c$  tuned to match the 00ZPL frequency of the molecule  $\omega_0$ . The coupling enhances the 00ZPL transition by  $\gamma_{\rm cav} = F \cdot \gamma_{\rm zpl}$ , where F is the Purcell factor. Since the cavity mirrors only cover a finite solid angle (up to  $1.3\pi$  in our experiments), we assume that the spontaneous emission rate of the molecule to all other modes (freespace) is unmodified by the cavity, i.e. still equals  $\gamma^0$ . The total decay rate of the molecule in the cavity can thus be written as  $\gamma' = \gamma_{\rm cav} + \gamma^0$ .

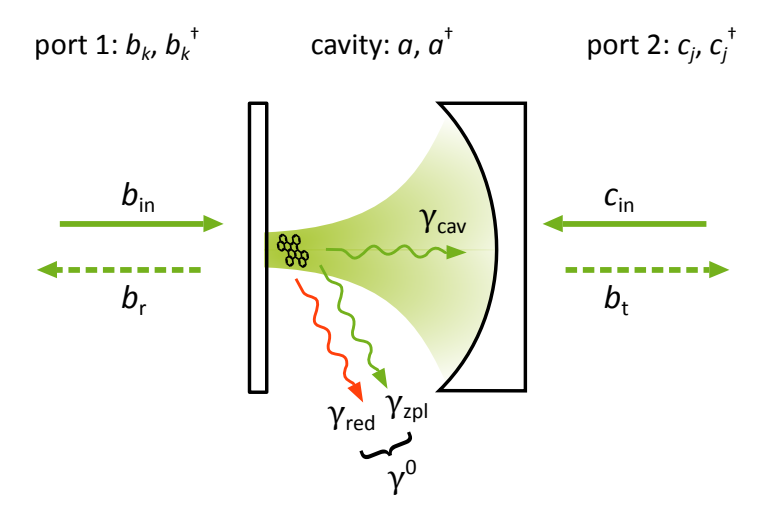


Figure 2.6: Illustration of the system under study. A molecule is coupled to a single mode of a microcavity. The spontaneous emission rate of the molecule in free space is denoted by  $\gamma^0$ , which is equal to the sum of  $\gamma_{\rm zpl}$  (emission rate via the 00ZPL) and  $\gamma_{\rm red}$  (emission rates via all the red-shifted transitions).  $\gamma_{\rm cav}$  stands for the net enhanced emission rate by the cavity. The cavity mode is represented by the annihilation operator a and couples to the free space modes in port 1 and port 2 via its two mirrors. The fields in port 1 and port 2 are represented by the annihilation operators  $b_k$  and  $c_j$ , respectively.  $b_{\rm in}$  and  $c_{\rm in}$  denote the input fields from port 1 and 2,  $b_r$  and  $b_t$  represent the reflected and transmitted fields of the incident field  $b_{\rm in}$ . See text for details.

As discussed in section 2.1, the molecule can be approximated as a two-level system (TLS) given the fast relaxations of the  $|S_0, v \neq 0\rangle$  levels. The decays from  $|S_1, v = 0\rangle$  into these levels are accounted for by including an additional dissipation rate  $\gamma_{\text{red}}$  to the upper level. In the analysis of this section, we use  $|g\rangle$  and  $|e\rangle$  to denote  $|S_0, v = 0\rangle$  and  $|S_1, v = 0\rangle$  states, respectively. The corresponding atomic raising and lowering operators are written as  $\sigma_+ = |e\rangle \langle g|$  and  $\sigma_- = |g\rangle \langle e|$ .

We consider a perfect symmetric cavity, where the two mirrors are non-absorptive and have equal transmission and reflection coefficients. We use  $a^{\dagger}$  and a to represent the photon creation and annihilation operators of the cavity mode. The cavity mode is coupled to the electromagnetic modes in free space (port 1, port 2) via its two mirrors (see Fig. 2.6). The photon annihilation (creation) operators of port 1 and 2 are denoted as  $b_k$  ( $b_k^{\dagger}$ ) and  $c_j$  ( $c_j^{\dagger}$ ), respectively.

The Hamiltonian of the system can be written as

$$H = \hbar\omega_0(\sigma_+\sigma_- - \sigma_-\sigma_+)/2 + \hbar\omega_c a^{\dagger}a - i\hbar g(\sigma_+a - \sigma_-a^{\dagger}) + \sum_k \hbar\omega_k b_k^{\dagger}b_k + \sum_j \hbar\omega_j c_j^{\dagger}c_j$$
$$-i\hbar \sum_k (g_1b_k^{\dagger}a - g_1a^{\dagger}b_k) - i\hbar \sum_j (g_2c_j^{\dagger}a - g_2a^{\dagger}c_j), \qquad (2.32)$$

where  $\omega_k$  ( $\omega_j$ ) denotes the frequency of the field in port 1 (2), g represents the moleculecavity coupling strength defined in Eq. 2.20 and  $g_1$  and  $g_2$  are real constants standing for the coupling strengths of the cavity mode to the modes in port 1 and 2, respectively.

In the next step, we write down the Heisenberg equation of motion (EOM) for the operators using

$$\frac{d\langle O(t)\rangle}{dt} = \frac{i}{\hbar} \left[ H, O(t) \right] + \left( \frac{\partial O(t)}{\partial t} \right)_{H}$$
 (2.33)

with O(t) a time-dependent operator, to arrive at

$$\dot{\sigma}_{-} = -i\omega_{0}\sigma_{-} + g\sigma_{z}a,$$

$$\dot{\sigma}_{z} = -2g(\sigma_{+}a + a^{\dagger}\sigma_{-}),$$

$$\dot{b}_{k} = -i\omega_{k}b_{k} - g_{1}a,$$

$$\dot{c}_{j} = -i\omega_{l}c_{j} - g_{2}a,$$

$$\dot{a} = -i\omega_{c}a + g\sigma_{-} + g_{1}\sum_{k}b_{k} + g_{2}\sum_{l}c_{j},$$
(2.34)

where  $\sigma_z = \sigma_+ \sigma_- - \sigma_- \sigma_+$ .

We use the operators  $b_{\rm in}$  and  $c_{\rm in}$  to represent the input fields from port 1 and port 2, respectively. The transmitted field  $b_t$  and the reflected field  $b_r$  (with respect to  $b_{\rm in}$ , the incident field from port 1) are defined following the derivations in Ref. [51], as

$$b_r = b_{\rm in} - \sqrt{\frac{\kappa}{2}} a,$$

$$b_t = c_{\rm in} - \sqrt{\frac{\kappa}{2}} a,$$
(2.35)

where  $\kappa$  denotes the decay rate of the cavity field, corresponding to the FWHM of the cavity's transmission spectrum. We note that despite the damping, the fluctuations of  $b_r$  and  $b_t$  maintain the commutator relations of a. The quantities  $b_{\rm in}^{\dagger}b_{\rm in}$ ,  $c_{\rm in}^{\dagger}c_{\rm in}$ ,  $b_r^{\dagger}b_r$  and  $b_t^{\dagger}b_t$  carry the unit of number of photons per unit of time, representing the power in their respective channel.

Combining Eqs. 2.34, 2.35, the temporal evolution of a becomes

$$\dot{a} = -i\omega_c a - \frac{\kappa}{2}a + g\sigma_- + \sqrt{\frac{\kappa}{2}}(b_{\rm in} + c_{\rm in}). \tag{2.36}$$

We express the EOMs in the rotating frame at the laser frequency  $\omega_l$ , to arrive at

$$\dot{\sigma}_{-} = i\Delta\omega\sigma_{-} + g\sigma_{z}a,$$

$$\dot{\sigma}_{z} = -2g(\sigma_{+}a + a^{\dagger}\sigma_{-}),$$

$$\dot{a} = i(\Delta\omega - \delta)a - \frac{\kappa}{2}a + g\sigma_{-} + \sqrt{\frac{\kappa}{2}}(b_{\rm in} + c_{\rm in}),$$
(2.37)

with  $\Delta \omega = \omega_l - \omega_0$  and  $\delta = \omega_c - {\omega_0}^4$ .

So far, we have not considered the coupling of the molecule with the free-space modes. This coupling is a dissipation from the system and can be taken into account by adding the spontaneous emission rate  $\gamma^0$  into the EOMs [51], which become

$$\dot{\sigma}_{-} = i\Delta\omega\sigma_{-} + g\sigma_{z}a - \frac{\gamma^{0}}{2}\sigma_{-} + G,$$

$$\dot{\sigma}_{z} = -2g(\sigma_{+}a + a^{\dagger}\sigma_{-}) - \gamma^{0}(\sigma_{z} + 1) + K,$$

$$\dot{a} = i(\Delta\omega - \delta)a - \frac{\kappa}{2}a + g\sigma_{-} + \sqrt{\frac{\kappa}{2}}(b_{\rm in} + c_{\rm in}) + H,$$
(2.38)

where K, G and H are noise operators due to the interaction of the molecule with the free-space modes. In the experiment, these modes are not excited by external fields, i.e. they are in the vacuum state, therefore  $\langle G \rangle = \langle H \rangle = \langle K \rangle = 0$ .

We now focus on the weak excitation limit, where the population of the excited state is negligible, i.e.  $\langle \sigma_z \rangle \approx -1$ . The cavity field can be eliminated adiabatically from the EOMs when considering a steady-state response. We set  $\dot{a}=0$  and obtain

$$a = \frac{g\sigma_{-} + \sqrt{\kappa}(b_{\rm in} + c_{\rm in})}{-i(\Delta\omega - \delta) + \kappa/2}.$$
 (2.39)

After inserting Eq. 2.39 into the EOMs and considering a vacuum state for port 2  $(c_{\text{in}} = 0)$ , we arrive at

$$\dot{s} = i\Delta\omega s - \frac{\gamma_{\text{cav}}}{2} \left( t_0 + \frac{\gamma^0}{\gamma_{\text{cav}}} \right) s + \sqrt{\frac{\gamma_{\text{cav}}}{2}} b_{\text{in}} t_0,$$

$$b_t = -t_0 b_{\text{in}} + \sqrt{\frac{\gamma_{\text{cav}}}{2}} t_0 s,$$

$$b_r = b_{\text{in}} + b_t ,$$
(2.40)

<sup>&</sup>lt;sup>4</sup>We note the differences in the conventions of  $\kappa$  and  $\Delta\omega$  in Ref. [51] and this thesis.  $\kappa$  and  $\Delta\omega$  quoted in this thesis correspond to  $2\kappa$  and  $-\Delta\omega$  in Ref. [51].

where  $s = \langle \sigma_{-} \rangle$  and

$$t_0(\Delta\omega) = \frac{-1}{1 - i\frac{\Delta\omega - \delta}{\kappa/2}}$$
 (2.41)

denotes the transmission coefficient of an empty cavity. The transmission coefficient of the coupled molecule-cavity system can be obtained by taking the ratio of the transmitted field  $b_t$  to the incident field  $b_{\rm in}$ :

$$t(\Delta\omega) = \frac{b_t}{b_{\rm in}} = t_0 \cdot \left[ 1 - \frac{1}{1 + \left( i \frac{2\Delta\omega}{\gamma_{\rm cav}} - \frac{\gamma^0}{\gamma_{\rm cav}} \right) \left( i \frac{\Delta\omega - \delta}{\kappa/2} - 1 \right)} \right]. \tag{2.42}$$

Similarly, the complex reflection coefficient r can be calculated with

$$r = \frac{b_r}{b_{\rm in}} = 1 + t \ . \tag{2.43}$$

In the experiment, one normally measures the transmission and reflection coefficients in energy (T, R), which are related to the complex coefficients t, r by

$$T = |t|^2$$
,  
 $R = |r|^2$ . (2.44)

The blue curves in Fig. 2.7 **a**, **b**, **c** represent exemplary transmission spectra of a coupled system with  $(\kappa, \gamma^0, \gamma_{\text{cav}})/2\pi = (10, 0.04, 0.4)$  GHz and for three different molecule-cavity detunings as given in the legends. The transmission spectra without coupling to the molecule (empty cavity) are plotted as the dashed black lines. The resonant coupling to the molecule introduces a dip in the transmission spectrum (see **a**), which is a result of destructive interference of the molecular scattering with the cavity field [51]. When the cavity is detuned from the molecular resonance (see **b**, **c**), the interference shows up as a Fano-shaped signal [53], since the phase of the molecular scattering flips sign from the red to the blue side of its resonance. The red curves in Fig. 2.7 **d**, **e**, **f** present the reflection spectra of the system with the same parameters as in **a**, **b**, **c**. When the cavity is tuned on resonance (as shown in **d**), the molecule introduces a peak in the reflection signal, which confirms that the interaction is a coherent interference effect rather than purely absorptive.

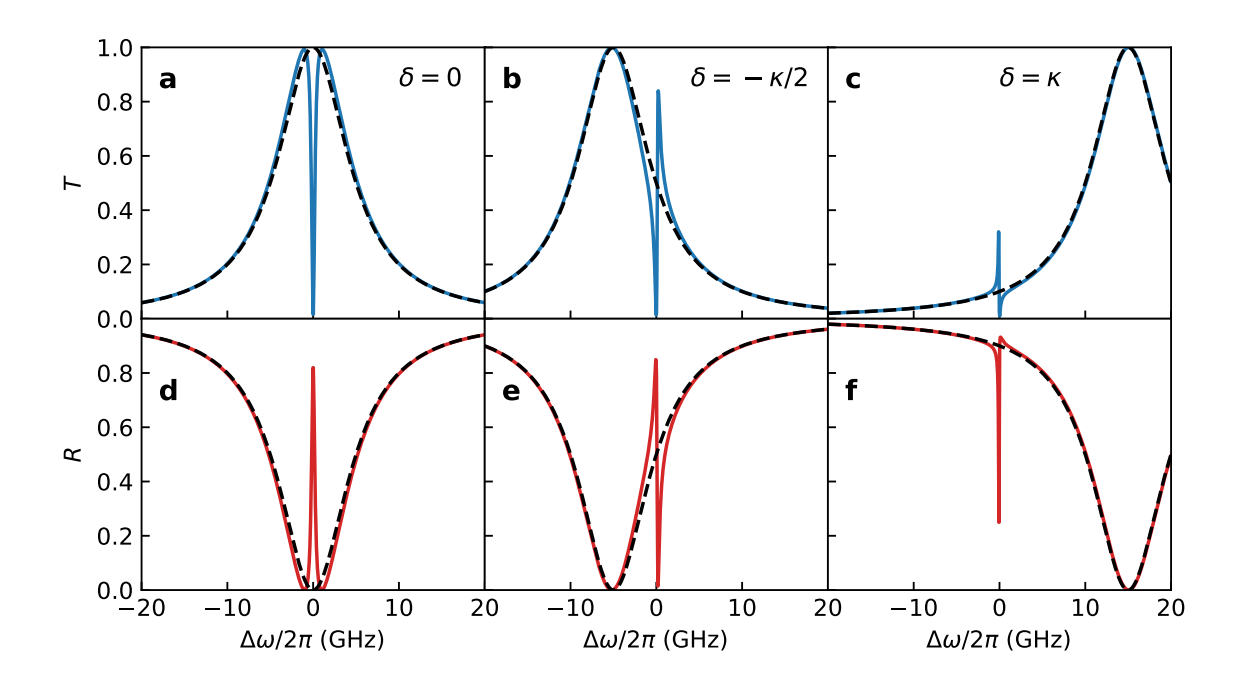


**Figure 2.7: a, b, c**, Blue curves display the transmission spectra of the coupled moleculecavity system with  $\delta = (0, -\kappa/2, \kappa)$ , correspondingly. The reflection spectra are shown by the red lines in **d, e, f**. Dashed black lines represent the transmission spectra of the empty cavity.  $(\kappa, \gamma^0, \gamma_{\text{cav}})/2\pi = (10, 0.04, 0.4)$  GHz are used for the calculations.

Using Eqs. 2.42-2.44, we can calculate the amplitude of the resonant ( $\delta = 0, \Delta \omega = 0$ ) transmission and reflection of the coupled system:

$$T(\delta = 0, \Delta\omega = 0) = \left(1 - \frac{\gamma_{\text{cav}}}{\gamma_{\text{cav}} + \gamma^0}\right)^2 = (1 - \beta)^2,$$

$$R(\delta = 0, \Delta\omega = 0) = \left(\frac{\gamma_{\text{cav}}}{\gamma_{\text{cav}} + \gamma^0}\right)^2 = \beta^2,$$
(2.45)

where  $\beta = \gamma_{\rm cav}/(\gamma_{\rm cav} + \gamma^0)$ , as defined in section 2.2.1. One would expect a stronger coherent interaction when the molecule scatters more efficiently into the cavity mode. This is evidenced by Eq. 2.45, that for a larger  $\gamma_{\rm cav}$  (a larger  $\beta$ ), the modifications in T and R are stronger. In the limit of  $\beta = 1$ , the molecule acts as a perfect mirror: it blocks the transmission completely (T = 0) and reflects all the incident light back to the input port (R = 1). In Fig. 2.8, we plot the transmission (a) and reflection (b) spectra in the close frequency range of the molecule for  $(\kappa, \gamma^0, \delta)/2\pi = (10, 0.04, 0)$  GHz and different values of  $\gamma_{\rm cav}$  as displayed in the legend. As expected, with increasing  $\gamma_{\rm cav}$ , the amplitude of the signal becomes higher and the linewidth becomes broader. The FWHM of the profile equals  $\gamma_{\rm cav} + \gamma^0$ , which we will derive in the coming section.

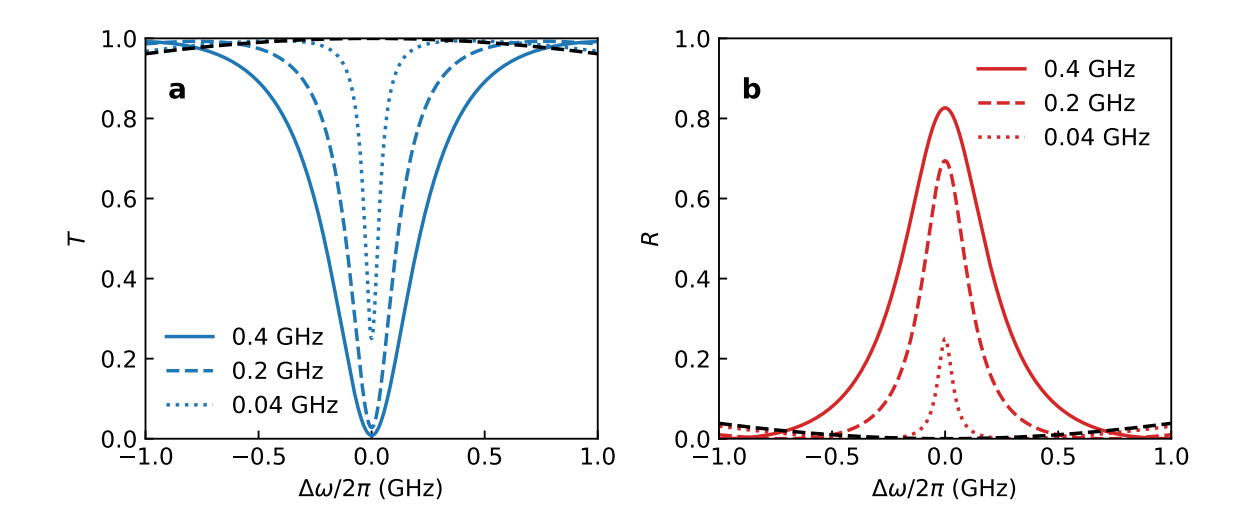


**Figure 2.8: a, b,** Transmission and reflection spectra in the close frequency range of the molecule, with  $(\kappa, \gamma^0, \delta)/2\pi = (10, 0.04, 0)$  GHz and the values of  $\gamma_{\text{cav}}/2\pi$  displayed in the legends. The dashed black lines represent the spectra of an empty cavity.

Note that we have considered an ideal symmetric cavity with perfect mode match to the incident field. In experiment, the coupling efficiency to the cavity mode is normally limited by the mode and impedance mismatches. To correctly describe the experimental spectra, one needs to consider an in/out-coupling efficiency in the expressions of t and r. We will introduce the explicit expression as it arises in the experimental chapters.

#### 2.3.2 Purcell effect and Lamb shift

It is well known that the modification of the photonic density of states by the cavity affects the linewidth and the center frequency of an atom inside [28,54]. The former effect is known as the Purcell effect [26], discussed at the beginning of this chapter. The latter effect can be considered a modification of the Lamb shift [47,55], which results from the coupling of the electronic transition to vacuum fields. In this section, we show that the amplitudes of both effects depend on the molecule-cavity detuning and can be extracted from the transmission spectrum.

We denote the linewidth of the molecular resonance and the change in its center frequency  $\gamma$  and  $\delta\omega_0$ , respectively. We start from Eq. 2.42 and Eq. 2.44 and consider a regime in which the cavity resonance is much broader than the modified molecular resonance ( $\kappa \gg \gamma^0$ ,  $\kappa \gg \gamma_{\rm cav}$ ). When studying the spectrum in the vicinity of the molecular frequency ( $|\Delta\omega| \lesssim \gamma_{\rm cav}/2$ ), we can make the approximation  $\Delta\omega/\kappa \approx 0$  and

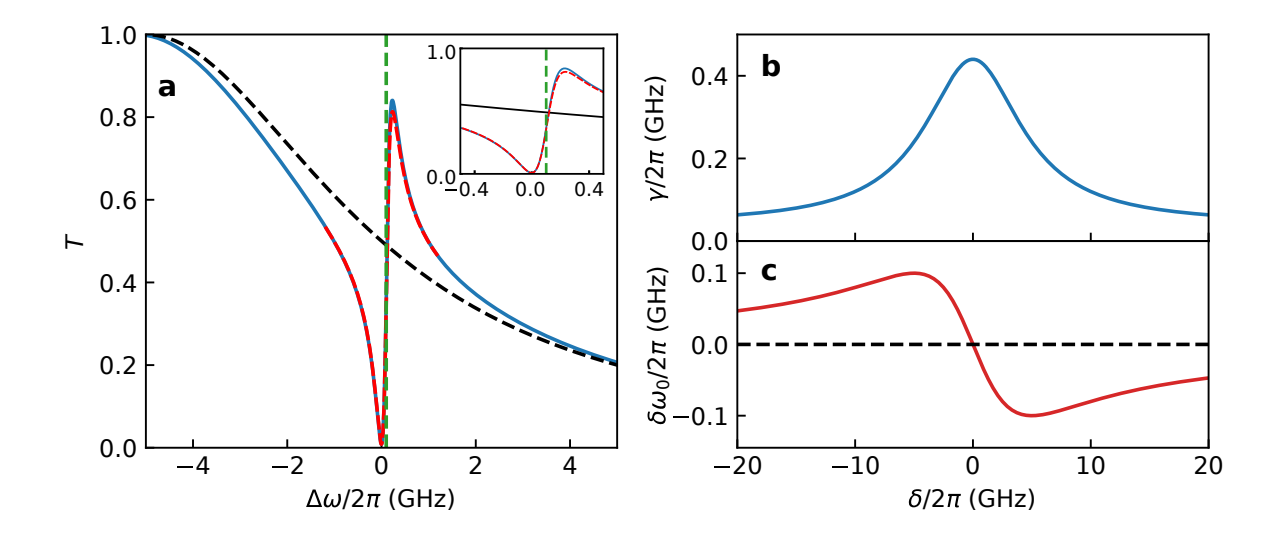


Figure 2.9: a, Blue line displays the transmission spectrum of the coupled system calculated using  $(\kappa, \gamma^0, \gamma_{\text{cav}}, \delta)/2\pi = (10, 0.04, 0.4, -5)$  GHz. The dashed black line shows the spectrum of an empty cavity. The red line represents the calculated spectrum in the vicinity of the molecule using Eq. 2.46. The vertical green line marks the center frequency of the generalized Lorentzian function. The inset shows a close-up of the spectra in the frequency interval (-0.5, 0.5) GHz. The small deviation of the green line from zero indicates the modification of the Lamb shift. b, c, Linewidth and change in center frequency of the molecule as a function of the molecule-cavity detuning, respectively. The dashed black line in c marks the frequency of the molecule in free space.

simplify the expression of T to:

$$T = T_{\text{cav}} \cdot \left[ 1 + \frac{-\frac{2\delta\kappa\gamma_{\text{cav}}}{4\delta^2 + \kappa^2} \left(\Delta\omega + \frac{\delta\kappa\gamma_{\text{cav}}}{4\delta^2 + \kappa^2}\right) + \frac{\gamma_{\text{cav}}^2\kappa^2}{4\left(4\delta^2 + \kappa^2\right)} \left(\frac{8\delta^2}{4\delta^2 + \kappa^2} - \frac{2\gamma^0}{\gamma_{\text{cav}}} - 1\right)}{\left(\Delta\omega + \frac{\delta\kappa\gamma_{\text{cav}}}{4\delta^2 + \kappa^2}\right)^2 + \frac{1}{4}\left(\frac{\kappa^2}{4\delta^2 + \kappa^2} \cdot \gamma_{\text{cav}} + \gamma^0\right)^2}\right],$$
(2.46)

where  $T_{\text{cav}} = |t_0|^2$  represents the transmission spectrum of an empty cavity.  $T/T_{\text{cav}}$  is a generalized Lorentzian function, i.e. the sum of a dissipative and a dispersive Lorentzian profile with the same center frequencies and linewidths. The linewidth and center frequency of the molecule (indicated by the generalized Lorentzian profile) are given by

$$\gamma(\delta) = \left(\frac{\kappa^2}{4\delta^2 + \kappa^2} \cdot F + 1\right) \cdot \gamma^0,$$

$$\delta\omega_0(\delta) = -\frac{\delta\kappa F}{4\delta^2 + \kappa^2} \cdot \gamma^0,$$
(2.47)

which are different from the values of the molecule in free space. The solid blue curve in Fig. 2.9 a displays the transmission spectrum of a system with  $(\kappa, \gamma^0, \gamma_{\text{cav}}, \delta)/2\pi = (10, 0.04, 0.4, -5)$  GHz according to Eqs. 2.42 and 2.44. The dashed red line shows the spectrum calculated using Eq. 2.46. The close agreement between the two curves confirms the validity of the approximation. The dashed green line marks the center frequency of the generalized Lorentzian profile. Its slight deviation from zero indicates the cavity-modified Lamb shift. The dashed black line represents the spectrum of an empty cavity as a reference.

The molecular linewidth  $\gamma$  is a Lorentzian function of  $\delta$ . When the cavity is placed on resonance with the molecule,  $\gamma = \gamma_{\text{cav}} + \gamma^0$ , showing the Purcell-enhanced linewidth of the molecule. When the cavity is far detuned  $(\delta \gg \kappa)$ ,  $\gamma \approx \gamma_{\text{leak}}$ , revealing the molecular linewidth in free space. The shift in the center frequency  $\delta\omega_0$  follows a dispersive lineshape with respect to  $\delta$  and vanishes at zero detuning. When the cavity is far detuned  $(\delta \gg \kappa)$ ,

$$\delta\omega_0\left(\delta\right) \approx -\frac{\kappa\gamma_{\text{cav}}}{4\delta} = -\frac{g^2}{\delta}\,,$$
 (2.48)

recovering the known formula for the cavity-modified Lamb shift in this regime [28]. The dependences of  $\gamma$  and  $\delta\omega_0$  on  $\delta$  are plotted in Fig. 2.9 b, c.

### 2.3.3 Phase response

The scattering of light by an atom is also accompanied by a phase shift. The information on the phase can be utilized to realize nondestructive detection of photons [56]. In this section, we examine the phase shift a laser beam acquired after traversing the coupled molecule-cavity system.

The complex transmission coefficient t of the coupled system can be expressed as

$$t = t_0 \cdot t' = |t_0| \cdot e^{i\phi_0} \cdot |t'| \cdot e^{i\phi'} = |t_0| \cdot |t'| \cdot e^{i(\phi_0 + \phi')}, \qquad (2.49)$$

where t' represents the term in the squared brackets of Eq. 2.42 and we have separated the amplitudes from the phases.  $\phi_0$  denotes the argument of  $t_0$  and represents the phase shift of transmission through an empty cavity.  $\phi'$  stands for the additional phase shift due to the coupling to the molecule. The dashed black line in Fig. 2.10 a displays the phase shift of transmission through an empty cavity with  $\kappa/2\pi = 5 \,\text{GHz}$ . The phase of the resonantly transmitted light is shifted by  $\pi$  from the incoming beam, which is marked by the dashed-dotted black line and originates from the minus sign

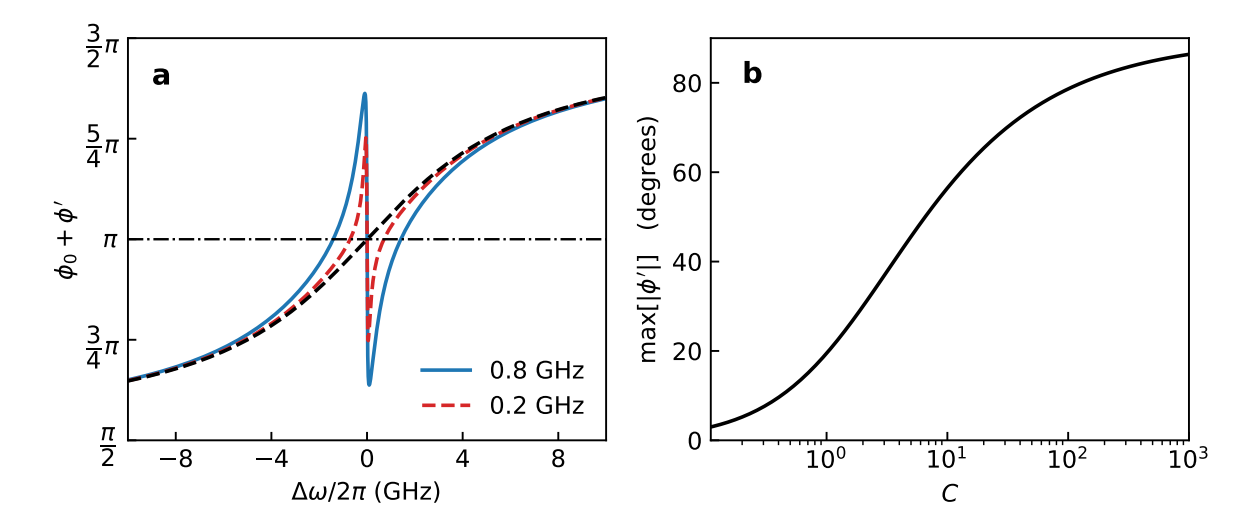


**Figure 2.10:** a, Phase shift on transmission through the coupled molecule-cavity system with  $(\kappa, \gamma^0, \delta)/2\pi = (10, 0.04, 0)$  GHz and  $\gamma_{\rm cav}/2\pi = 0.8$  GHz (blue), 0.2 GHz (red). The dashed black line represents the phase shift of an empty cavity. The phase shift of resonant transmission through an empty cavity amounts to  $\pi$  and is marked by the dashed-dotted black line. b, Calculated maximal phase shift as a function of cooperativity.

in the expression of  $t_0$  (see Eq. 2.41). The phase shift covers the range of  $(\pi/2, 3\pi/2)$ . The solid blue curve shows the phase shift  $\phi_0 + \phi'$  when a molecule is coupled to the cavity with  $(\gamma^0, \gamma_{\text{cav}})/2\pi = (0.04, 0.8)$  GHz. The molecule introduces a sharp change in phase with amplitudes of up to  $\pm \pi/3$ . The dashed red line displays the phase shift for a weaker molecule-cavity coupling with  $\gamma_{\text{cav}}/2\pi = 0.2$  GHz. In this case, the phase is shifted by up to  $\pm \pi/4$ .

A simple analytical expression of the phase shift by the molecule  $\phi'$  can be obtained in the limit  $\kappa \gg \gamma$ , where the approximation  $\Delta \omega / \kappa \approx 0$  can be applied to obtain

$$\tan\left[\phi'(\Delta\omega)\right] \approx -\frac{1}{\Delta\omega \cdot \frac{2}{\gamma_{\text{cav}}} + \frac{1}{\Delta\omega} \cdot \frac{\gamma^0}{2} \cdot \left(1 + \frac{\gamma^0}{\gamma_{\text{cav}}}\right)}.$$
 (2.50)

The maximal phase shift of

$$\max\left[|\phi'(\Delta\omega)|\right] = \arctan\left[\frac{1}{2\sqrt{\frac{\gamma^0}{\gamma_{\text{cav}}} \cdot \left(1 + \frac{\gamma^0}{\gamma_{\text{cav}}}\right)}}\right] = \arctan\left(\frac{1}{2}\sqrt{\frac{C^2}{C+1}}\right) \qquad (2.51)$$

can be achieved when  $\Delta \omega = \pm \sqrt{\gamma^0 (\gamma_{\text{cav}} + \gamma^0)/4}$ , with  $C = \gamma_{\text{cav}}/\gamma^0$  the cooperativity of the system. The maximal phase shift scales nonlinearly with C, as displayed in

Fig. 2.10 **b**. One finds that to reach a phase shift close to  $90^{\circ}$ , it is necessary to have C in the order of 1000.

#### 2.3.4 Saturation of the system

So far, we have focused on the weak-excitation regime and studied the spectral and phase properties of the system. The efficient interaction of the molecule with the cavity also gives rise to strong optical nonlinearities at higher incident powers. We consider only a resonantly coupled system ( $\delta = 0$ ,  $\Delta \omega = 0$ ) and follow the derivations in Ref. [51]. The steady-state solutions for the atomic operators at an arbitrary incident power can be written as

$$s_z = \langle \sigma_z \rangle = -\frac{1}{1+S},$$
  
 $s = \langle \sigma_- \rangle = \sqrt{\frac{2}{\gamma_{\text{cav}}}} \frac{b_{\text{in}}}{1+S} \beta,$  (2.52)

where  $S = 4\beta^2 |b_{\rm in}|^2/\gamma_{\rm cav}$  denotes the saturation parameter. S can alternatively be expressed as

$$S = \frac{|b_{\rm in}|^2/\gamma'}{\gamma_{\rm cav}/(4\beta^2\gamma')} = \frac{n_{\rm in}}{n_{\rm c}},\tag{2.53}$$

where  $n_{\rm in} = |b_{\rm in}|^2/\gamma'$  represents the number of incident photons per Purcell-enhanced lifetime of the molecule and  $n_{\rm c} = \gamma_{\rm cav}/(4\beta^2\gamma')$  denotes the critical photon number to reach S = 1.

Using the expression of the transmitted field  $b_t$  (see Eq. 2.40), the transmitted power can be written as

$$\langle b_t^{\dagger} b_t \rangle = |b_{\rm in}|^2 - 2|b_{\rm in}| \sqrt{\frac{\gamma_{\rm cav}}{2}} \cdot \text{Re}\left[\langle s \rangle\right] + \frac{\gamma_{\rm cav}}{2} \langle s^{\dagger} s \rangle .$$
 (2.54)

Combining Eq. 2.52 and Eq. 2.54, gives

$$\langle b_t^{\dagger} b_t \rangle = |b_{\rm in}|^2 \cdot \left[ \left( 1 - \frac{\beta}{1+S} \right)^2 + \beta^2 \cdot \frac{S}{(1+S)^2} \right] , \qquad (2.55)$$

where the first term in the square brackets represents the coherent contribution to the transmitted power ( $|\langle b_t \rangle|^2$ ) and the second term stems from the fluctuations of it

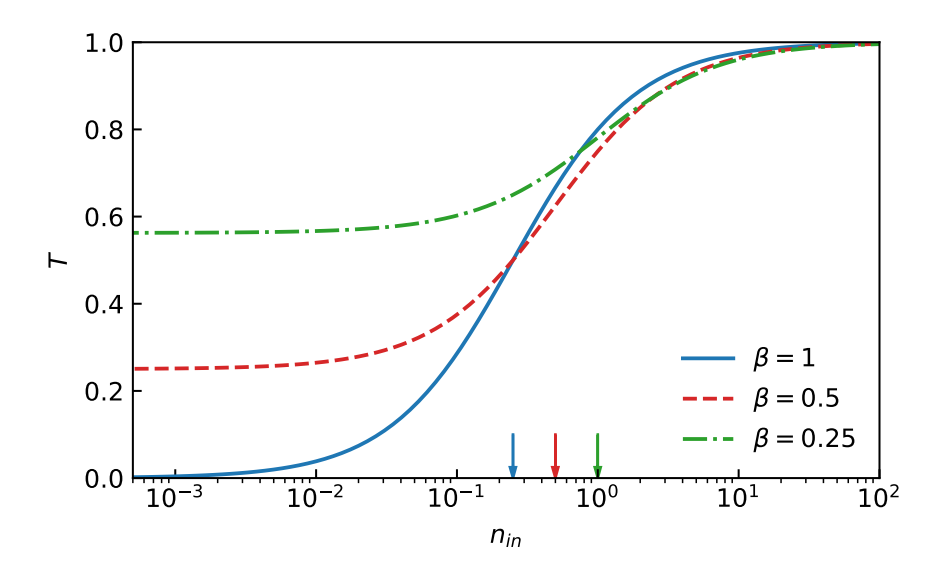


Figure 2.11: Resonant transmission of the coupled-system versus the incident photon number per lifetime of the molecule, calculated using Eq. 2.56 for  $\beta = 1$  (solid blue), 0.5 (dashed red) and 0.25 (dash-dotted green). The critical photon numbers for the three cases are marked by the correspondingly colored arrows.

 $(\langle b_t^\dagger b_t \rangle - |\langle b_t \rangle|^2)$ . The steady-state transmission of the cavity is then

$$T = \frac{\langle b_t^{\dagger} b_t \rangle}{|b_{\rm in}|^2} = \left(1 - \frac{\beta}{1+S}\right)^2 + \beta^2 \cdot \frac{S}{(1+S)^2}.$$
 (2.56)

Figure 2.11 displays the resonant transmission through the system as a function of  $n_{\rm in}$  for systems with different values of  $\beta$ . The resonant transmission at low excitation powers is given by Eq. 2.45. The transmission saturates gradually as the incident power increases. The critical photon numbers to reach S=1 are marked by the colored arrows.

In the regime of very high pump rates  $(S \to \infty)$ ,  $s_z \approx 0$ , meaning that the occupation probability of the excited state is 50%. We note that a single photon is predicted to be enough to act as a  $\pi$ -pulse and completely invert a two-level system [57]. This is a transient process and requires the spatial and temporal modes of the photon to match the time-reverse of a spontaneously emitted photon. The complete inversion of a two-level system is not possible in the steady-state. Considering a perfect coupling  $(\beta = 1)$  in our model, the minimal critical photon number to reach S = 1 is 0.25 [51].

## 2.4 Photon statistics of the transmitted light

The coupling to an emitter not only modifies the cavity's transmission and reflection spectra, but also gives rise to dynamic effects which can be observed in the photon statistics of the intracavity and transmitted fields [58–60]. In contrast to the structural effects such as the spectral modifications, which can be described by a classical model [61], the dynamic effects can result in nonclassical photon correlations which can only be explained quantum mechanically [60].

#### 2.4.1 Theoretical model

We start by briefly reviewing the theoretical model developed in Ref. [60] for describing the photon statistics of the intracavity field of a coupled emitter-cavity system. The model considers a two-level emitter resonantly coupled to a cavity mode and driven by a weak resonant laser field. In this regime, one can assume the system to have at most two excitations and neglect the higher excitation states. A master equation approach was employed to describe the temporal evolution, which can be solved for a truncated expansion of the joint density matrix. The steady-state wavefunction of the system expanded up to two excitation quanta can be expressed as

$$|\psi\rangle = |g,0\rangle + A|g,1\rangle + B|e,0\rangle + (A^2/2)pq|g,2\rangle + ABq|e,1\rangle, \qquad (2.57)$$

where,

$$A = (2E/\kappa)/(1+C),$$

$$B = -(2g/\gamma^{0}) \cdot A,$$

$$p = 1 - C/(1+\gamma^{0}/\kappa),$$

$$q = (1+C)/[1+C-C/(1+\gamma^{0}/\kappa)],$$
(2.58)

and E is the amplitude of the intracavity driving field. The first digit in the ket denotes the state of the atom while the second digit represents the number of photons in the cavity mode  $^{5}$ . The normalized second-order intensity-correlation function of the

<sup>&</sup>lt;sup>5</sup>We note the differences in the conventions of C and  $\kappa$  in Ref. [60] and this thesis: C and  $\kappa$  quoted in this thesis correspond to 2C and  $2\kappa$  in Ref. [60], respectively.

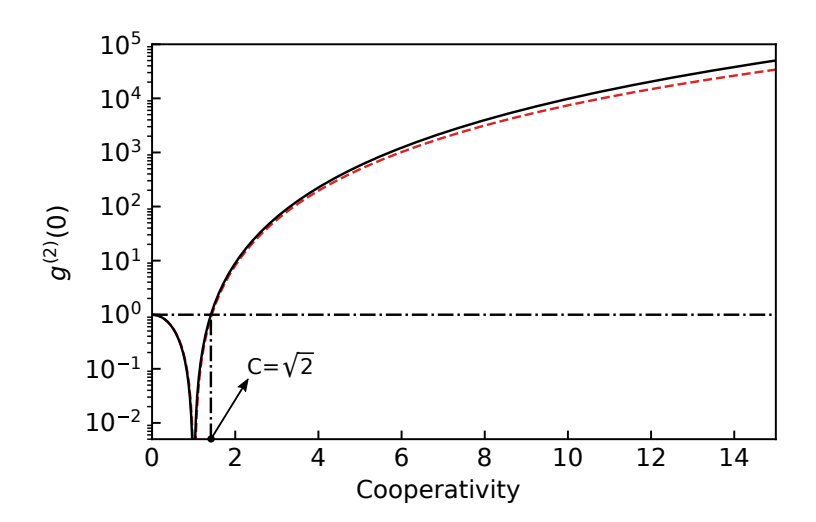


**Figure 2.12:** Dependence of  $g^{(2)}(0)$  of the intracavity field on the cooperativity C. The dashed red line displays  $g^{(2)}(0)$  calculated using Eq. 2.60, for a system with  $(\gamma^0, \kappa)/2\pi = (0.04, 3)$  GHz. The solid black line shows the calculation using Eq. 2.62, assuming  $\gamma^0/\kappa \ll 1$ . The dashed-dotted lines mark the position of  $C = \sqrt{2}$  and  $g^{(2)}(0) = 1$ .

intracavity field can be calculated with

$$g^{(2)}(\tau) = \frac{\langle \psi | a^{\dagger}(0) a^{\dagger}(\tau) a(\tau) a(0) | \psi \rangle}{(\langle \psi | a^{\dagger}(0) a(0) | \psi \rangle)^2} . \tag{2.59}$$

Using the expression of the steady-state wavefunction  $|\psi\rangle$  in Eq. 2.57, one arrives at

$$g^{(2)}(\tau) = |1 + (pq - 1) \exp\left(-\frac{\kappa + \gamma^0}{4}\tau\right) (\cosh M\tau + \frac{\kappa + \gamma^0}{4M} \sinh M\tau)|^2, \qquad (2.60)$$

with  $M = \sqrt{[(\kappa - \gamma^0)/4]^2 - g^2}$  and  $\tau$  the time delay between the two detectors. Note that this expression is derived for the intracavity field, but the same result also applies to the transmitted field, since the field operators only differ by a scaling factor of  $\sqrt{\kappa/2}$ , which cancels out in Eq. 2.59.

In the cases of non-zero cavity and laser frequency detunings, the corresponding steadystate wavefunction can also be derived from the master equation, which results in the same expressions as Eqs. 2.57-2.60 with the following transformations

$$\kappa \to \kappa + 2i(\Delta\omega + \delta),$$

$$\gamma^0 \to \gamma^0 + 2i\Delta\omega.$$
(2.61)

We now focus on the intensity correlations at zero time delay. Using the approximation  $\gamma^0/\kappa \ll 1$ , we can simplify Eq. 2.60 to

$$g^{(2)}(0) = (1 - C^2)^2, (2.62)$$

which is only a function of the cooperativity C. The dependence of  $g^{(2)}(0)$  on C is displayed in Fig. 2.12. The solid black curve in the figure shows the results calculated using Eq. 2.62. The dashed red curve in the same figure displays  $g^{(2)}(0)$  calculated using Eq. 2.60, for a system with  $(\kappa, \gamma^0)/2\pi = (3, 0.04)$  GHz without assuming  $\gamma^0/\kappa \ll 1$ . The two curves only differ slightly in the limit of large cooperativities.

For a system with a small cooperativity factor in the range  $(0, \sqrt{2})$ , the intracavity field is antibunched at zero time delay. When C is larger than  $\sqrt{2}$ , the intracavity field is bunched and  $g^{(2)}(0)$  increases approximately quartically with C. In the special case of C=1, the intracavity field is perfectly antibunched, implying that only single photons can traverse the system. This is somewhat nonintuitive, since the system is driven by a coherent field. We will explain the reason for the perfect antibunching in the coming section.

### 2.4.2 Probability of two-photon transmission

The unconventional behavior of the intensity correlation can be explained with an intuitive picture, by comparing the one- and two-photon probabilities of the transmitted field to those of a coherent field.

In the limit of  $\kappa \gg g \gg \gamma^0$ , the high-order absorption and re-emission processes of a cavity photon by the emitter can be neglected and a substitution of  $a = (E+g\sigma_-)/(\kappa/2)$  can be applied [60]. The probability amplitude of one photon traversing the system can be calculated as

$$p_1 = \langle g, 0 | a | \psi \rangle = (\kappa/2)^{-1} {}_e \langle g | (E + g\sigma_-) \otimes {}_c \langle 0 | \psi \rangle = \frac{E}{\kappa/2} \cdot \frac{1}{1+C}, \qquad (2.63)$$

where the subscript e and c denote the state of the emitter and the cavity, respectively. The probability amplitude for the simultaneous transmission of two photons is

$$p_{2} = \langle g, 0 | a^{2} | \psi \rangle = (\kappa/2)^{-2} {}_{e} \langle g | (E^{2} + 2Eg\sigma_{-} + g^{2}\sigma_{-}^{2}) \otimes {}_{c} \langle 0 | \psi \rangle$$

$$= E^{2} / (\kappa/2)^{2} + 2EgB / (\kappa/2)^{2}$$

$$= \frac{E^{2}}{(\kappa/2)^{2}} \cdot \frac{1 - C}{1 + C}.$$
(2.64)

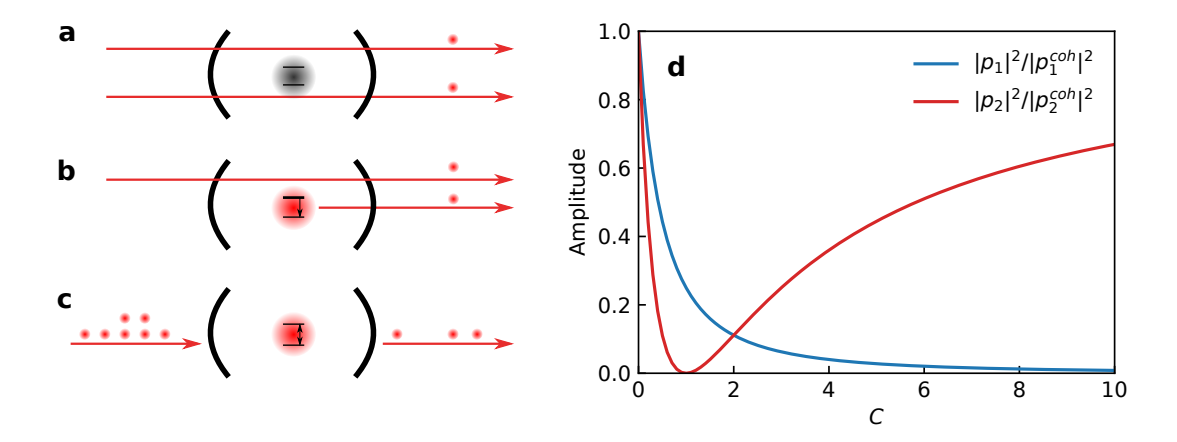


**Figure 2.13: a**, Two photons traverse the cavity without interacting with the emitter. **b**, One photon traverses the cavity, and a second one is emitted by the emitter. **c**, At C = 1, the coupled system works as a single-photon filter. **d**, Probabilities of one- and two-photon transmission as a function of C, normalized to the corresponding values for an empty cavity.

The first term in the second line of the equation represents the probability amplitude of having two photons traversing the cavity without interacting with the emitter (see Fig.  $2.13\,\mathrm{a}$ ), while the second term corresponds to one photon traversing the cavity and a second photon emitted by the emitter (see Fig.  $2.13\,\mathrm{b}$ ). At C=1, the probability of two-photon transmission is zero, which is a result of total destructive interference of the two probability amplitudes. In this particular situation, only single photons can traverse the system. The transmission is therefore perfectly antibunched (as shown in Fig. 2.12). The system can thus be used to construct a single-photon filter, i.e. a weak coherent light incident onto the system, but only single-photons traverse it, as depicted by Fig.  $2.13\,\mathrm{c}$ .

In the last step, we compare the probabilities of one- and two-photon transmissions  $(|p_1|^2, |p_2|^2)$  to those of a coherent field  $(|p_1^{\text{coh}}|^2, |p_2^{\text{coh}}|^2)$ . Note that for the coherent field,  $|p_2^{\text{coh}}| = |p_1^{\text{coh}}|^2$  and thus  $g^{(2)}(0) = 1$ . The deviations of  $p_1$ ,  $p_2$  from the values of a coherent field lead to the changes in photon statistics. In Fig. 2.13 d, the ratios  $|p_1|^2/|p_1^{\text{coh}}|^2$  and  $|p_2|^2/|p_2^{\text{coh}}|^2$  are plotted as functions of C. To arrive at the values of  $p_1^{\text{coh}}$  and  $p_2^{\text{coh}}$ , we used Eqs. 2.63, 2.64 and set C = 0. The two ratios thus represent the probabilities of one- and two-photon transmissions normalized to those of an empty cavity. The blue line displays the one-photon transmission probability, which decreases monotonically with C. The two-photon transmission probability shown by the red line decreases with C for C < 1 and increases when C > 1. In the limit of  $C \to \infty$ , the one-photon transmission approaches zero whereas the two-photon transmission reaches one. This is an extreme regime of single-photon nonlinearity, where the one-

photon components in an incoming coherent field are completely reflected, while the two-photon components traverse the system with unit probability.

It is noteworthy to mention a special value of C. When  $C = \sqrt{2}$ , the two-photon transmission probability  $|p_2|^2 = [(\sqrt{2} - 1)/3]^2$ , which is equal to the square of the one-photon probability  $|p_1|^2 = (\sqrt{2} - 1)/3$ , implying that the Poissonian statistics are not altered at zero time delay. This is confirmed by the value of  $g^{(2)}(0)$  which is 1 for  $C = \sqrt{2}$ . When  $C < \sqrt{2}$ ,  $|p_2|^2$  is smaller than the square of  $|p_1|^2$ . It is thus less probable to find two photons in the transmitted light compared to a coherent field, which explains the antibunching at zero time delay in this regime (see Fig. 2.12). Vice versa, when  $C > \sqrt{2}$ , the one-photon transmission is suppressed more than the two-photon transmission. The transmitted light is thus bunched in this regime.

# Chapter 3

# **Experimental platform**

In this chapter, we introduce the experimental setups and the key techniques enabling the measurements reported in this thesis. In section 3.1, we first explain the fabrication of thin anthracene crystals doped with dibenzoterrylene molecules and the experimental methods for single molecule detection. In section 3.2, we present the design of the microcavity, discuss its key features and outline the major challenges in realizing a cavity with small mode volume. In section 3.3, we introduce the focused-ion-beam milling technique for fabricating micromirrors with a radius of curvature (ROC) as small as  $2.5 \,\mu\mathrm{m}$ . The metallic and dielectric coatings of the mirrors are also introduced. To facilitate the experiment with the microcavity, three generations of mechanical assemblies and two optical setups were built in a progressive manner. The first generation of cavity assembly was constructed for room-temperature operations, aiming at characterizing microcavities with small-ROC mirrors. This cavity and the room-temperature optical setup are described in section 3.4. After the characterizations, the second generation of the cavity assembly was constructed for cryogenic operations of a cavity with a finesse of 200. This cavity assembly featured a passive stability of 0.6 nm and was not sufficient for the operation of a high-finesse cavity. In the third generation, an improved mechanical design was implemented, where a passive stability of 20 pm could be achieved. The two generations of cryo-microcavities and the cryogenic optical setup are introduced in section 3.5. In the last section of this chapter, we outline the measures for passive and active stabilizations of the cavity inside the cryostat.

## 3.1 Single-molecule sample preparation and detection

The experiments presented in this thesis are performed with dibenzoterrylene (DBT) molecules doped in thin anthracene (Ac) crystals. In this section, we introduce the fabrication of DBT-doped Ac crystals and explain the selective addressing of single molecules using high resolution spectroscopy.

### 3.1.1 Sample preparation

The molecular structures of DBT and Ac are illustrated in Fig. 3.1 **a**. A DBT molecule can be inserted into the Ac lattice by replacing three Ac molecules [41]. Two possible insertion schemes are shown in Figs. 3.1 **b** and **c**. The photophysics of DBT molecules in these two sites were studied in Ref. [52]. In our experiments, we used only molecules in the main site (shown in Fig. 3.1 **b**) with the 00ZPL transition lying around 783 nm.

A vapor-phase growth method [62] is employed to fabricate thin DBT-doped Ac crystals of high optical quality, which is favorable for the integration in a microcavity. First, DBT molecules (obtained from Dr. W. Schmidt, Laboratory for PAH Research, Greifenberg, Germany) are pre-mixed with melted Ac (Zone-refined,  $\geq 99\%$ , Sigma-Aldrich Co. LLC.) in a nitrogen glove box. A small amount of the mixture is placed in a home-built sublimation chamber (see Fig. 3.1 d) and heated to 220 °C under one bar of nitrogen atmosphere. After the mixture has melted, the chamber is flushed with cold nitrogen gas. Ac/DBT vapor in the chamber begins to condensate and thin Ac crystals develop along their (a-b) plane [63]. A clean glass cover slip is placed at the top of the chamber to collect the condensed crystals. After sufficient Ac crystals are attached to the cover slip, it is removed from the chamber. In the last step, the cleaned planar mirror of the microcavity is pressed gently against the cover slip to transfer a few Ac crystals to its surface.

Figure 3.1 e displays an optical microscope image of Ac crystals after transferred to the surface of the planar mirror. The image is acquired in cross-polarized mode, where the crystals appear colorful due to their birefringence. The lateral size of the crystals varies between 50 to 500  $\mu$ m and their thickness lies in the range from 0.1 to 5  $\mu$ m. To obtain the thickness of individual crystals, we perform topographic measurement using an atomic force microscope (AFM). An example of the measured topography of an Ac crystal is displayed in Fig. 3.1 f. A cross sectional scan along the direction marked by the dashed horizontal line in Fig. 3.1 f is displayed in Fig. 3.1 g, revealing the thickness of this crystal ( $\sim 100 \, \mathrm{nm}$ ).

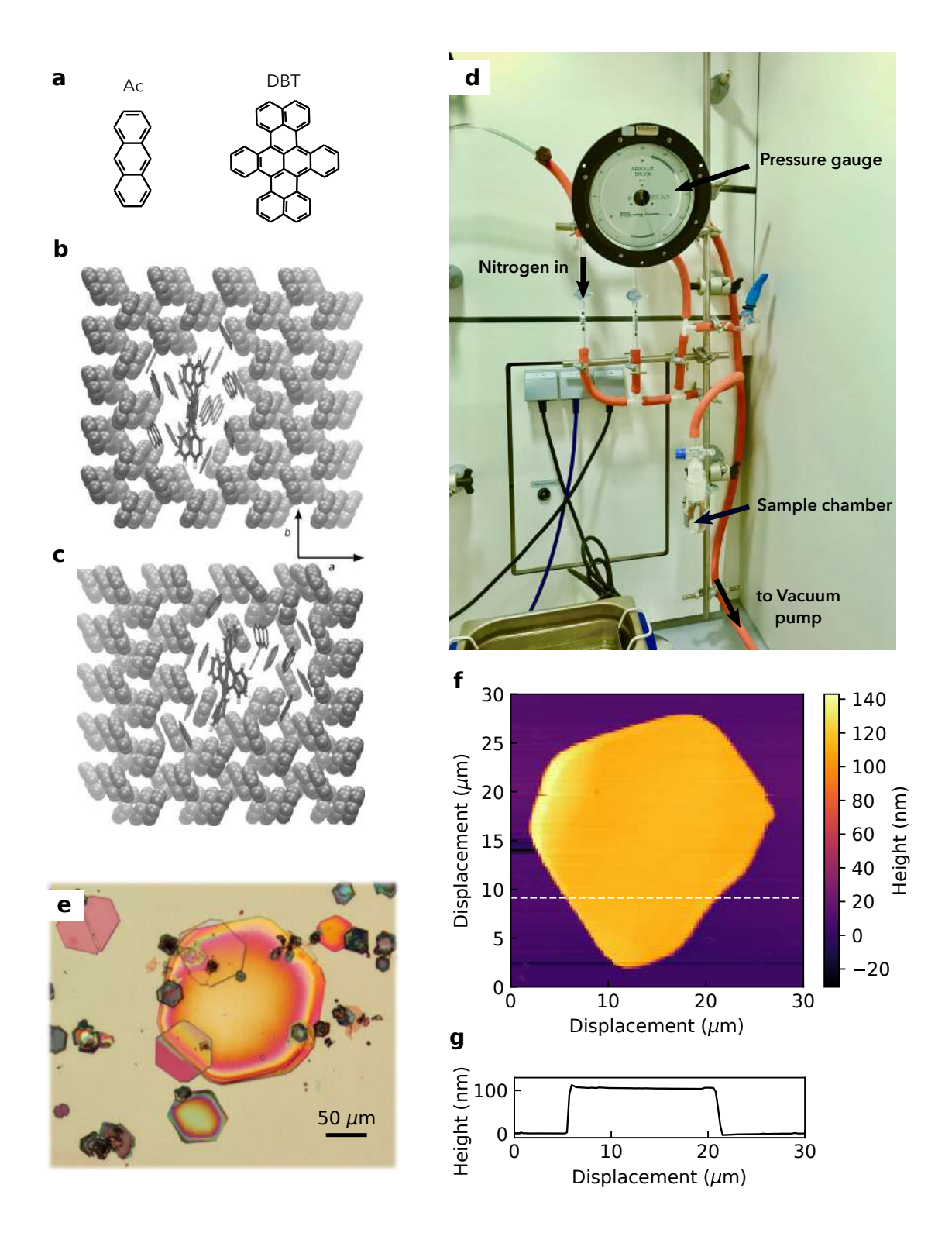


**Figure 3.1: a**, Molecular structures of Ac and DBT. **b**, **c**, The main and the red insertion sites of a DBT molecule in the Ac lattice, respectively. In both configurations, three Ac molecules are substituted by a DBT molecule. Reprinted from Ref. [41] with permission from WILEY-VCH Verlag GmbH. **d**, The home-built Ac sample preparation apparatus. **e**, An optical microscope image of DBT-doped thin Ac crystals on the planar mirror, acquired in cross-polarized mode. **f**, **g**, Topography of one Ac crystal measured using an AFM and a cross-sectional scan along the horizontal dashed line in **f**, respectively.

#### 3.1.2 Single-molecule detection

Using the vapor-phase growth method, we obtain weakly doped crystals with about 20 to 50 molecules per confocal spot ( $\sim 700\,\mathrm{nm} \times 700\,\mathrm{nm}$ ). Access to a single molecule can be gained by exploiting the inhomogeneous broadening of the molecular spectra in the crystal.

When cooled down to  $T \sim 4\,\mathrm{K}$ , the 0-0 zero-phonon lines (00ZPL) of DBT molecules narrow down to their Fourier limit of about 40 MHz [41,64]. As we observed in the experiment, cooling down to 1.4 K does not lead to further line narrowing, which is in accordance with the studies in Ref. [41]. Being embedded in a solid-state environment, each molecule experiences a slightly different local environment (including electric field, strain, etc.) and acquires a different shift in its energy levels. As a result, the frequencies of the 00ZPLs normally span over several hundred gigahertz. The difference in the transition frequencies, also referred to as the inhomogeneous broadening, provides an extra degree of freedom for selectively addressing single molecules.

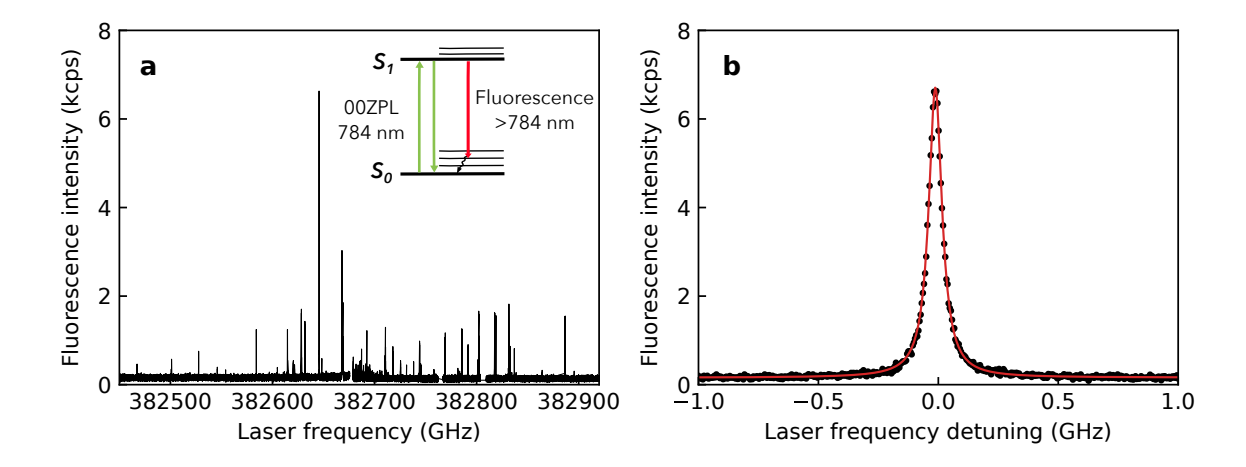


**Figure 3.2:** a, Fluorescence excitation spectrum of one confocal spot on the crystal, showing the inhomogeneous broadening of the molecules. Individual sharp peaks represent single molecules. The inset displays a simplified energy diagram of a DBT molecule. The molecules are excited via their 00ZPL transitions and the red-shifted fluorescence is detected. **b**, A close-up of the spectrum of a single molecule. The red line represents a fit to a Lorentzian function.

Single molecules are commonly detected by observing their fluorescence signals [22, 65]. Figure 3.2 a displays the intensity of the red-shifted fluorescence from a confocal spot on the crystal, when the frequency of a narrow-linewidth (< 1 MHz) laser is tuned across the inhomogeneous broadening of the 00ZPLs (see inset of a for the

excitation and detection schemes). The sharp peaks in the plot represent individual molecules, whose frequencies span over around 500 GHz. A close-up of the fluorescence spectrum of a single molecule is displayed in Fig. 3.2 b. The red line represents a fit to a Lorentzian function, with a FWHM of  $66.8 \pm 0.2 \,\mathrm{MHz}$ . The excellent agreement of the measured data and the fit confirms that the fluorescence signal is the result of a single-exponential decay. We note that a second-order intensity-correlation measurement on this fluorescence signal will provide the final proof that it stems from a single molecule. In this example, the linewidth of the Lorentzian profile is larger than the natural linewidth ( $\sim 40 \,\mathrm{MHz}$ ), due to a slight power broadening.

We note that apart from the fluorescence detection, single molecules can also be identified in the transmission signal of a laser beam impinging on it. Details of this scheme will be explained in chapter 5.

## 3.2 Cavity design

Many pioneer experiments in cavity-QED were carried out using atoms in ultrahigh vacuum and macroscopic Fabry-Pérot cavities [28, 34, 35] (see Fig. 3.3 a). Incremental developments in the cavity design and the atom manipulation have led to the strong coupling of a single atom to a cavity mode at both microwave and optical frequencies [66, 67]. The success of this approach has benefited greatly from the developments of super-polished substrates and high-reflectivity coatings using superconductors [66] or multilayer dielectrics [68, 69]. For cavities operating at optical frequencies, finesse of  $2 \times 10^6$  and quality factor of up to  $10^{10}$  were reported [68]. The ROC of these mirrors are normally in the order of millimeters, the length of the cavity is typically about  $100 \,\mu\mathrm{m}$  and the mode waist a few tens of microns. The resulting large mode volume  $(\gtrsim 1000 \,\mu\text{m}^3)$ , only allows a coupling strength in the order of 10-100 MHz. Even under a most optimistic assumption of achieving a  $\lambda/2$ -cavity, the coupling strength is limited to less than 650 MHz [69]. In many applications such as quantum communication and quantum information processing, it is desirable to implement operations at a higher speed (achieve a larger bandwidth). It is therefore, beneficial to use cavities with a smaller mode volume.

The combination of cavity-QED with solid-state physics brought the field into a new regime, where an artificial atom (quantum dot) and an optical resonator can be fabricated on a single chip. Using micro-pillar [70,71] or photonic crystal cavities [72] (see Fig. 3.3 b, c), the optical fields can be confined down to a mode volume of a few  $\lambda^3$ , thus boosting the coupling strength to the order of 1-10 GHz. The larger coupling strength

40 3.2. Cavity design

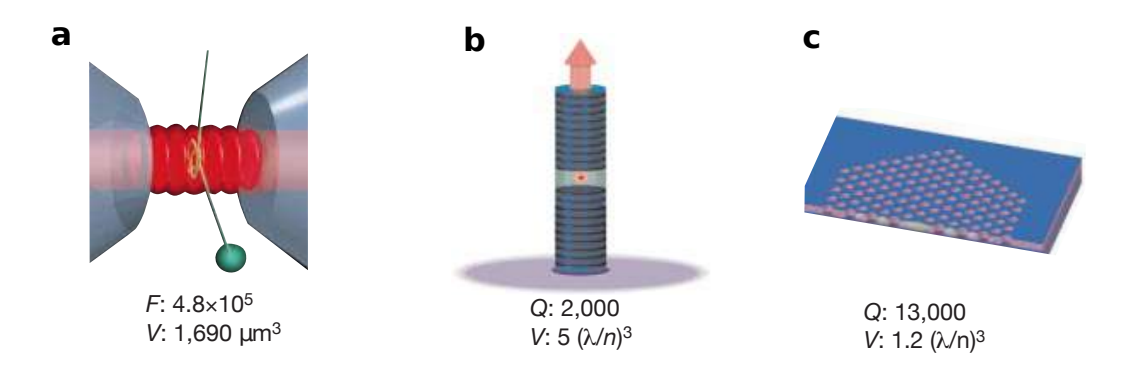


Figure 3.3: a, Fabry-Pérot cavity with mascroscopic mirrors. b, c, Micro-pillar and photonic crystal cavities. Reprinted from Ref. [25] with permission from Springer Nature.

has led to the observations of strong coupling with a single quantum dot [71,72] and enabled the realizations of on-chip high-brightness single-photon sources [73].

The fabrication of these devices is however, engaged and only applicable to specific groups of materials. The monolithic nature on one hand ensures the robustness of the device, on the other hand limits the control over the cavity and the emitter frequencies. Typically, many devices are produced in one fabrication run and the devices with suitable parameters are chosen for the experiments.

An alternative approach to achieve small mode volume is by miniaturizing the open Fabry-Pérot cavity. By fabricating mirrors with small ROCs on micro-pedestals [74–79], open Fabry-Pérot microcavities with mode volume smaller than one  $\lambda^3$  has been achieved [79]. Figure 3.4 illustrates the geometry of a hemispherical Fabry-Pérot microcavity. The cavity consists of a planar mirror and a curved micromirror fabricated at the end of a micro-pedestal. In the Gaussian approximation, the cavity mode has its waist (with 1/e half width  $w_0$ ) at the planar mirror, where a thin sample doped with single emitters is placed on. The cavity features easy tunability and scannablity. The open access of the microcavity also makes it applicable to different species of emitters. Indeed, experiments in recent years have demonstrated coupling of quantum dots [80–82], color centers in diamond [33,83–86] and molecules [64,77,79] to microcavities of this geometry. Furthermore, the open feature also makes the cavity an attractive platform for chemical and biological sensing [79,87], enhanced microscopy and spectroscopy [88–90] and applications in cavity optomechanics [79,91].

The mode volume of a hemispherical Fabry-Pérot cavity can be estimated as [76]

$$V = \frac{\pi}{4}w_0^2 L,\tag{3.1}$$

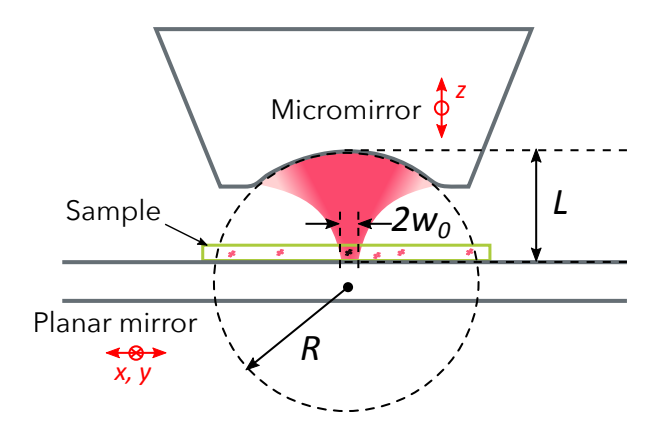


**Figure 3.4:** Illustration of a hemispherical microcavity consisting of a curved micromirror and a planar mirror. A thin layer of sample doped with single emitters is placed on the planar mirror. The resonance frequency of the cavity can be tuned by adjusting the micromirror in the axial (z) direction. The planar mirror can be scanned laterally (along the x-y plane) to deterministically position an emitter at the center of the mode. L, R and  $w_0$  denote the cavity length, ROC of the micromirror and the mode waist, respectively.

where L is the cavity length and  $w_0 = (\lambda^2 L R/\pi^2)^{1/4}$  is the mode waist, with R the ROC of the curved mirror. In order to achieve a small V, it is necessary to reduce both the ROC and the cavity length.

A few challenges lie in the experimental realization of such an open, small mode volume cavity. First, in order to reach a mode volume of  $\lambda^3$ , one need both L and  $w_0$  in the order of  $\lambda$ . This requires to use a curved mirror with  $R < 16\lambda$  (when assuming  $L = \lambda$ ), i.e. the ROC need to be smaller than  $12.5\,\mu\mathrm{m}$  for the operation at 785 nm. Note that the estimation of mode volume using Eq. 3.1 does not include the effect of field penetration into the dielectric coatings. The restriction on R for a cavity with dielectric mirrors is thus more strict. Second, the mirror need to be structured on a microscopic plateau, so that it can be brought close enough to the planar mirror to form a cavity with length of  $\lambda$ . Third, the assembly of the microcavity, including the two mirrors, in- and out-coupling optics, slip-stick piezoelectric sliders enabling the coarse tuning and piezoelectric transducers for fine control of cavity length need to be integrated on the insert of the cryostat, which has a diameter of 5 cm and a height of 10 cm. Lastly, despite the requirements on compactness and flexibility, the mechanical assembly has to be rigid, so that it maintains a proper passive stability of the cavity in the complex cryogenic environment. For example, for a cavity with finesse of 10,000, the linewidth of the resonance in length is 40 pm. Keeping a cavity stable to this order is challenging due to the mechanical and acoustical noise introduced by the operation of the cryostat.

We will outline our solutions to these issues in the coming sections of this chapter.

#### 3.3 Micromirror fabrication

An established technique for fabricating curved micromirrors is  $CO_2$ -laser ablation, where a single (or a few) high energy laser pulse is used to produce a Gaussian-shaped concave structure on a glass substrate [74–76]. This method can result in very smooth surfaces with root-mean-square surface (RMS) roughness less than 0.2 nm [75]. The high surface quality allows the adoption of high-reflectivity dielectric coatings, with which cavities with finesse larger than  $10^5$  were reported [76,92]. On the other hand, this technique faces its limit in machining spherical mirrors with ROCs smaller than  $20 \,\mu\text{m}$ , due to the Gaussian beam profile and the diffraction-limited spot size of the  $CO_2$ -laser.

We use focused-ion-beam (FIB) machining [93] to fabricate micromirrors for the experiment. FIB is a technique capable of fabricating mirrors with ROCs below  $10 \,\mu\mathrm{m}$  and offers nanometer-level topographic control on varies materials [79,84,94]. In this section, we introduce the principle of FIB, the fabrication of micromirrors with ROCs in the range  $2.5 - 10 \,\mu\mathrm{m}$  on silicon and glass substrates and the three types of coatings applied on the mirrors.

#### 3.3.1 Focused-ion-beam machining

Gallium ion (Ga<sup>+</sup>) is the most widely used ion spieces in commercial FIB instruments. The operation principle of a gallium FIB apparatus is illustrated in Fig. 3.5 a. First, a piece of gallium metal is heated to its melting point and wets around a tungsten tip. A large bias voltage is applied across the tungsten tip and the extractor electrodes, which induces ionization and field emission of the gallium atoms at the end of the tip. The emitted ions with energy up to 50 keV are collimated by a set of electrostatic lenses and are spatially selected using an aperture. After passing the aperture, the propagation direction of the ion beam is scanned by a set of deflection electrodes. Finally, an objective lens focuses the ion beam onto the sample surface with a focal spot size below 10 nm. Upon hitting the sample, the high-energy ions sputter the local atoms away, thus enabling nanometer-resolution structuring on the sample surface [93].

Figures 3.5 **b-e** display a series of images acquired during the machining process of a micromirror on a silicon substrate, taken by the in-built scanning electron microscope (SEM) of the FIB setup. In this example, gallium ions with an energy of 30 keV and a total ion-current of 50 pA are focused onto a planar silicon substrate (see Fig. 3.5 **b**). The focal spot of the ions is scanned in a circular pattern with a step size of 10 nm and

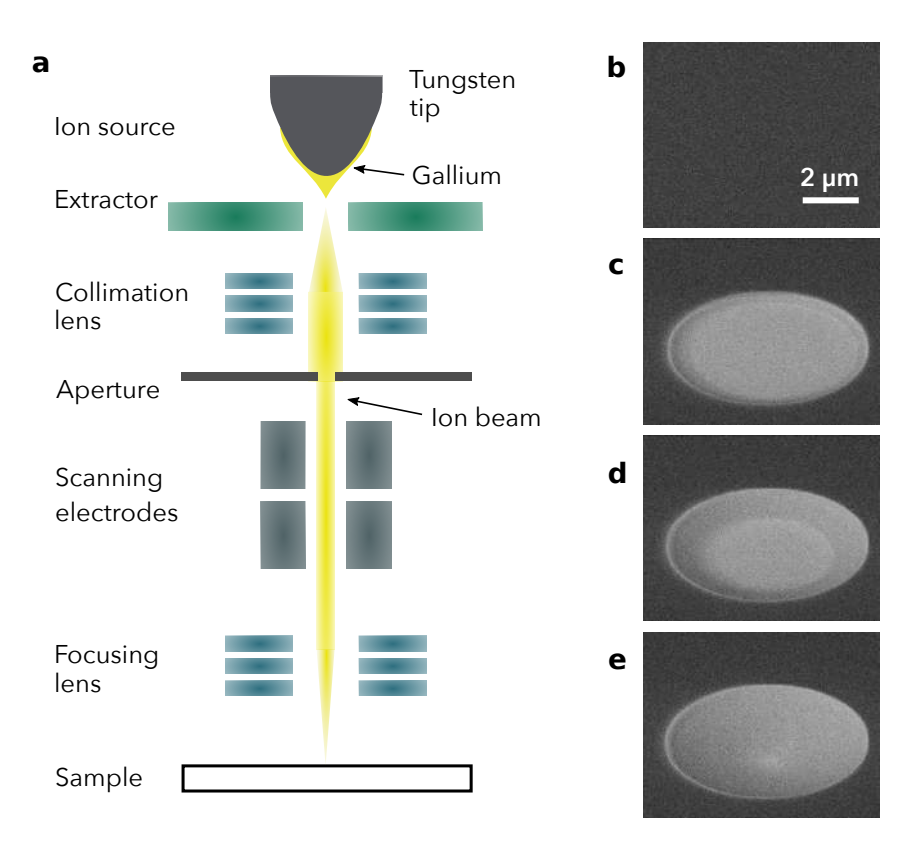


**Figure 3.5:** a, Illustration of a gallium-ion FIB setup. See text for details. b-e, Scanning electron microscope images acquired during the machining process of a micromirror on a silicon substrate.

a hemispherically shaped mirror is milled layer after layer (see Fig. 3.5 c-e). We note that the conductivity of doped silicon substrates ensures fast neutralization of positive changes deposited on the sample surface. The machining of silicon using focused  $Ga^+$  ions has also been well-studied [95,96]. When machining on non-conductive materials such as fused silica, a flood of low-energy electrons are sprayed onto the substrate after every layer to neutralize the deposited positive charges. The total machining process lasts about five minutes for a mirror with a ROC of  $10 \,\mu\text{m}$  and a depth of  $500 \,\text{nm}$ .

Figure 3.6 a shows an SEM image of four micromirrors machined on the tip of a silicon AFM cantilever. A topographic measurement is performed on one of the mirrors using an AFM, as shown by the black line in Fig. 3.6 b. The mirror has an opening aperture of  $\sim 2.2 \,\mu\text{m}$  and a depth of 250 nm. The green line in the same plot represents a fit to a circle, yielding a ROC of 2.3  $\mu$ m and a RMS deviation of 3.6 nm. Being fabricated at the tip of an AFM cantilever, the micromirror has several attractive features apart from its small ROC: first, the micromirror can be brought close to contact with a planar mirror to form a cavity with sub- $\lambda^3$  mode volume (see section 3.4); second,

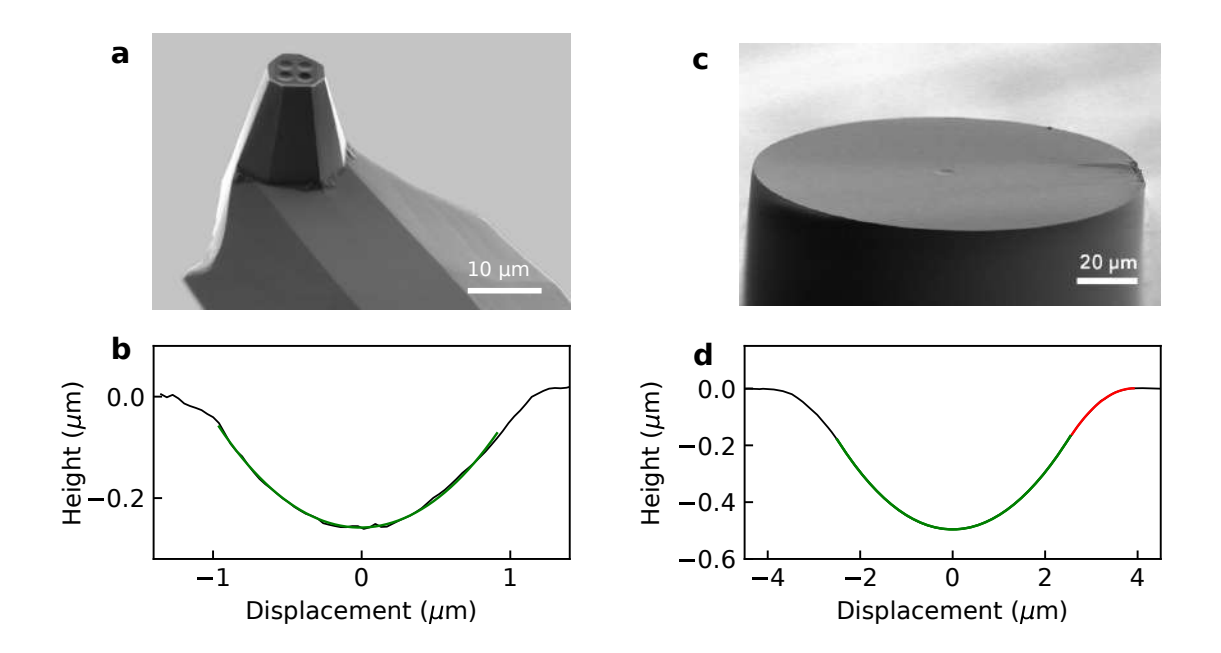


**Figure 3.6: a**, SEM image of four micromirrors machined on the tip of a silicon AFM cantilever. **b**, The black line displays an AFM cross sectional scan across the center of one of the mirrors shown in **a**. The green line represents a circular fit. **c**, A SEM image of a micromirror fabricated at the cleaved end of a fused-silica fiber. **d**, The black line shows an AFM cross sectional image across the center of the micromirror shown in **c**. The green and the red lines represent fits to a circle.

despite the small mirror separation, the cavity is tunable and scannable like a common AFM; third, the cantilever supports mechanical resonances with the fundamental mode at frequency  $\sim 100\,\mathrm{kHz}$ . The resonance frequency can be increased to 5 MHz when using a low-mass cantilever, thus enabling an optomechanical coupling strength in the order of 1 MHz [79], making it an attractive platform for applications in cavity optomechanics [91].

The surface quality of the micromirrors can be improved by switching to amorphous substrates such as fused silica. The SEM image in Fig. 3.6 c displays a micromirror machined at the cleaved end of a single-mode fiber made of fused silica with a diameter of 125  $\mu$ m. The black line in Fig 3.6 d represents a cross sectional AFM scan across the center of the mirror, showing a hemispherical shape with an opening diameter of about  $7 \mu$ m and depth of 500 nm. The green curve represents a fit of the central region to a circle, yielding a ROC of 10.0  $\mu$ m. The maximal deviation of the measured data from the circular fit is about 1 nm and the RMS roughness of the mirror is less than 0.4 nm, which is limited by the resolution of the AFM. We note that it is not necessary to involve an additional polishing step to achieve this surface smoothness, since FIB provides an effective polishing due to the dependence of the sputtering rate on the

incident angle of the ion beam [94]. The red curve in Fig. 3.6 d represents a circular smoothening pattern with a ROC of 5.7  $\mu$ m. This was implemented to avoid sharp features around the edge and to ease the adoption of a multilayered dielectric coating.

In addition to the improved surface smoothness, fused silica is transparent in visible and near-infrared frequencies, thus providing a direct transmission channel of the cavity. The micromirror machined at the end of a single-mode fiber (shown in Fig.  $3.6\,\mathrm{c}$ ) is used for the experiments presented in chapter 5 and 6. However, a limitation of using a fiber is the finite coupling efficiency of the cavity mode to the guided mode. Ideally, one would use a micro-sized plateau structured on the fused silica substrate to host the micromirrors.

#### 3.3.2 Mirror coatings

After the FIB machining, the mirrors are coated with a metallic or dielectric layer to achieve a high reflectivity. Three types of coatings are used for the experiments reported in this thesis:

- Gold coating. The coating is deposited by an in-house thermal evaporator. A 10 nm-layer of titanium is first deposited on the mirror as a wetting layer, followed by 150 nm of gold. The deposition rate of titanium is  $0.2 \, \mathrm{nm/s}$  and that of gold is about  $0.5 \, \mathrm{nm/s}$ . The whole coating process takes about 10 minutes. Since the gold coating can easily be scratched, a 50 nm-layer of fused silica is deposited on top of the gold as a protective layer. Figure 3.7 a displays an optical microscope image of the same micromirror sample shown in Fig. 3.6 a after the gold coating. The coating has a reflectivity of 96% at wavelength 785 nm.
- Enhanced silver coating. The coating is deposited by Laseroptik GmbH, consisting of a 120-nm silver layer and a thin dielectric layer on top to enhance the reflectivity. Compared to common commercial silver coatings which have reflectivity of around 97% at 785 nm, the enhanced coating reaches a reflectivity of 99% at the same wavelength.
- Multilayer dielectric coating. The coating is also deposited by Laseroptik GmbH.
   The dielectric coating consists of alternating λ/4-thick layers of Nb<sub>2</sub>O<sub>5</sub>/SiO<sub>2</sub> or TiO<sub>2</sub>/SiO<sub>2</sub>. Twelve such bilayers are deposited on the substrate to reach reflectivities of up to 99.995%. Figure 3.7 b displays an optical microscope image of a micromirror machined at the cleaved end of an optical fiber after coating

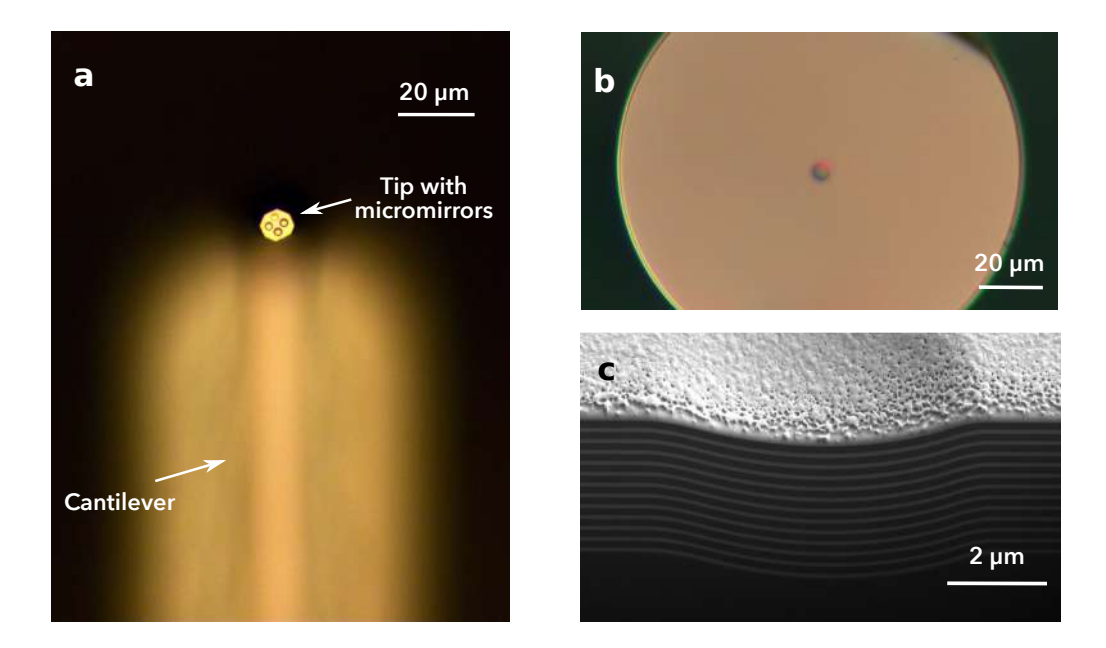


Figure 3.7: a, Optical microscope image of micromirrors structured on an AFM tip after the gold coating. The lower part of the image shows the cantilever supporting the tip, which is out of focus. b, Optical microscope image of the dielectric coated micromirror at the end of a fiber. c, SEM image of the multilayer dielectric coating on the micromirror shown in b. The mirror has a radius of curvature of  $10 \,\mu\text{m}$  and a depth of  $500 \,\text{nm}$ . The coating consists of 12 alternating layers of Nb<sub>2</sub>O<sub>5</sub> and SiO<sub>2</sub> and is cut by a focused ion beam. The apparent surface roughness is caused by the metallic coating necessary for imaging with the SEM.

with the dielectric layers. An SEM image of the dielectric coated micromirror after cutting by the FIB is shown in Fig.  $3.7 \, c$ .

We note that state-of-the-art dielectric coating can reach a reflectivity of 99.9998%, when applied to super-polished macroscopic mirrors, a cavity finesse of up to  $2 \times 10^6$  can be reached [68,69]. However, applying the dielectric coating to mirrors with ROCs down to a few micrometers can be problematic since the thickness of the coating and the feature size of the mirror become comparable. Studies by Trichet *et al* [94] suggest that a combination of mono-directional and isotropic growth interplays during the coating process and cracks tend to develop around the edge of the micromirror. Therefore, one has to pay special attention to the topography of the mirror to ensure the quality of the coating. To facilitate such a high-reflectivity dielectric coating on the micromirror, a circular smoothening pattern is applied to the edge area of the mirror during the FIB milling process, as shown by the red line in Fig. 3.6 **d** of the previous section.

Compared to the high-reflectivity dielectric coatings, the main advantages of metallic coatings are their easy fabrication and small optical penetration depths. The metallic

coated mirrors can be used to realize low-Q and small mode volume cavities (see also chapter 4).

## 3.4 Room-temperature setup

In this project, we used a cryogenic setup and an inverted microscope for sample characterization at room temperature. We now introduce the inverted-microscope setup and the first generation of microcavity assembly based on it. Using this setup, we investigated the performance of Fabry-Pérot cavities with mode volume smaller than  $\lambda^3$ , and demonstrated spatially-resolved nanoparticle sensing. The details of these experiments will be explained in chapter 4.

#### 3.4.1 Inverted microscope

The schematics of the inverted microscope setup is shown in Fig. 3.8. The microscope has two light sources. A light emitting diode (LED) serves as a white light source for wide-field imaging, and a diode laser (DL DFB, Toptica Photonics AG) is used for laser scanning microscopy (LSM). The two light sources can be switched with a flip mirror (FM). For the LSM measurements, the laser light is first sent through a polarization beam splitter (PBS) for polarization cleaning. The light transmitted through the PBS is focused onto the sample by an objective with a numerical aperture (NA) of 0.75. The sample is mounted on a three-dimensional piezoelectric transducer (PZT) stage (Model 3976, Piezosystem Jena GmbH), which is scannable up to  $100 \,\mu\mathrm{m}$  in all three dimensions. The reflected light (or fluorescence) from the sample is collimated by the same objective and separated from the incident laser beam using a beam splitter (BS). The reflected light from the BS is sent to a photodiode or a charge-coupled device (CCD) camera, controlled by a second flip mirror. To improve the passive stability of the system, the whole microscope is built on an active vibration-isolation stage (Halcyonics i4, Accurion GmbH) and is shielded with acoustic isolation foam on all sides.

## 3.4.2 Room-temperature microcavity assembly

The first generation of the microcavity was built on top of the inverted microscope. Figure 3.9 a illustrates the assembly of the microcavity. The planar mirror sits on a

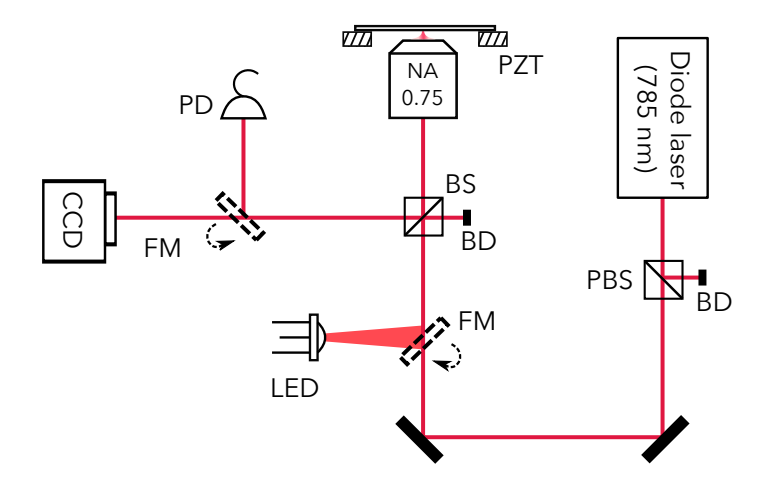


**Figure 3.8:** Schematic of the inverted microscope setup. PBS, polarization beam splitter; BD, beam dump; LED, light emitting diode; FM, flip mirror; BS, non-polarizing beam splitter; PZT, piezoelectric transducer; PD, photodiode; CCD, charge-coupled device.

three-dimensional PZT stage (pzt1) and lies parallel to the optical table. During the experiment, the planar mirror can be scanned in both lateral (x, y) directions parallel to the optical table (see also Fig. 3.9 b). The third (z) channel of pzt1 is grounded to avoid slow drift of the cavity length. The micromirror is fabricated on the tip of an AFM cantilever and coated with gold (see Fig. 3.6 a and Fig. 3.7 a). As shown in Fig. 3.9 b, the micromirror is fixed onto a triangular-shaped plate made of stainless steel, which is detachable from the base plate hosting the planar mirror. The triangular plate can be positioned on the base plate via a Maxwell kinematic coupling design [97].

Three fine-leveling screws are used to adjust the tilt of the top plate. A three-dimensional translation stage is mounted on the top plate to allow for coarse positioning of the micromirror. A second piezoelectric transducer (pzt2) with a travel range of  $15 \,\mu\text{m}$  in the axial (z) direction is glued at the end of the translation stage. A shear piezoelectric transducer (pzt3) is glued to the end of pzt2, which allows fine positioning of the micromirror along the two lateral (x, y) directions in an area of  $3 \,\mu\text{m} \times 3 \,\mu\text{m}$ . The incident light is focused by the objective on the planar mirror and coupled to the cavity. The reflected light is collected by the same objective and sent to the detection setup.

In chapter 4, we will discuss the experiments performed on this setup.

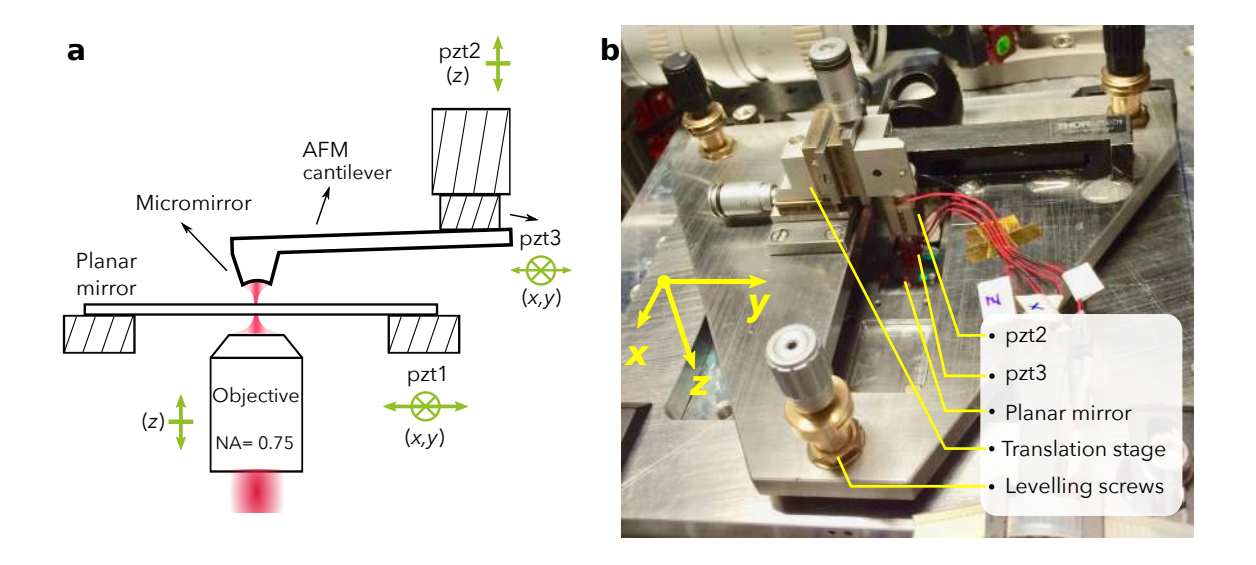


**Figure 3.9: a**, Schematic of the room-temperature microcavity assembly. **b**, A photograph of the microcavity assembly on top of the inverted-microscope. See text for details.

## 3.5 Cryogenic setup

Studying the coherent interaction of single molecules with the cavity mode requires cooling of the system to liquid helium temperatures [22]. For this purpose, the molecular sample and the microcavity are assembled in a liquid-helium cryostat (CryoVac GmbH) and cooled down to 4.2 K, which is the temperature necessary for a DBT molecule to reach its natural linewidth. In this section, we will introduce the cryogenic experimental setup, including the cryostat, its supporting optical setup and two generations of microcavities built on the cryostat insert.

## 3.5.1 The cryostat

As illustrated in Fig. 3.10, the cryostat is equipped with two liquid helium tanks and one liquid nitrogen tank. The upper helium tank has a volume of 6.4 liters and serves as a reservoir. It is refilled daily from an external dewar with a volume of 250 liters. During the experiment, the upper tank is maintained at 4.2 K and ambient pressure. The lower helium tank has a volume of 2.2 liters. It is in direct thermal contact with the sample chamber. The lower tank can be filled by transferring liquid helium from the upper tank. The two tanks are connected via a needle valve, which can be controlled manually. The pressure in the lower helium tank can be reduced to  $\sim 20$  mbar using a rotary vane pump. Under this pressure, the liquid helium in the lower tank becomes a

50 3.5. Cryogenic setup

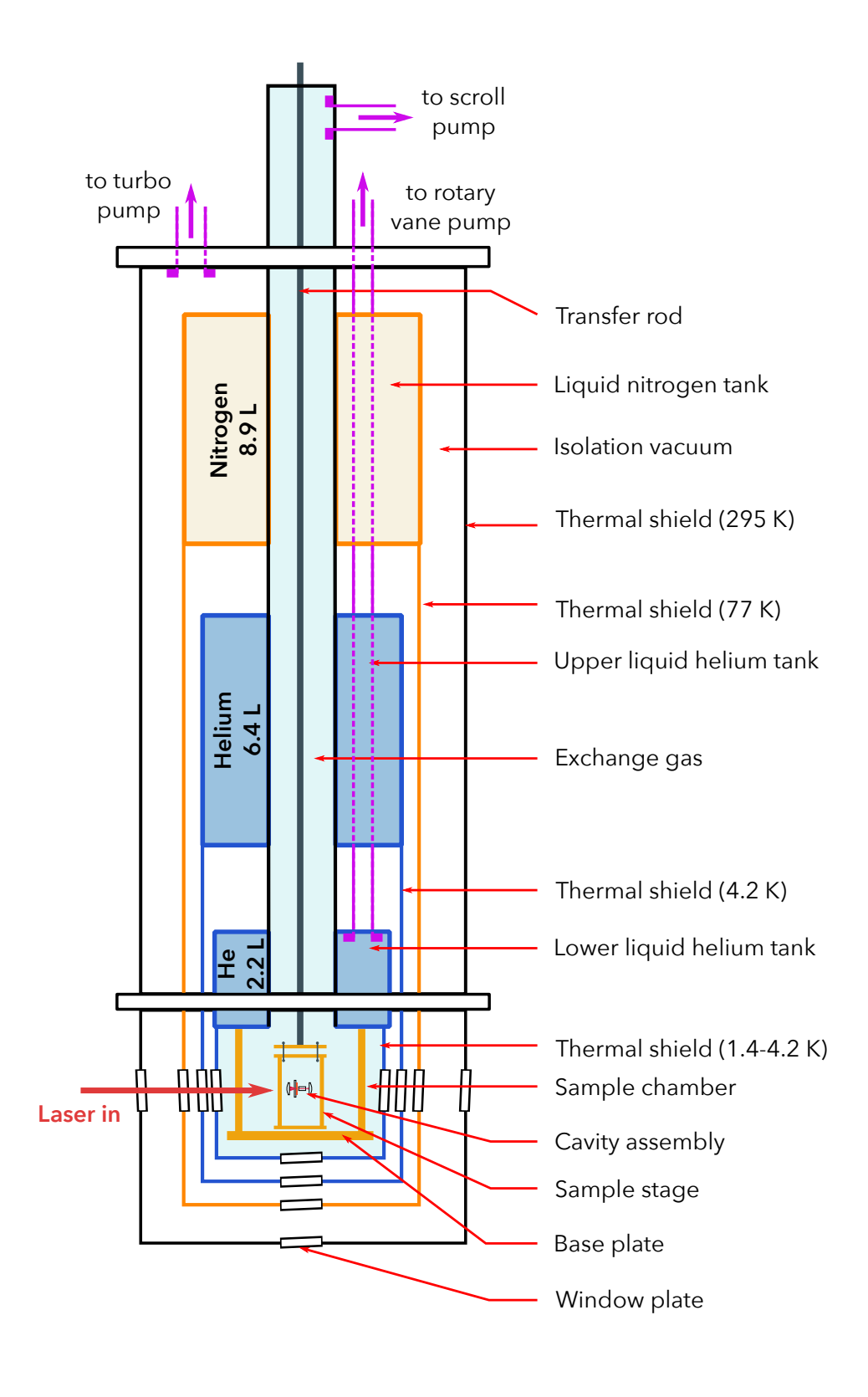


**Figure 3.10:** Structure of the liquid helium cryostat. The cryostat has two liquid helium tanks and one liquid nitrogen tank. The sample is cooled by the lower helium tank via an exchange gas. The sample chamber is isolated from the ambient environment by four layers of thermal shields. See text for details.

superfluid and can be cooled to 1.4 K. The liquid nitrogen tank has a volume of 8.9 liters and is designed to reduce the thermal evaporation rate of liquid helium. We note that the boiling of liquid nitrogen introduces significant vibrations to the microcavity in the sample chamber. It is therefore only refilled in the evening after the experimental operations and emptied before the next experimental run. On average, the cryostat consumes about 120 liters of liquid helium and 100 liters of liquid nitrogen per week for constant experimental operations at 4.2 K.

During the experiment, the sample chamber is filled with a helium exchange gas to improve the thermal contact of the sample with the lower helium tank. The pressure of the exchange gas is controlled by a scroll pump and is normally kept at around 50 mbar. The sample chamber is shielded from the ambient environment by four layers of thermal shields (see Fig. 3.10). The innermost shield is attached to the lower helium tank. The second shield is contact-cooled by the upper helium tank to 4.2 K. The third is attached to the liquid nitrogen tank and cooled to 77 K. The last shield is at room temperature. The chamber in between the four shields is evacuated to  $\sim 1 \times 10^{-6}$  mbar by a turbomolecular pump.

The microcavity is assembled on an insert attached to a transfer rod. The insert can be transferred out of (into) the cryostat by lifting up (down) the transfer rod without the necessity to warm up the cryostat. Considering the sensitivity of the cavity to mechanical vibrations, the insert is detached from the transfer rod after transferred into the cryostat and lands on a base plate via a Maxwell kinematic coupling mechanism [97]. The base plate is attached to the bottom of the lower helium tank. Two temperature sensors are used to monitor the temperature in the sample chamber. One is mounted on the base plate and the second is glued directly onto the sample stage.

The cryostat has five viewports. Four on the sides and one at the bottom. Each view port consists of four window plates mounted on the four thermal shields. The optical transmission through the four window plates is about 87% at 785 nm. The cryostat and its supporting optical setup is mounted on a pneumatically floated optical table to isolate it from the vibrations of the floor.

#### 3.5.2 Cryogenic microscope

The main optical setup is built around the cryostat to facilitate the measurements with the microcavity inside the cryostat. Figure 3.11 displays the schematics of the setup. Two lasers are employed for the normal experimental operation: a diode laser

52 3.5. Cryogenic setup

(DL Pro, Toptica Photonics AG) serves as a locking laser for the active stabilization of the cavity length and a Ti:sapphire laser (SolsTis, M Squared Laser Limited) is used as the probe laser for the measurements. The Ti:sapphire laser is mounted on a temperature stabilized (within  $\pm 0.1 \,\mathrm{K}$ ) optical table located in a neighboring lab. Its emission is guided to the experimental table via a single mode fiber. The diode laser is mounted directly on the experimental table. Each of the laser beams is sent through an acousto-optic modulator (AOM) for intensity stablization, and the resulting first-order diffraction is coupled to a single mode fiber for spatial-mode cleaning. After being coupled out from the fiber, each of the laser beams traverses a quarter-wave plate (QWP) and a half-wave plate (HWP) before they are combined at a beam splitter (BS). After the BS, the two beams are directed towards the cryostat via a common beam path. Before the cryostat, the laser beams are reflected by a steering mirror (SM: FSM-300, Newport Corporation), which scans their direction of reflection. A telecentric system with two  $f = 250 \,\mathrm{mm}$  lenses maps the direction of the reflected beams after the steering mirror to the incident direction at the back focal plane of the aspheric lens (Asph). The aspheric lens is mounted on the sample stage and focuses the light onto the planar mirror (PM). The steering mirror thus enables the lateral scanning of the focal spot on the planar mirror.

The light reflected from the cavity is collected by the same aspheric lens and separated from the incident light by a BS. The two laser beams are then separated using a BS and two interference filters. The polarization of the locking-laser beam is analyzed by a QWP in combination with a polarization beam splitter (PBS). The two outputs of the PBS are detected by the two channels of a balanced photodetector (BPD: OE-200, Femto Messtechnik GmbH). The output signal of the BPD provides the error signal for the active stabilization of the cavity [64, 98] (see also section 3.6). The probelaser beam first passes through a telescope consisting of two  $f = 100 \, \text{mm}$  lenses. A pinhole at the focal plane of the telescope allows performing confocal laser scanning microscopy on the sample. After the telescope, the laser beam can be directed to an avalanche photodetector (APD) for single-photon counting, to a Hanbury Brown and Twiss (HBT) setup for intensity autocorrelation measurement or to a scientific complementary metal-oxide-semiconductor (sCMOS) camera (Orca Flash 4.0, Hamamatsu Photonics) for imaging, controlled by two flip mirrors.

When a thin anthracene crystal is placed in the cavity, its strong birefringence allows us to access the intracavity fields at the reflection side exclusively [64]. To facilitate this, an HWP, a QWP and a polarizer (POL) are placed in front of the flip mirror to filter out the reflection from the planar mirror. The principle of the cross-polarized detection will be discussed in section 3.5.4.

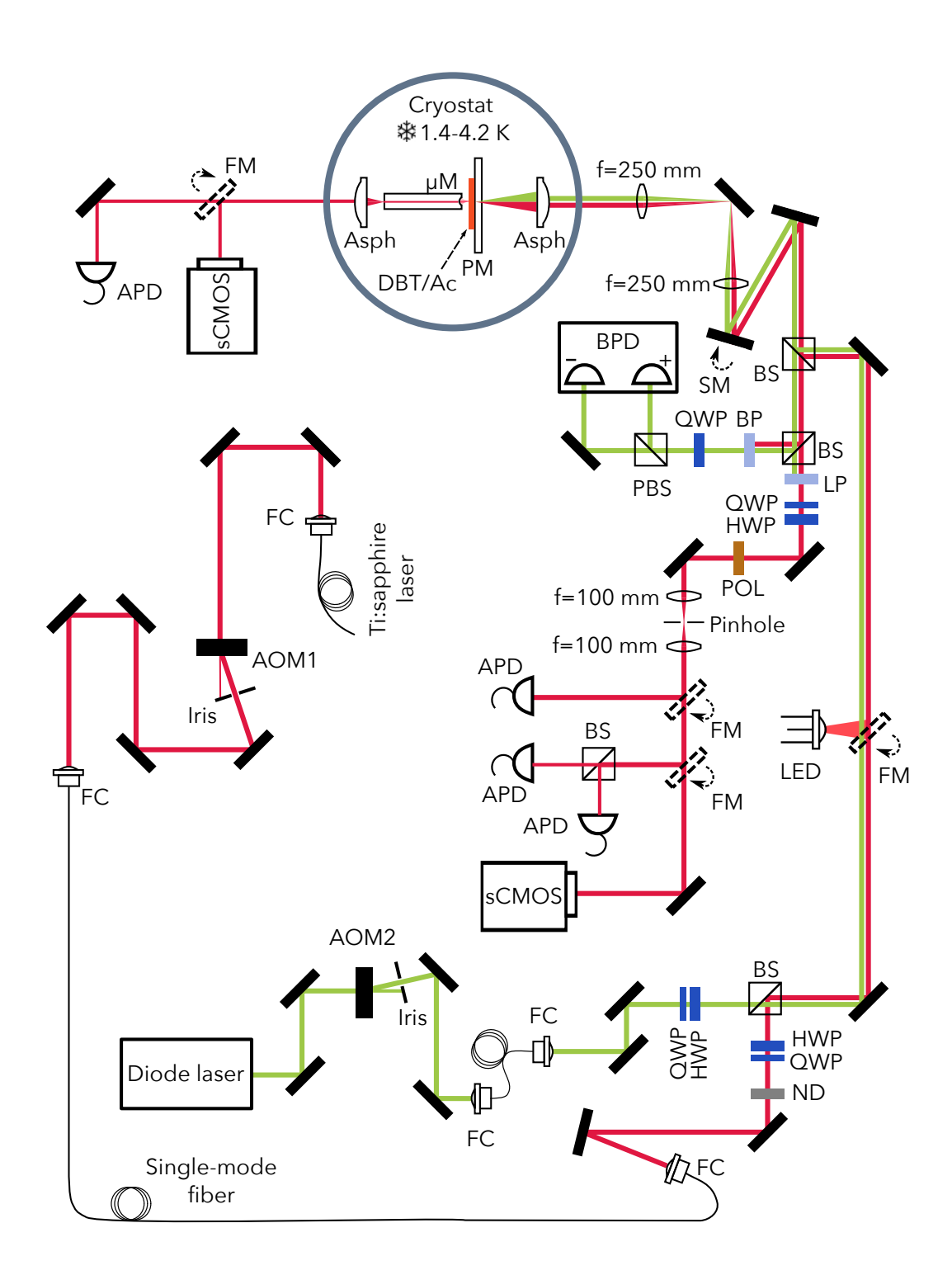


Figure 3.11: Main optical setup. AOM, acousto-optic modulator; FC, fiber coupler; ND, neutral-density filter; QWP, quarter-wave plate; HWP, half-wave plate; BS, non-polarizing beam splitter; LED, light emitting diode; FM, flip mirror; SM, steering mirror; Asph, aspheric lens; PM, planar mirror;  $\mu$ M, micromirror; DBT/Ac, DBT-doped thin anthracene crystal; BP, bandpass filter; LP, longpass filter; BPD, balanced photo detector; POL, linear polarizer; sCMOS, scientific complementary metal-oxide-semiconductor; PBS, polarization beam splitter. See text for details.

The microscope is also equipped with a transmission detection channel. The light transmitted through the sample is collected by a second aspheric lens and detected using an APD or an sCMOS camera. The sample can alternatively be illuminated by a LED for wide-field imaging.

#### 3.5.3 Low-temperature microcavity on the cryo-insert

Two generations of microcavities were assembled on the cryostat insert for studying the coupling of single molecules to the cavity. The first generation hosted a low-finesse cavity, in which the curved micromirror was fabricated on a  $50\,\mu\text{m}$ -wide and  $200\,\mu\text{m}$ -tall pedestal on a planar silicon wafer and coated with the enhanced silver coating. The planar mirror was a fused silica substrate coated with alternating layers of Nb<sub>2</sub>O<sub>5</sub>/SiO<sub>2</sub> at a design wavelength of  $700\,\text{nm}$ . This generation of cavity was used to demonstrate the coherent coupling of single molecules to a low-finesse cavity. We will discuss the details of this experiment in chapter 5.

Schematics of the first generation of the cryo-cavity are displayed in Figs. 3.12 a and b. The tunability and scannability of the cavity is realized by employing six slip-stick piezoelectric sliders (PESs) and two piezoelectric transducers (PZT). An aspheric lens (asph1: NA=0.55) is mounted on a PES (pes1: ANPx51, attocube systems AG) to couple light into the cavity and also collect its reflection. The planar mirror is mounted on a stack of two PESs (pes2: ANPx51, pes3: ANPz51, attocube systems AG) to enable lateral (x, y) scanning of the planar mirror across the cavity mode. The micromirror sits on a stack of three PESs (pes4, pes5: ANPx51, pes6: ANPx51), which provides the motional freedom in both the lateral (x, y) and the axial (z) directions. A ring piezoelectric transducer (Ring pzt) scans the axial (z) position of the micromirror during cavity alignment. Once a desired cavity mode is found, a DC voltage is applied to the ring piezo to bring the micromirror close to the resonance position. A second piezoelectric transducer (pzt2) is used for fast feedback control of the cavity length (see also section 3.6). The travel range of the PESs (3 mm) is enough to move the micromirror away from the optical axis of the incoming beam and enable the positioning of a second aspheric lens (asph2: NA=0.55) in the transmission path. This allows controlled measurements on the same molecule in and out of the cavity without removing the sample from the cryostat (see Fig. 3.12 b). The tilt of the micromirror with respect to the planar mirror is pre-aligned at room temperature by adjusting two tip-tilt screws on the micromirror mount. When cooled down to liquid helium temperatures, a shift of about 2° in the tilt is observed. A photograph of the cavity assembly is shown in Fig. 3.12 **c**.

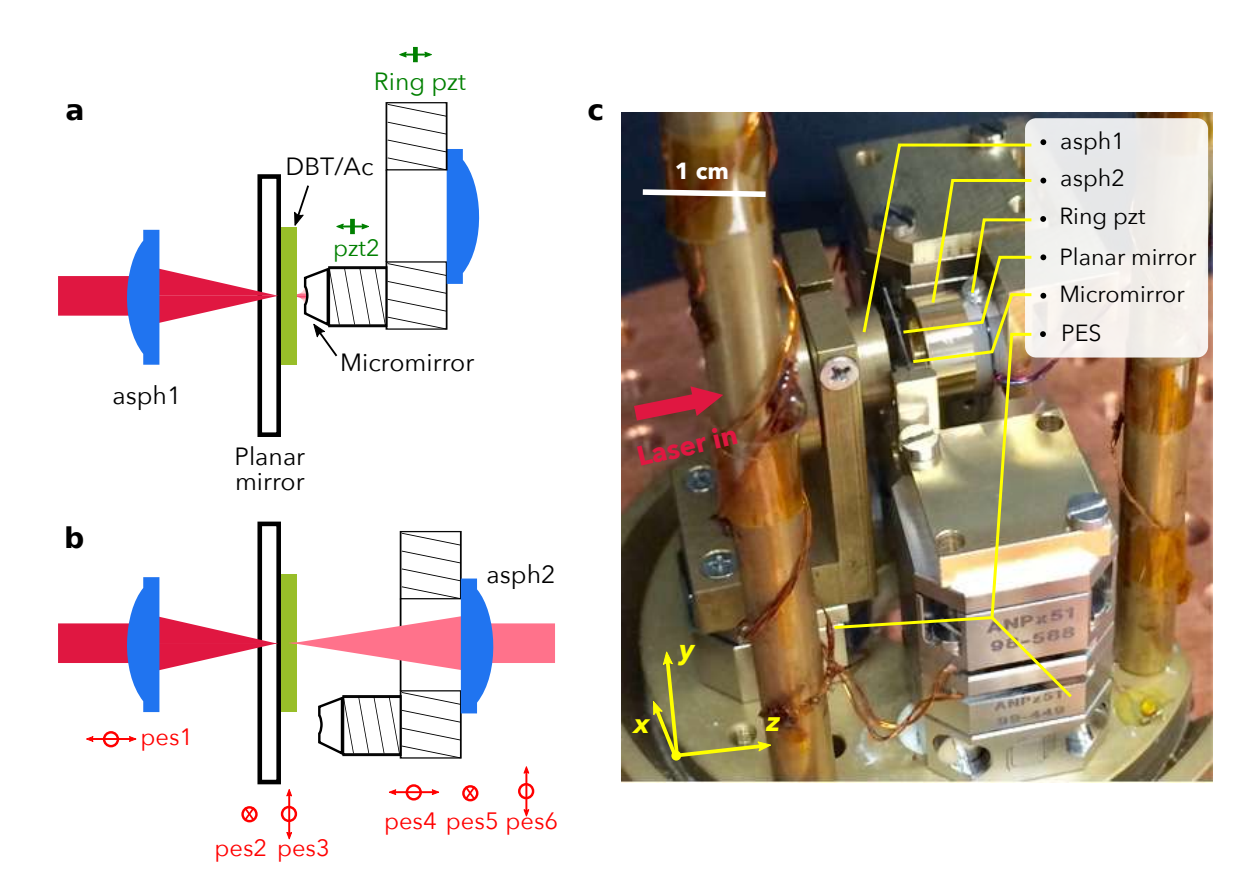


Figure 3.12: a, A schematic of the first generation of cryo-cavity when the micromirror is approached onto the planar mirror for the in-cavity measurements. b, The same as in a but for the out-of-cavity measurements. Here, the micromirror is retracted and displaced to allow a second aspheric lens aligned to the optical axis. Six slip-stick piezoelectric sliders (pes1-pes6) and two piezoelectric transducers (Ring pzt, pzt2) are employed to achieve full tunability and scannability of the cavity. DBT/Ac, DBT-doped thin anthracene crystal. c, A photograph of the microcavity assembly on the cryostat insert. The diameter of the insert is 5 cm. See text for details.

The finesse of the cavity with silver coated micromirror is limited to 200 due to the reflectivity of the coating ( $\sim 99\%$ ). In order to achieve stronger molecule-cavity coupling, we also applied the dielectric coating to the micromirror (see section 3.3.2). The dielectric coating consists of 12 alternating layers of  $\mathrm{SiO_2/Nb_2O_5}$ , reaching a nominal reflectivity of 99.995% and can support a finesse up to 60,000. Operating such a high-finesse cavity in the cryogenic environment poses significant challenges to the mechanical stability of the system. We thus modified the mechanical design of the first generation for improved passive stability.

Figure 3.13 a presents a schematic of the second generation of the cryo-cavity. The planar mirror is mounted on a PES (pes1: ANPz51) which positions the molecular sample in the lateral (y) direction. The micromirror is machined at the cleaved end of

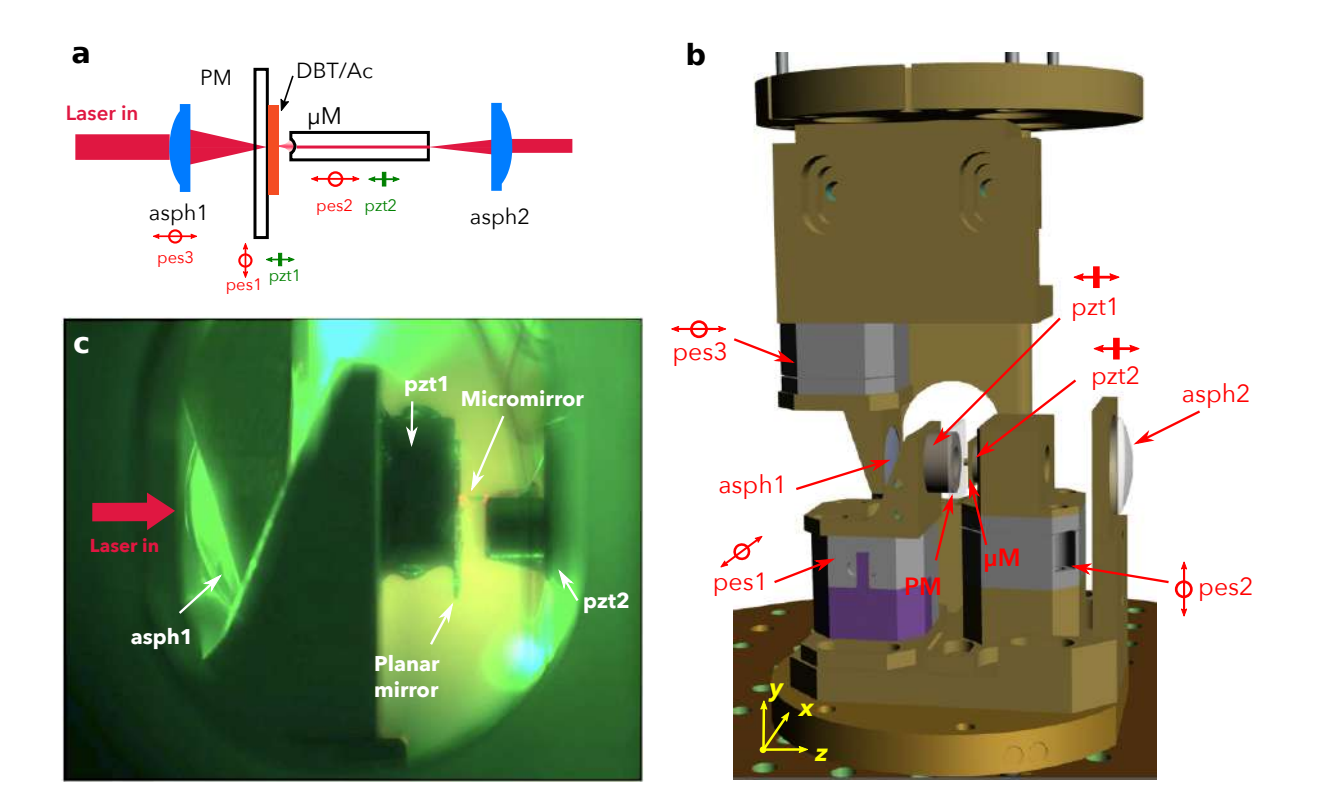


Figure 3.13: a, Schematic of the second generation of the cryo-cavity. The cavity is formed by the micromirror at the end of a single mode fiber and a planar mirror with a thin crystal attached to it. Light is coupled into the cavity by an aspheric lens (asph1) and the light transmitted through the fiber is collimated by a second aspheric lens (asph2). The red arrows denote the degree of freedom for the coarse alignment, provided by three slip-stick nano-positioners (pes1-pes3). The green arrows indicate the fine cavity length adjustments using two ring piezoelectric transducers (pzt1, pzt2). PM, planar mirror;  $\mu$ M, micromirror; DBT/Ac, DBT-doped thin anthracene crystal. b, CAD drawing of the cavity assembly. c, A photograph of the cavity assembly at 4 K, taken through a side window of the cryostat.

a single mode fiber, sits on a second PES (pes2: ANPx51) and travels along the axial (z) direction of the cavity. Each of the cavity mirrors is glued on a ring piezoelectric transducer (pzt1, pzt2) to facilitate the fine adjustment of the cavity length. The incident laser beam is coupled to the cavity using an aspheric lens (asph1: NA =0.5), which is mounted on a third PES (pes3: ANPx51) to adjust the focus of the incoming beam. A second aspheric lens (asph2: NA =0.2) is mounted at the transmission side of the fiber to collimate the transmitted light from the fiber. Figure 3.13 b displays a computer-aided design (CAD) drawing of the cavity assembly on the cryostat insert. Figure 3.13 c shows a side-view photograph through the window of the cryostat when the insert is positioned on the base plate and cooled to 4.2 K.

## 3.5.4 Polarization-mode splitting and cross-polarized detection

When a thin anthracene crystal is placed in the cavity, its birefringence lifts the polarization degeneracy of the cavity modes. Each of the eigenmodes splits into two modes resonant at different frequencies and of orthogonal polarizations aligned along the principle axes of the crystal. The vapor-phase growth of anthracene results in thin crystals lying on their **a-b** plane, which lies parallel to the planar mirror and perpendicular to the optical axis of the cavity.

The orientation of the **a** and **b** axes can be determined by rotating the polarization of the incoming laser beam and monitoring the coupling efficiencies to the two modes. The blue (brown) dots in Fig. 3.14 display the measured coupling efficiencies into the mode polarized along the **b** (**a**) axis of the crystal versus the incident polarization. The solid curves represent sinusoidal fits to the measured data which let us determine the orientations marked by the blue (**b**-axis) and brown (**a**-axis) lines. The angular separation of the two axes is 93° projected on our plane of measurement. In addition, we can determine the dipole orientation of DBT molecules by measuring the polarization of their fluorescence emission. The red dots in the same plot display the fluorescence intensity from a DBT molecule versus the angle of a polarizer in the detection beam path. The dipole orientation is extracted using a sinusoidal fit (red curve), which is tilted by 26° with respect to the **b**-axis.

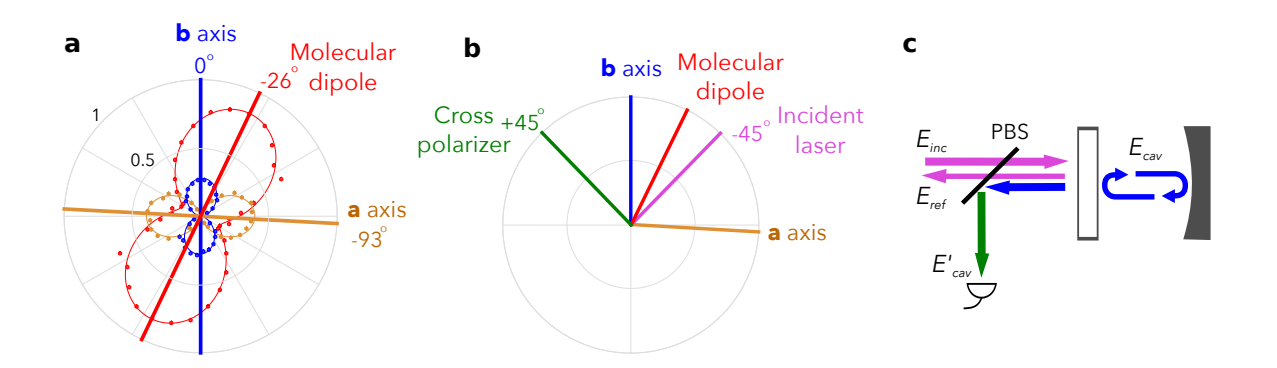


**Figure 3.14: a**, Orientation of the **a**, **b** axes of the crystal and the transition dipole of a DBT molecule. The blue (brown) dots represent the measured coupling efficiencies into the **b**- (**a**-) polarized modes. The red dots denote the measured fluorescence intensity (in arbitrary units) of a DBT molecule. The solid curves represent sinusoidal fits to the measured data. The solid lines display the orientations extracted from the fits. **b**, Arrangement of the incident and detection polarization for the cross-polarized detection. **c**, Schematic of the cross-polarized detection scheme. See text for details.

**58** 3.6. Vibration control

The polarization anisotropy allows us to access the intracavity field at the reflection side exclusively. As illustrated in Fig. 3.14 b and c, we set the polarization of the incident laser beam at  $-45^{\circ}$  with respect to the b-axis and place a polarizer at  $+45^{\circ}$  in the reflection beam path. A part of the incident beam  $(E_{\rm inc}, \, {\rm pink})$  is coupled to the intracavity field  $(E_{\rm cav}, \, {\rm blue})$ . The transmission of the intracavity field through the incoupling mirror is separated from the reflected field  $(E_{\rm ref}, \, {\rm pink})$  at the cross polarizer (PBS). The reflected light at the PBS  $(E'_{\rm cav}, \, {\rm green})$  detected against a very low background provides the means for monitoring the intracavity field, equivalent to measuring the transmission field.

We note that the coated optical elements (such as mirrors, beamsplitters and cryostat window plates) in the setup introduce rotations to the polarization of the incident laser beam. Therefore, a HWP and a QWP are placed after the out-coupler of the laser (see Fig. 3.11) to pre-compensate the polarization rotations in the setup. However, the depolarization effects, e.g. due to the inhomogeneity of the window plates under thermal stress or the focusing and re-collimation from the cavity can not be compensated by the waveplates. This results in a finite extinction ratio of the reflected light. In the experiment, we normally achieve an extinction ratio of about 300:1, translating to a signal-to-background ratio of 15:1 when measuring the transmission of an empty cavity under cross-polarization.

## 3.6 Vibration control

The main challenge in operating a tunable microcavity in a helium cryostat lies in the stability of the system. For example, a cavity with a finesse of 15,000 has a linewidth of about 26 pm. Although macroscopic optical cavities could be stabilized down to the level of femtometers [99], adopting the conventional techniques to a tunable microcavity in the complex cryogenic environment remains a challenging task. In this section, we explain the passive and active noise isolation measures implemented in our experiment in order to reach a cavity length stability of about 20 pm.

When placed in the cryostat, the cavity is affected by two main sources of noise. First, the acoustic noise in the laboratory (e.g. from the ventilation system and the electronic instruments) can couple to the cavity via the acoustic conduction of the sample rod and the exchange gas. Second, the operation of the cryostat is accompanied by mechanical vibrations from various sources, such as the vacuum pumps, the boiling of the cryogenic liquids and the icing at the exhausts of the helium tanks.

We implement noise-isolation measures for each specific source of noise. First, two layers of 10 cm-thick foam (BPlanG100SK, Firma flexolan e.K.) with acoustic attenuation of 1.3 dB/cm (at 200 Hz) are constructed around the cryostat to shield it against the acoustic noise from the laboratory environment. Second, acoustic conduction via the sample rod is negated by mechanically detaching the microcavity assembly from the sample rod once it is positioned on the base plate. Third, the pressure in the sample chamber is reduced to  $10^{-2}$  mbar during the measurements to minimize the acoustic conduction via the exchange gas. Fourth, massive concrete dampers are added to both the turbo pump and the diaphragm pump to reduce their mechanical conduction to the cryostat. Lastly, the filling schedule of the cryostat is carefully planned that the measurements are only performed shortly after all the liquid nitrogen has evaporated and the liquid helium tanks are about 50% filled. In this time interval, the vibration within the cryostat is significantly reduced and the liquid nitrogen tank remains at a low temperature (<100 K). When the liquid nitrogen tank warms up further, thermal tensions start to develop between different parts of the cryostats and sudden jumps of the cavity length are frequently observed.

In addition to the measures for noise isolation, a feedback loop is implemented to actively stabilize the cavity length using the Hänsch-Couillaud scheme [98]. The method is applicable to optical resonators with polarization anisotropy, which is provided by the birefringence of anthracene in our cavity.

When measuring with DBT molecules in a Ac crystal, the cavity length should be kept stable at the 00ZPL frequency of the molecules ( $\sim 784 \,\mathrm{nm}$ ) and support the mode polarized aligned along the b-axis. At the same cavity length, a second mode at around 762 nm is simultaneously resonant with its polarization aligned to the a-axis. A tunable diode laser (locking laser) at 762 nm is used to obtain an error signal for the active stablization (see also Fig. 3.11). The polarization of the locking laser is aligned at +45° with respect to the a-axis. Upon reflection from the cavity, the polarization component parallel to the a-axis couples to the cavity and experiences a cavity-length dependent phase delay. The component perpendicular to the a-axis is reflected at the planar mirror and serves as a constant phase reference [98]. The changes in cavity length are thus translated to the ellipticity of the reflected beam. On the detection path, the ellipticity is analyzed using a QWP at  $+45^{\circ}$  and a PBS. The intensities of the two outputs of the PBS are measured by the two channels of a balanced photodetector. The output of the detector provides an error signal, which is positive when the cavity is too long and negative when it is too short. The error signal is first inverted and amplified by a low-noise preamplifier (SR560, Stanford Research Systems) and then fed to a PID module (PID110, Toptica Photonics AG). The output of the PID is **60** 3.6. Vibration control

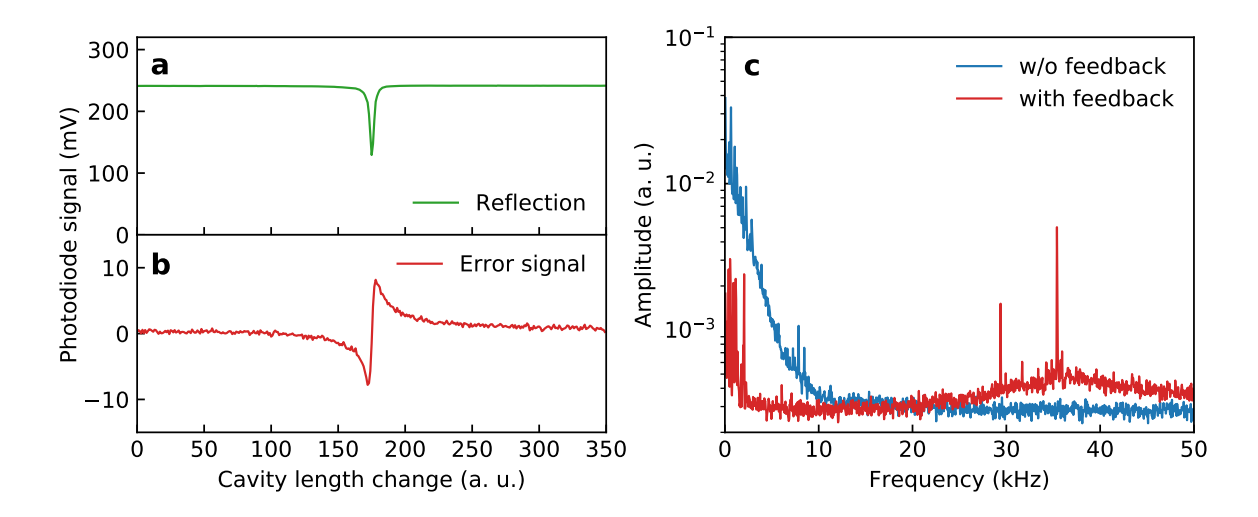


**Figure 3.15:** a, Reflected signal from the cavity as a function of cavity length change. b, Output of the balanced photodetector, providing a error signal for the feedback stabilization. c, Fourier spectra of the vibrations for the locked (red) and unlocked (blue) cavity.

sent to a high-voltage amplifier which drives the piezoelectric transducer holding the micromirror and thus compensates for the changes in cavity length.

Figures 3.15 a, b display an example of the measured reflection and error signals from the cavity as a function of the cavity length change, respectively. The measurement was performed on the low-finesse cavity at  $4.2\,\mathrm{K}$ . The error signal is in a dispersive lineshape and has its zero-crossing at the resonant length. The blue line in Fig. 3.15 c represents the Fourier amplitude of the error signal of the passively stabilized cavity, obtained by the Fourier transformation of the error signal. The red line in the same figure stands for the same quantity but with the feedback loop activated. The active feedback reduces the vibration amplitude by about one order of magnitude in the low frequency range ( $<20\,\mathrm{kHz}$ ). The fast feedback regulation is also evidenced by the small vibrations introduced in the frequency interval (20, 50) kHz. This allows us to determine the bandwidth of the feedback loop to be 20 kHz. In this example, the RMS amplitudes of the vibrations for the passively and actively stablized cavity shown in this plot are 0.6 nm and 0.1 nm, respectively.

# Chapter 4

# A classical dipole in a microcavity

The content of the chapter has been published in Sensing nanoparticles with a cantilever-based scannable optical cavity of low finesse and sub- $\lambda^3$  volume by H. Kelkar, D. Wang, D.-M. Cano, B. Hoffmann, S. Christiansen, S. Götzinger and V. Sandoghdar, Phys. Rev. Applied 4, 054010 (2015).

Some passages of the present text are similar to the text in the published manuscript.

In this chapter, we report on the experimental realization of an open and tunable Fabry-Pérot cavity (FPC) with a mode volume smaller than  $\lambda^3$ . The microcavity is assembled on the room-temperature microscope, consisting of a planar mirror and micromirror with a radius of curvature of 2.6  $\mu$ m, fabricated on a silicon cantilever. The microcavity features a low quality factor in the order of 200. Spectral measurements show that the cavity can support a resonance with longitudinal mode number q=2. In contrast to macroscopic FPCs, we observe a clear dependence of the cavity's finesse and quality factor on the longitudinal mode number. We perform full numerical simulations to extract the mode volumes of various longitudinal modes, arriving at a volume as small as  $0.8\lambda^3$  for the q=2 mode.

The open character, scanning capability and small mode volume of the microcavity facilitate its usage as a scanning microscope [77,88]. We demonstrate spatially resolved sensing of single 80-nm gold nanoparticles using the microcavity, where the introduction of a nanoparticle shifts the cavity's resonance frequency by up to 400 GHz. The polarizability of the nanoparticle is comparable to a virus with a diameter of 200 nm immersed in water. The sensing capability thus makes the microcavity attractive for applications in biological or chemical sensing [87,100].

#### 4.1 Characterization of the cavity parameters

The measurements are performed on the inverted-microscope setup at room temperature. The optical setup and the assembly of the microcavity are introduced in chapter 3. In brief, we use a micromirror fabricated on an n-doped silicon cantilever that contains a pedestal with a diameter of  $8 \mu m$ . The mirror is machined on the end of the pedestal using focused-ion-beam milling with a radius of curvature of  $2.6 \mu m$ . After the machining, the mirror is coated with gold (see section 3.3.2), yielding a nominal reflectivity of 96% at  $\lambda = 785$  nm. Taking into account the slight roughness of this mirror (root mean square value of 3.6 nm, see Fig. 3.6 a), we expect the reflectivity to be reduced to  $\sim 95\%$  due to residual scattering [101].

The planar mirror of the cavity is a fused silica substrate coated with a dielectric coating, which consists of 11 bilayers of  $\text{TiO}_2/\text{SiO}_2$  finished by a 22-nm layer of  $\text{TiO}_2$  to place the field maximum at the mirror surface. The coating has a total thickness of 2.14  $\mu$ m with a design center wavelength at 710 nm and a band edge at 841 nm, leading to reflectivities of 99.9% at  $\lambda = 785\,\text{nm}$  and 99.99% at 745 nm. The microcavity is assembled with piezoelectric transducer (PZT) stacks for the positioning of the cantilever and a PZT scanner for the lateral displacement of the planar mirror. The light is coupled into the cavity using an objective with a numerical aperture of 0.75. The light reflected from the cavity is collected by the same objective and detected by a photodiode (see Fig. 3.9).

#### 4.1.1 Spectra of the cavity

We first measure and characterize the spectra of the cavity. The light from a diode laser (DL Pro, Toptica Photonics AG) is coupled into the cavity mode using the microscope objective. The length of the cavity is scanned by actuating the PZT holding the cantilever and the light reflected from the cavity is measured using a photodiode. We perform the measurements at two wavelengths,  $\lambda$ =785 nm and  $\lambda$ =745 nm. The blue spectra in Figs. 4.1 a and b display the measured reflection signal from the cavity as a function of cavity length L at wavelengths of 745 nm and 785 nm, respectively. Here, the incident light is slightly defocused and misaligned to allow coupling to the higher-order transverse modes. The vertical red lines mark the resonances associated with the Hermite-Gaussian modes predicted by the equation

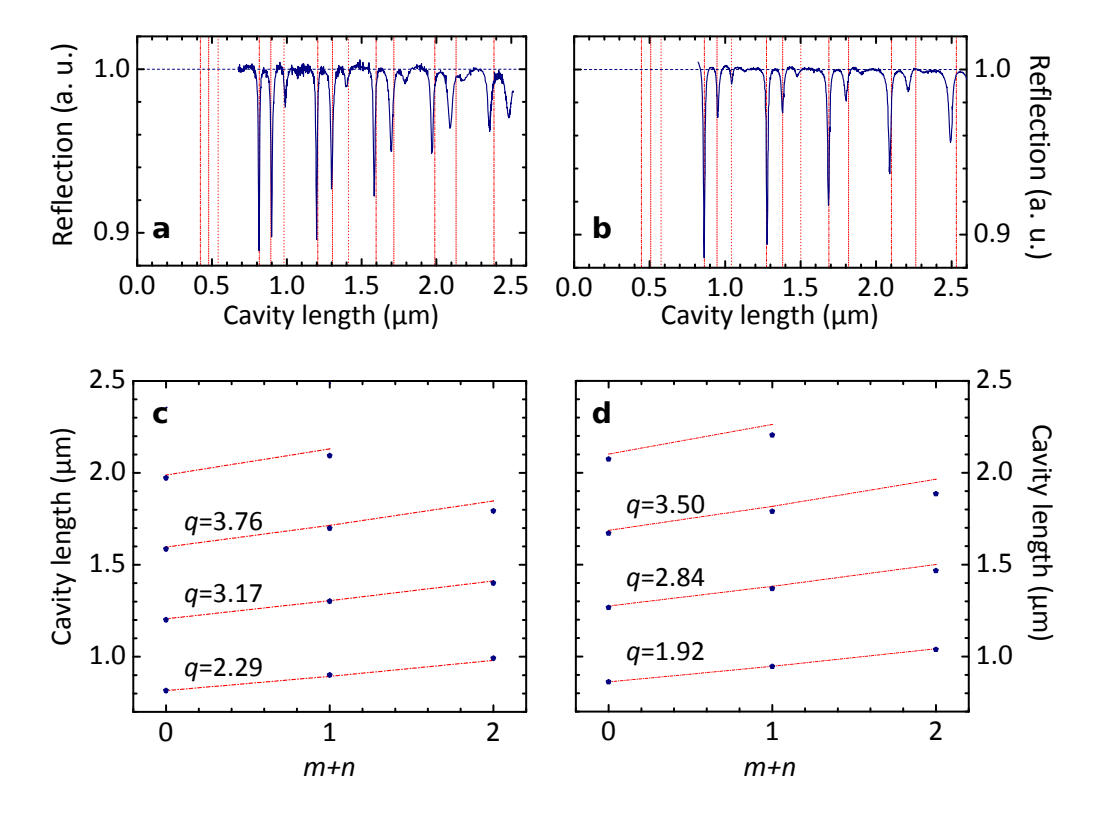


**Figure 4.1: a, b**, Intensity of the reflected light from the cavity as a function of the cavity length for wavelengths 745 nm and 785 nm, respectively. The focus and the lateral alignment of the incident beam are adjusted to allow coupling to the higher-order transverse modes. The red vertical lines denote the resonances of the cavity according to a Hermite-Gaussian model. **c, d**, Summary of the experimental (blue dots) and theoretical data (red lines) from **a, b** plotted as a function of m+n for various TEM<sub>mn</sub> modes. The indices q signify the best fit obtained for the longitudinal mode number.

$$L = \frac{\lambda}{2} \left[ q + \frac{m+n+1}{\pi} \arccos\left(\sqrt{1-\frac{L}{R}}\right) \right], \tag{4.1}$$

for a cavity with the same nominal geometrical parameters as in the experiment but considering ideal thin mirrors [102]. The second term in the square brackets denotes the Gouy phase within the paraxial approximation. The blue dots in Figs. 4.1 c and d summarize the dependence of L on m+n indices of the transverse TEM<sub>mn</sub> modes, corresponding to the spectra presented in Figs. 4.1 a and b, respectively. After fitting the data using Eq. 4.1, we obtain values for q given in the legends of Figs. 4.1 c, d. The close cumulative agreement between theory and experiment suggests that we have reached the longitudinal mode with q=2. The resulting non-integer values of q stem from the fact that Eq. 4.1 neglects the penetration of the field into the dielectric

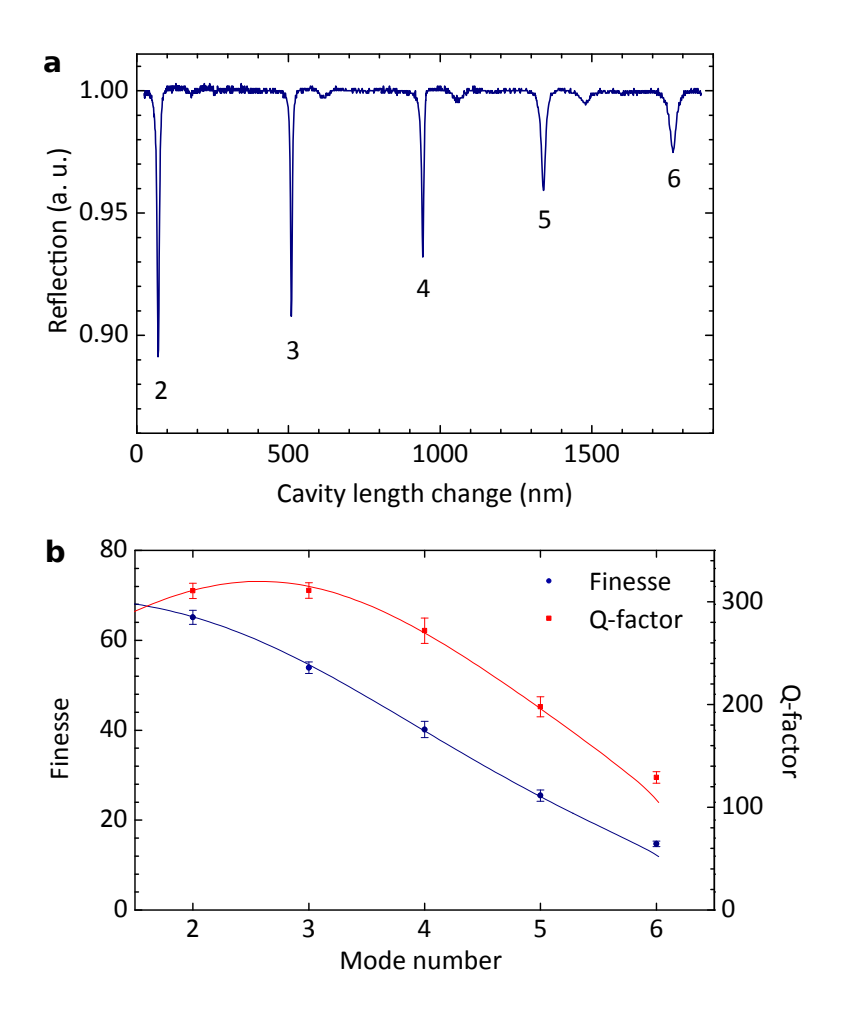


**Figure 4.2: a**, Intensity of the reflected light as a function of the cavity length change. The longitudinal mode number is labeled below each corresponding resonance. The small satellite resonances result from coupling to higher order transverse modes. **b**, Q-factor (red) and finesse (blue) of the cavity versus mode number q. The dots represent the experimental data. The solid curves show the theoretical predictions.

mirror [69]. A thorough examination of the cavity resonance conditions and the phase responses of the mirrors to explain the non-integer values of q is presented in Ref. [79].

In Fig. 4.2 a, we plot a spectrum recorded at  $\lambda = 785 \,\mathrm{nm}$ , where the incident beam is aligned to minimize the coupling to higher transverse modes. The finesse  $\mathcal{F}$  and quality factor  $Q = q_{\mathrm{eff}} \cdot \mathcal{F}$  extracted from this spectrum are displayed by the dots in Fig. 4.2 b. Here,  $q_{\mathrm{eff}}$  is an effective mode number accounting for the penetration and phase shift of the mirrors [79]. In contrast to macroscopic FPCs,  $\mathcal{F}$  and Q vary strongly with the mode number.

To understand our observations, we set up a simple model based on the propagation of a Gaussian beam between the two mirrors. The position and size of the beam waist

after each round trip are calculated, whereby the loss due to the finite aperture of the curved mirror (about 0.1% per round trip for the longitudinal mode with q=2) is treated simply as a scalar factor. The red curve in Fig. 4.2 **b** represents the quality factor calculated using the intracavity intensity decay time, which is in good agreement with the experimental values. We notice deviations for the highest mode order, where the cavity length L is large enough that the diffraction at mirror edges and losses due to beam clipping become significant and our model is no longer strictly valid. The nonmonotonous behavior of Q in Fig. 4.2 **b** is the result of the competition between finite-aperture losses and the gain in the photon lifetime for larger cavity lengths. The blue curve in Fig. 4.2 **b** displays the calculated  $\mathcal{F}$ , which is in good agreement with the experimental values determined by taking the ratio of the mode spacing  $L_{q+1} - L_q$  to the linewidth  $\delta L$ .

#### 4.1.2 Mode volume

The mode volume V of a cavity plays a central role in the context of cavity quantum electrodynamics [27,28]. V is usually calculated as the integral of the electromagnetic energy density in the physical volume of the cavity normalized to the maximum of the field intensity (see chapter 2). For macroscopic FPCs, the mode volume can be estimated using the expression  $V = \pi w_0^2 L/4$  [103], where  $w_0$  is the Gaussian mode waist. In the presence of a dielectric mirror, the field penetration into the multilayered dielectrics makes the calculation nontrivial, especially when L becomes comparable to  $\lambda$  and to the penetration depth [69, 104]. In order to obtain accurate estimations of the mode volume, we perform full-numerical simulations using COMSOL Multiphysics. Figure 4.3 a-c display the cross sections of the intensity distribution for three longtudinal modes with q = 2, 3, 4 at  $\lambda = 745 \,\mathrm{nm}$ .

To calculate the mode volume of the eigenmodes, we follow the definition provided in Ref. [48], which allows for the treatment of the Purcell factor in complex electromagnetic geometries. We find that the q=2 mode has a mode volume as small as  $0.8\lambda^3$ . For longer cavity lengths, V grows approximately linearly with q. Such a small mode volume can support notable Purcell enhancement of an emitter, even though the cavity only has Q in the order of 200. Figure 4.3  $\mathbf{d}$  displays the calculated mode volume and expected Purcell factor versus the mode number q for  $\lambda = 745$  nm.

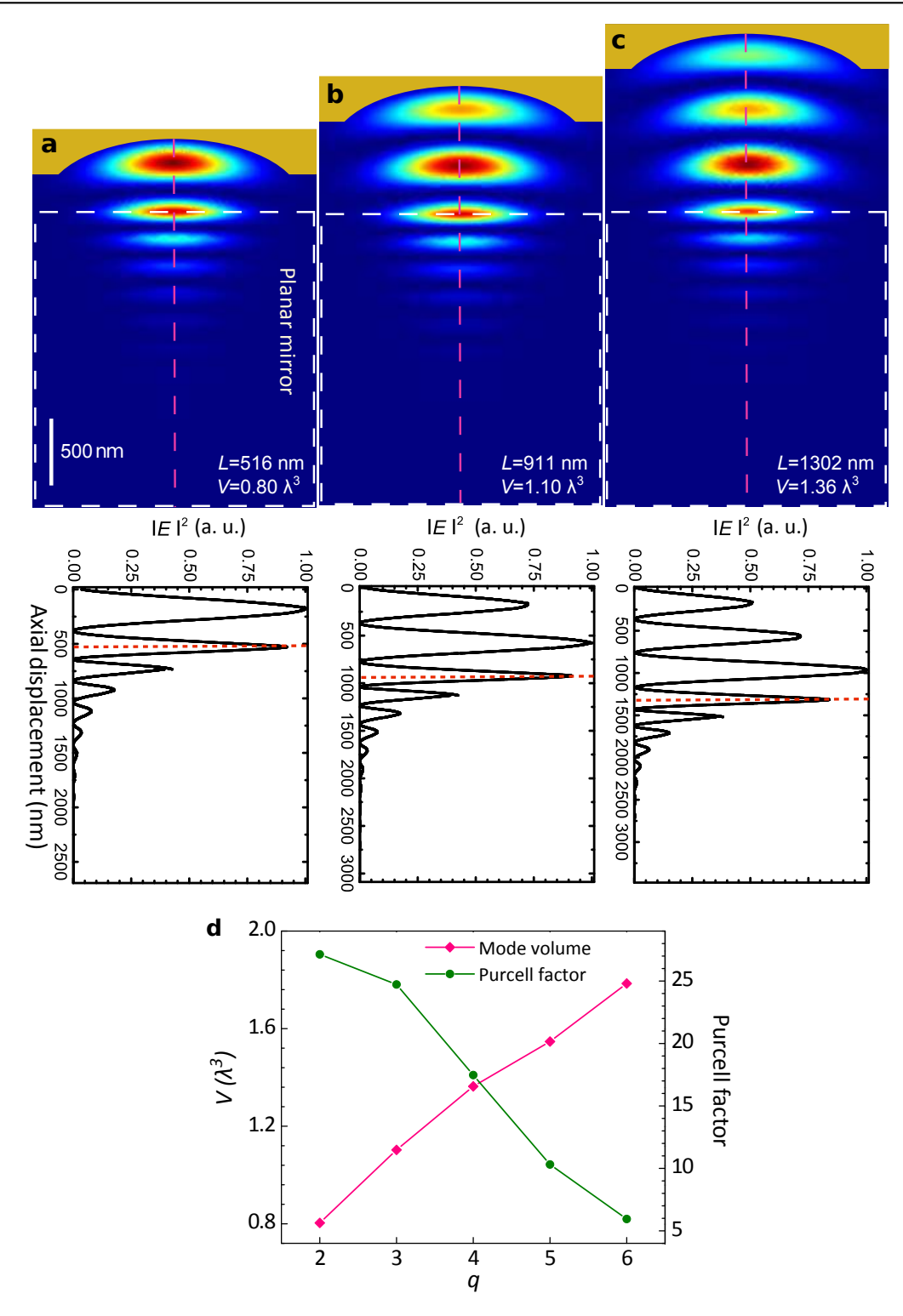


Figure 4.3: a, b, c, Intensity distribution obtained from the numerical simulations for three longitudinal modes with q=2,3,4 at a wavelength of 745 nm. The dashed white lines in the upper figures mark the boundaries of the dielectric mirror. A cross sectional intensity distribution along the vertical dashed red line is displayed at the bottom of each subplot. The horizontal dashed red lines mark the boundaries between air and the planar mirror. The mode volume V and the cavity length L measured between this interface and the apex of the curved mirror is displayed in each plot. d, V (magenta) and the expected Purcell factor F (green) versus the longitudinal mode number q extracted from the numerical simulations.

#### 4.2 Sensing and imaging of single nanoparticles

The introduction of a foreign object into an optical resonator modifies the round-trip optical path length, thus leading to a spectral shift of the cavity resonance. This effect has been utilized for tuning the resonance frequency of laser cavities [102]. Vice versa, the spectral shift of a cavity can be monitored to detect the presence of small objects such as nanoparticles, viruses or even single molecules [100, 105, 106].

#### 4.2.1 Frequency shift by a single dipolar scatterer

When a subwavelength nanoparticle is placed in the cavity mode, its Rayleigh scattering introduces a phase shift [107] to the cavity field and thus leads to a shift of the cavity resonance. The amount of spectral shift  $\Delta\nu$  introduced by a nanoparticle with complex polarizability  $\alpha$  can be written as

$$\frac{\Delta\nu(\mathbf{r})}{\nu} = -\frac{\mathcal{R}e(\alpha)}{2V} \frac{|E(\mathbf{r})|^2}{\max[|E(\mathbf{r})|^2]},$$
(4.2)

where  $\nu$  is the resonance frequency of the unperturbed cavity,  $E(\mathbf{r})$  is the electric field at position  $\mathbf{r}$  in the cavity [105, 108]. In the quasi-static approximation

$$\alpha = \frac{\pi D^3}{2} \frac{\epsilon_{\rm p}(\lambda) - \epsilon_{\rm m}(\lambda)}{\epsilon_{\rm p}(\lambda) + 2\epsilon_{\rm m}(\lambda)}, \qquad (4.3)$$

where D is the diameter of the particle,  $\epsilon_{\rm p}(\lambda)$  and  $\epsilon_{\rm m}(\lambda)$  are the dielectric functions of the particle and its surrounding medium, respectively. When the particle is placed at the field maximum of the cavity, Eq. 4.2 can be simplified to

$$\frac{\Delta\nu}{\kappa} = -\frac{\alpha}{2} \frac{Q}{V} \,, \tag{4.4}$$

which expresses the ratio of a frequency shift  $\Delta \nu$  to the linewidth  $\kappa$  of the cavity resonance. It is apparent that a high Q and a small V facilitate the detection of a small frequency shift.

To investigate the effect of a nano-scatterer on our cavity, we spin coat gold nanoparticles (GNP) of diameter 80 nm on the planar mirror with inter-particle spacings in the order of a few micrometers. To ensure that we can address individual GNPs, we perform AFM measurements on the planar mirror to identify particles that are far enough from their neighbors. By correlating the AFM image and the optical scattering

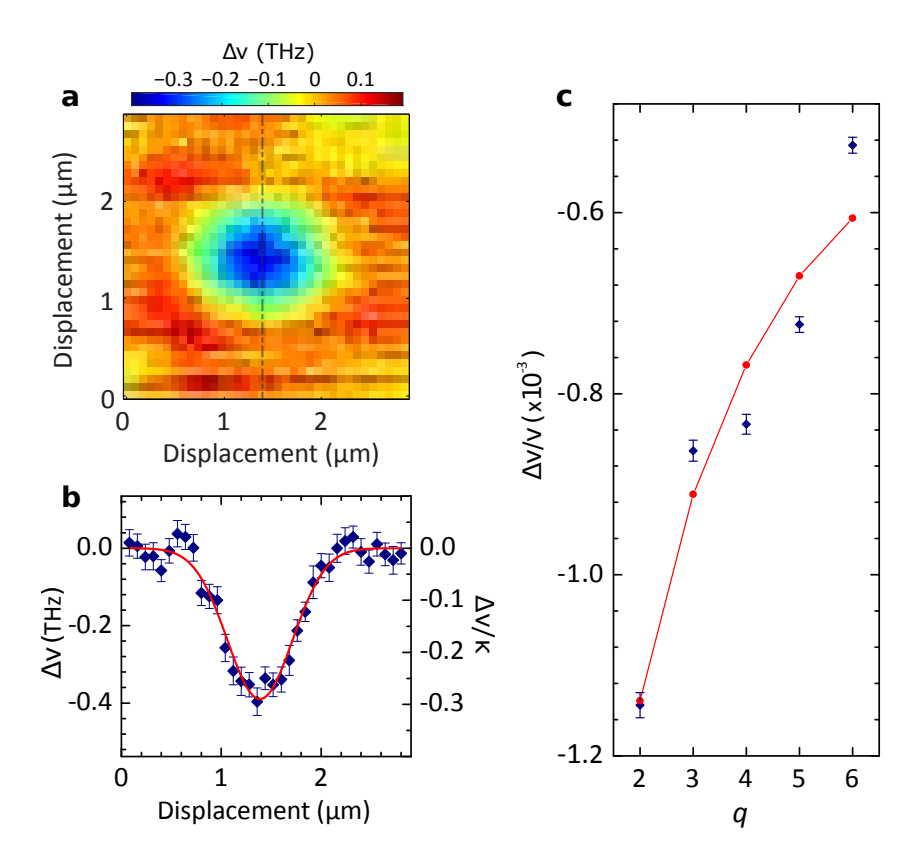


**Figure 4.4: a**, Shift of the q=2 cavity resonance in THz as a function of the lateral displacement of a gold nanoparticle. **b**, A cross section of **a** along the vertical dash-dotted line. The red line displays a fit to a Gaussian function. **c**, Cavity resonance shift measured for different longitudinal modes. See text for details.

image acquired by the inverted microscope, we can then map the positions of individual GNPs.

Figure 4.4 a displays the measured cavity resonance shift as a function of the lateral position of a single GNP and Fig. 4.4 b shows a cross section of it. The particle introduces a red shift of the cavity resonance of up to 400 GHz, equivalent to 40% of the cavity linewidth. The red line in Fig. 4.4 b displays a fit to a Gaussian function, yielding a FWHM of 770 nm. To obtain these data, the planar mirror holding the GNP is scanned laterally, while the cavity length is scanned at each pixel.

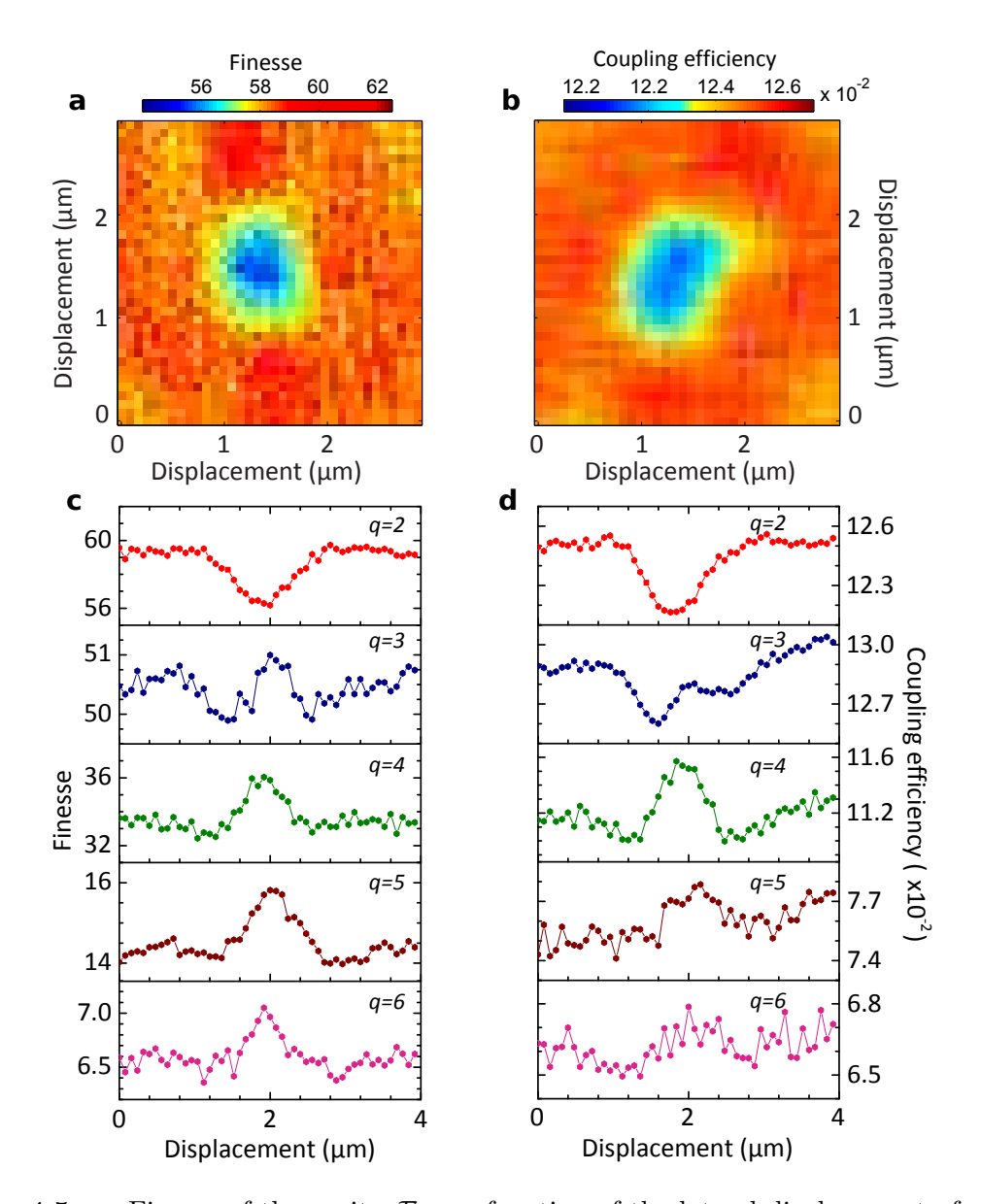
The blue dots in Fig. 4.4 c display the maximal cavity resonance shifts for different longitudinal modes. The error bars represent the uncertainties in extracting the spectral shifts from Gaussian fittings (see Figure 4.4 b). As expected from Eq. 4.2, the effect of the particle rapidly diminishes for higher q modes with larger mode volumes. To verify the measured data quantitatively, we perform a fit using Eq. 4.2, while leaving  $\alpha$  as a free parameter. The red curve displays the best fit obtained for  $\alpha = 1.1 \times 10^6$  nm<sup>3</sup>, which is 1.17 times larger than its expected value for a GNP with a diameter of  $80 \pm 6$  nm.

However, one should keep in mind that calculating the exact value of  $\alpha$  for a given GNP is difficult. First, near-field coupling to the surface of the planar mirror modifies the plasmon resonance and hence the polarizability [109]. By using an analytical expression [110], we estimate the polarizability of the GNP to be 1.1 times larger in the presence of the end layer of the planar mirror compared to the value when it is in vacuum. Furthermore, the radiation damping effect resulting from the finite size of the particle [111] and the coupling of the scattering fields via the radiation continuum [112] enter beyond the simple expression of Eq. 4.2 and 4.3. Considering these effects, our experimental findings are in very good agreement with the theoretical expectations.

#### 4.2.2 Modifications of finesse

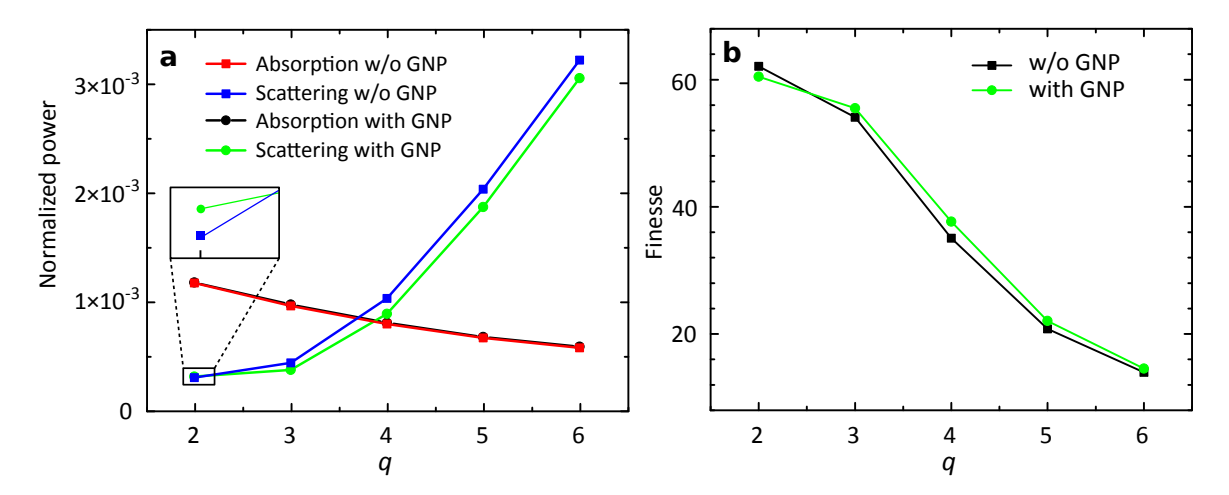
Having studied the spectral shift introduced by the nanoparticle, we now analyze its effect on the cavity's finesse  $\mathcal{F}$ . One might intuitively expect that a foreign object would introduce scattering and absorption losses to the cavity, thus reducing its  $\mathcal{F}$ . Although this is true in most cases, it has been demonstrated that a nano-object can shift the cavity resonance without incurring a notable broadening [105, 108], or even induce line narrowing [112].

Figure 4.5 a displays a map of  $\mathcal{F}$  as a function of the lateral displacement of the GNP in the q=2 mode. The coupling efficiency into the cavity mode extracted from the same measurement is shown in Fig. 4.5 b. Figures 4.5 c (d) display cross sections of the measured finesse (coupling efficiency) for modes of different mode numbers. At shorter cavity lengths, the micromirror supports a large enough solid angle that the light scattered by the nanoparticle can be efficiently captured after each round trip. In this regime, the absorption of the particle determines the change in the finesse. For example, one finds that the presence of the particle reduces  $\mathcal{F}$  by about 7% for the q=2 mode. However, this behavior changes substantially for the modes at longer cavity lengths, as shown by the other subplots (q > 2) in Fig. 4.5 c. When L approaches R, the unperturbed cavity resonance becomes less stable, as witnessed by the reduction in  $\mathcal{F}$  (see also Fig. 4.2 b). In this regime, we find that addition of a GNP increases the finesse, e.g. for the mode with q=6, the finesse is increased from 6.5 to 7. The same behavior is also observed in the coupling efficiencies to the cavity mode. As shown by Figs. 4.5 d, for the modes with q > 3, the presence of the nanoparticle improves the incoupling efficiency to the microcavity, implying that the nanoparticle reduces the overall losses in the cavity.



**Figure 4.5: a**, Finesse of the cavity  $\mathcal{F}$  as a function of the lateral displacement of a single GNP for the q=2 mode. **b**, Coupling efficiencies to the cavity mode versus the lateral position of the GNP for the q=2 mode, obtained by normalizing the reflected power to the incident power. **c**, Cross sections of  $\mathcal{F}$  versus the displacement of GNP for different longitudinal modes. The mode number q is indicated in each plot. **d**, Cross sections of the coupling efficiencies to different modes of the cavity.

To examine the underlying effects of our observations, we perform numerical calculations including the nanoparticle in the cavity. We consider the contribution of absorption and scattering losses to the cavity quality factor (denoted as  $Q_{\rm abs}$  and  $Q_{\rm sca}$ , respectively) according to  $1/Q = 1/Q_{\rm abs} + 1/Q_{\rm sca}$ . The absorption and scattering powers are estimated from simulations by calculating the overall resistive losses per optical cycle and the power flow in the directions perpendicular to the cavity axis. Figure 4.6 a



**Figure 4.6:** a, Absorption and scattering losses normalized by the intra-cavity electromagnetic energy per optical cycle versus the mode number. The inset displays a close-up of the scattering loss for the q=2 mode, showing that the presence of the nanoparticle increases the scattering loss of the cavity. b, Finesse of the cavity obtained from the simulations with (green) and without (black) the nanoparticle.

displays these two terms for different modes normalized to the energy stored in the cavity every optical cycle. For an empty cavity without the nanoparticle, the absorption loss decreases while the scattering loss grows with q, as shown by the red and the blue lines. The introduction of a nanoparticle to the cavity (at the intensity maximum on the planar mirror) slightly increases the absorption (black line). The nanoparticle increases the scattering loss of the q=2 mode (see inset) but reduces it for modes with q>2 (green line). The reduction of the scattering losses can be explained by destructive interference of the radiation leakages of the cavity mode and the scattering of the GNP into free space [112].

The black dots in Fig. 4.6 **b** display the finesse obtained from the numerical simulations with and without the presence of a nanoparticle. To arrive at these values, we adjusted the reflectivity of the gold-coated micromirror to 94% to emulate the experimental values, corresponding to a reduction of the finesse by 2.4 times from its expected value for the ideal structure. The trend obtained from the numerical simulations shows excellent agreement with the measured values (see Fig. 4.2 **b**). In particular, we observe the cross-over of scattering losses with and without the nanoparticle between the q=2 and q=3 modes, as displayed in Fig. 4.6 **a**. The reduction of scattering losses caused by the nanoparticle increases the cavity finesse and thus verifies the experimental observations in Fig. 4.5.

# **Chapter 5**

# Efficient coherent light-matter interaction in a microcavity

The content of the chapter is part of the following manuscripts:

Coherent coupling of a single molecule to a scanning Fabry-Perot microcavity by D. Wang, H. Kelkar, D.-M. Cano, T. Utikal, S. Götzinger and V. Sandoghdar, Phys. Rev. X 7, 021014 (2017).

Turning a molecule into a coherent two-level quantum system by D. Wang, H. Kelkar, D.-M. Cano, D. Rattenbacher, A. Shkarin, T. Utikal, S. Götzinger and V. Sandoghdar, Nat. Phys. (2019), in press.

Some passages of the present text are similar to the text in the published manuscript.

In this chapter, we report on the experimental realization of efficient coherent coupling between light and an organic molecule, enabled by an open Fabry-Pérot microcavity operating at temperatures  $T \sim 3.0$ -4.2 K. In section 5.1, we first present the experimental observations of coupling a molecule to a low-finesse cavity mode. In the following sections, we report on the realization of a nearly-perfect coupling between a molecule and a high-finesse cavity mode. The efficient coupling gives rise to about 40-fold Purcell enhancement in the 00ZPL transition of a molecule, changing its branching ratio from 33% to 95% and thus converting the molecule to a nearly-perfect two-level system. The observed 99% extinction of the cavity's transmission and a phase shift of  $\pm 66^{\circ}$  of a laser beam provide evidence for the efficient and coherent interaction of the molecule with the incoming light field.

### 5.1 Coupling of a single molecule to a low-finesse cavity

In this section, we discuss the experimental observations in coupling a single molecule to a low-finesse microcavity. Details of the assembly of this cavity are discussed in chapter 3. The cavity is cooled down in a liquid-helium cryostat with an active feedback loop regulating its length using the Hänsh-Couilloud scheme [64, 98]. The measurements presented in this section were performed at temperatures  $T \sim 3.0$ -3.6 K, to avoid strong pumping on the liquid helium tank.

#### 5.1.1 Identifying a molecule

The cavity consists of a silver-coated micromirror with a radius of curvature (ROC) of  $5\,\mu\rm m$  and a planar mirror coated with dielectric multilayers (see section 3.5.3). The dielectric-coated planar mirror is designed to reflect the 00ZPL emission while transmitting part of the red-shifted fluorescence. Taking advantage of this design, we can identify molecules via fluorescence excitation spectroscopy. In the first step, we retract the micromirror from the planar mirror by approximately 2.5 mm and search for molecules through the planar mirror. Figure 5.1 a presents the fluorescence excitation spectrum of a confocal spot on the sample. The sharp peaks correspond to individual molecules within the inhomogeneous broadening of about 500 GHz. The low fluorescence intensity is due to the high reflectivity of the planar mirror at the excitation frequency, so that only a small fraction of the excitation light arrives at the molecules.

In the next step, the micromirror is moved towards the planar mirror to form a cavity. Figure 5.1 b presents the fluorescence excitation spectrum of the same confocal spot when the cavity is resonant at the lower frequency side of the inhomogeneous band. The increase in the signal amplitude provides evidence for the cavity enhancement of the excitation efficiency and the fluorescence collection. The broad Lorentzian-shaped envelope marked out by the dashed red line stems from the weak background fluorescence of the sample and reveals the linewidth of the cavity. To verify this, we tune the cavity resonance to a higher frequency by adjusting the frequency of the locking laser. Figure 5.1 c presents the modified fluorescence excitation spectrum, where the frequencies of individual molecules remain unchanged, while the envelope migrates to higher frequency by about 250 GHz. A quantitative analysis of the envelope allows us to determine the FWHM of the cavity resonance  $\kappa$  to be 250 GHz, corresponding to a quality factor of Q = 1500.

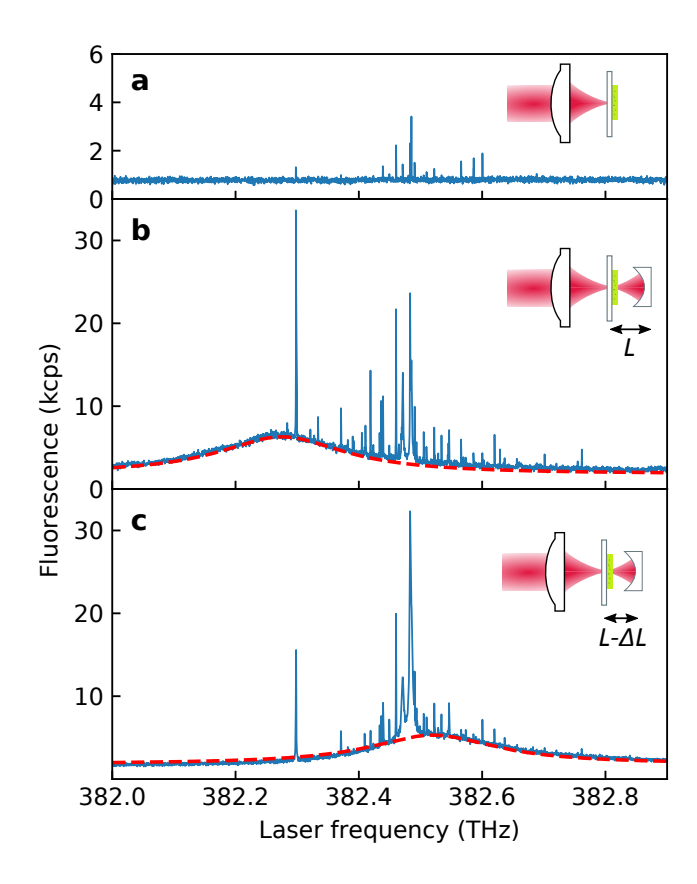


**Figure 5.1:** Fluorescence excitation spectra from one confocal spot on the sample. **a**, The micromirror is retracted. Single molecules show up as individual sharp resonances. **b**, **c**, The cavity resonance is stabilized at the lower and higher frequency sides of the inhomogeneous band, respectively. The dashed red lines in **b**, **c** represent a Lorentzian-profile with FWHM of 250 GHz. The unit of the vertical axis is kilocounts per second (kcps).

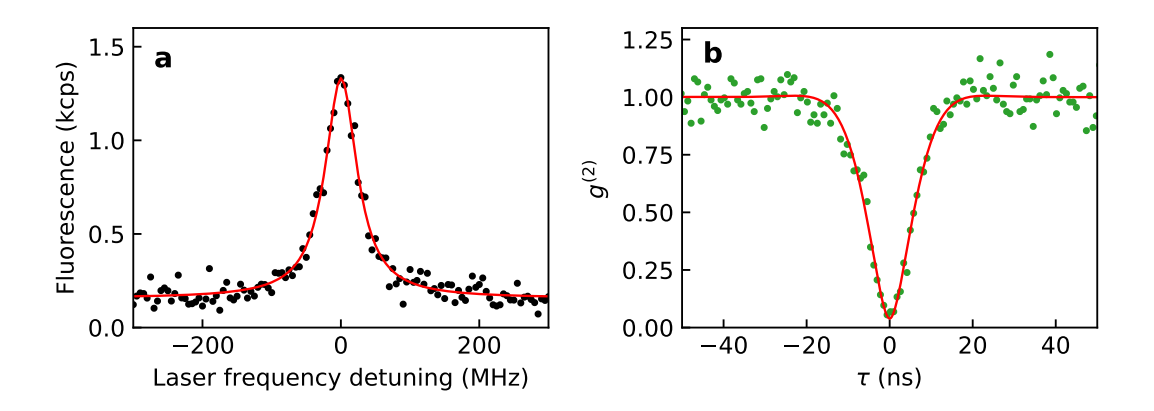


**Figure 5.2:** a, A close-up of one sharp resonance in the fluorescence excitation spectra. The red line represents a Lorentzian fit. b, Second-order intensity-correlation function measured at the peak of the resonance.  $\tau$  represents the time delay between the two detectors in the Hanbury Brown and Twiss setup. The red line displays a theoretical fit. The resulting  $g^{(2)}(0) = 0.04$  confirms that the signal is from a single molecule.

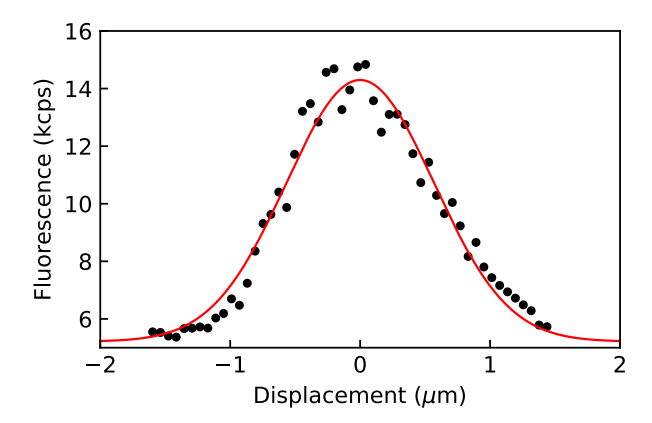


**Figure 5.3:** A lateral cross section of the cavity mode mapped by the fluorescence of a single molecule. The red curve displays a fit to a Gaussian function.

Having investigated the inhomogeneous broadening in the sample, we now turn to study the coupling of a single molecule to the cavity mode. Figure 5.2 **a** displays a frequency scan around one of the resonances in Fig. 5.1 **c**. The red line depicts a fit to a Lorentzian profile with a FWHM of  $56 \pm 2$  MHz. A second-order intensity correlation  $(g^{(2)})$  measurement at the peak of the resonance confirms that the signal is from a single molecule (see Fig. 5.1 **b**).

The open and scannable nature of the Fabry-Pérot cavity allows us to deterministically position a molecule at the lateral center of the cavity mode. The black dots in Fig. 5.3 display the fluorescence intensity of a molecule as it is scanned laterally across the cavity mode. The red line represents a fit to a Gaussian function with a FWHM of  $1.3\,\mu\text{m}$ . The Gaussian profile provides an estimation of the intensity cross section of the cavity mode at the planar mirror. Considering that the molecule might be saturated at the center of the spot, the width of the Gaussian profile gives an upper bound of the cavity mode diameter.

#### 5.1.2 Transmission spectra

Having identified a suitable molecule, we now study its coherent interaction with the cavity mode. The black dots in Fig. 5.4 a display the transmission of the cavity as a function of the frequency detuning of the excitation laser with respect to the molecule  $(\Delta\omega)$  measured via cross-polarized detection of the reflected light (see section 3.5.4). The red line shows a fit to a Lorentzian function. The FWHM of the fit profile is  $54 \pm 2 \,\mathrm{MHz}$ . The interference of the light scattered by the molecule and the cavity mode introduces a dip in transmission, equivalent to 38% of the transmission through

an empty cavity. The amplitude of the transmission dip provides a direct measure of the efficiency of the coherent interaction [51]. The green dots together with the dashed red line on the left of Fig. 5.4 a show the transmission signal when the laser frequency is detuned far out of the cavity resonance, defining a reference level for the measurement.

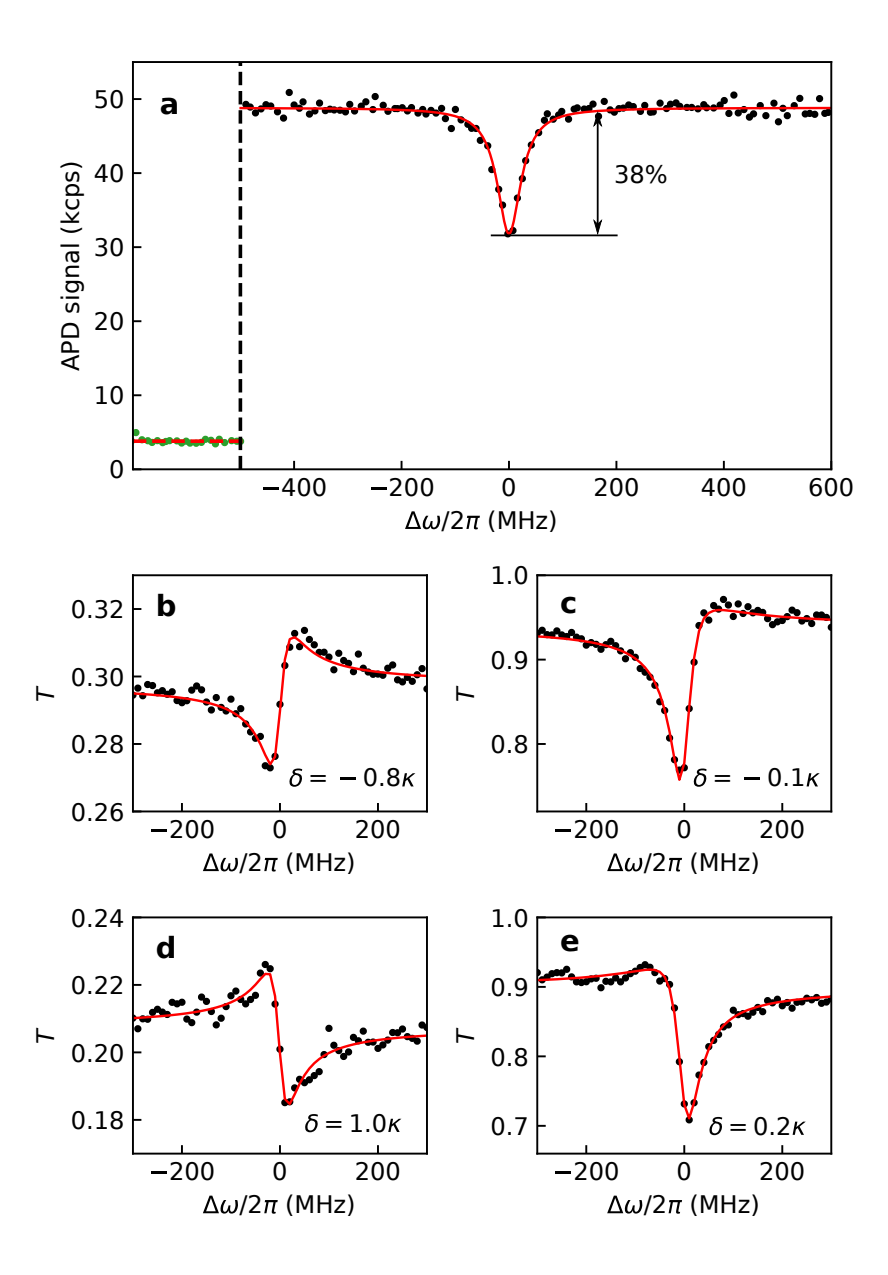


**Figure 5.4: a**, Black dots represent the measured transmission of the resonant cavity-molecule system as a function of the laser frequency detuning. The solid red line shows a Lorentzian fit. The green dots on the left side display the measured signal when the laser frequency is tuned far from the cavity resonance. **b-e**, Transmission spectra of the system for four different cavity frequency detunings by the amounts displayed in the corresponding legend. The solid red lines represent fits using a Fano-function.

We note that the cavity resonance is about 5000 times broader than the observed feature in Fig. 5.4 a. In this regime, the transmission profile in the vicinity of the molecular resonance can be approximated by a generalized Lorentzian function (see chapter 2 for details).

An important feature of the coherent interaction between two oscillators of different linewidths is a dispersive Fano lineshape [53]. As shown in Figs. 5.4 **b-e**, the Fano lineshape arises when the broader cavity resonance is detuned from the narrower molecular resonance. Figures 5.4 **b** and **d** present clear dispersive resonances when the cavity center frequency is detuned by  $\delta = -0.8\kappa$  and  $\delta = \kappa$  with respect to the molecule, respectively. As expected, the spectra approach an absorptive shape when the cavity is tuned closer to the molecular resonance (shown by Figs. 5.4 **c**, **e**).

#### 5.1.3 Cavity QED-parameters

To quantify the cavity modification of the molecular decay rates, we deduce the excited-state lifetime of the same molecule when resonantly coupled to the cavity ( $\tau' = 3.2 \pm 0.1 \,\mathrm{ns}$ ) and when the micromirror is retracted ( $\tau^0 = 3.9 \pm 0.1 \,\mathrm{ns}$ ) from second-order intensity correlation measurements [113], as displayed in Fig. 5.5. The resulting values of the lifetime match the measured linewidths of  $\gamma'/2\pi \approx 50 \,\mathrm{MHz}$  and  $\gamma^0/2\pi \approx 40 \,\mathrm{MHz}$ . Considering that the red-shifted transitions are spectrally broad and lie over the band edge of the planar mirror, we can assume the total decay rate into these channels is not affected by the cavity. The decay rates of the molecule without and with coupling to the cavity can be written as

$$\gamma^{0} = \gamma_{\text{red}} + \gamma_{\text{zpl}} ,$$
  

$$\gamma' = \gamma_{\text{red}} + (1 + F) \cdot \gamma_{\text{zpl}} ,$$
(5.1)

where  $\gamma_{\rm red}$  and  $\gamma_{\rm zpl}$  denote the decay rates of an uncoupled molecule into the redshifted fluorescence and into the 00ZPL, respectively. For DBT molecules embedded in anthracene crystals, the typical relation between the two decay rates is  $\gamma_{\rm red} \approx 2\gamma_{\rm zpl}$  [114]. F represents the Purcell factor describing the net enhancement of the 00ZPL transition into the cavity mode. The lifetime modification of the molecule can be expressed as

$$\frac{\tau'}{\tau^0} = \frac{\gamma_{\text{red}} + \gamma_{\text{zpl}}}{\gamma_{\text{red}} + (1+F) \cdot \gamma_{\text{zpl}}}.$$
 (5.2)

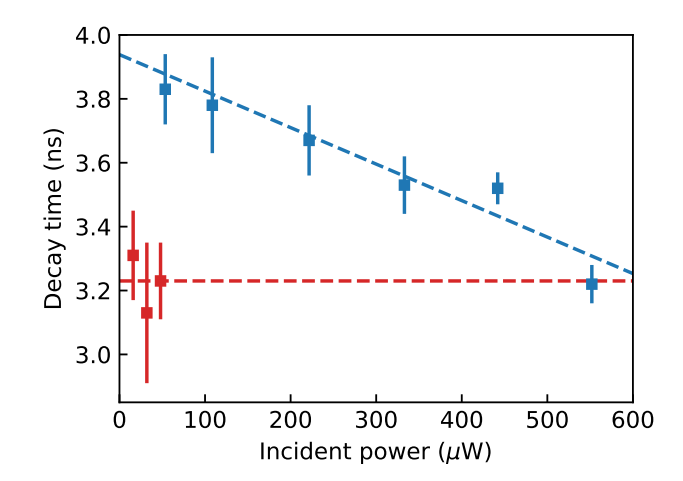


**Figure 5.5:** Modification of the excited-state lifetime. The red dots show the decay time of the measured  $g^{(2)}$ -signal at low pump powers in a resonant cavity. The blue dots display the same quantities recorded after retracting the micromirror at different incident powers. Extrapolation of a linear fit gives the lifetime in the limit of zero excitation intensity. The horizontal axis denote the incident power measured in front of the cryostat window.

Taking the measured values of  $\tau^0$  and  $\tau'$ , we arrive at F = 0.66. The cooperativity C, which quantifies the cooperative emission into the cavity mode, can be calculated as

$$C = \frac{F \cdot \gamma_{\text{zpl}}}{\gamma^0} \,, \tag{5.3}$$

which gives C = 0.22. The  $\beta$ -factor associated with the ZPL ( $\beta_{zpl}$ ) and the cavity-modified branching ratio  $\alpha'$  can be calculated using

$$\beta_{\text{zpl}} = \frac{F \cdot \gamma_{\text{zpl}}}{(F+1) \cdot \gamma_{\text{zpl}}} = \frac{F}{F+1} ,$$

$$\alpha' = \frac{(F+1) \cdot \gamma_{\text{zpl}}}{(F+1) \cdot \gamma_{\text{zpl}} + \gamma_{\text{red}}} \approx \frac{F+1}{F+3} ,$$
(5.4)

resulting in  $\beta_{\rm zpl} \approx 40\%$  and  $\alpha' \approx 45\%$ . The molecule-cavity coupling strength g can be calculated using the cooperativity factor,

$$g = \frac{\sqrt{C\kappa\gamma^0}}{2} \,, \tag{5.5}$$

where we find  $g/2\pi=740 \,\mathrm{MHz}$ .

In summary, the system operates in the weak coupling regime with  $(g, \kappa, \gamma^0)/2\pi = (0.74, 250, 0.04)$  GHz. The Purcell factor of the 00ZPL transition is 0.66 and the cooperativity of the molecular emission into the cavity mode 0.22.

# 5.2 A high-finesse microcavity in the cryogenic envi-

In the following sections of this chapter, we report on the experimental realization of a nearly-perfect light-molecule coupling enabled by a high-finesse microcavity. The fabrication and assembly of this cavity are discussed in chapter 3. In this section, we discuss the characterization of the cavity linewidth and the modeling of the residual vibrations. The measurements were performed at 4.2 K, without pumping on the liquid helium tank.

#### 5.2.1 Parameters of the cavity at 4.2 Kelvin

Once cooled down in the liquid-helium cryostat, the cavity is subject to noise from various sources, e.g. mechanical vibrations from the vacuum pumps, acoustic noise from boiling liquid helium and from the lab environment. As discussed in chapter 3, passive and active measures were implemented to isolate the experiment from the noise sources. For the high-finesse cavity presented in this section, the cavity length could be kept stable down to the order of one linewidth.

The black dots in Fig. 5.6 a, b display the measured transmission and reflection signals from the cavity as a function of the laser frequency detuning, respectively. A Lorentzian function is first used to fit the measured data, as displayed by the green lines. The clear deviations between the data and the fit curves indicate the effect of residual vibrations.

A Voigt-function of the form

$$f(\Delta\omega) = \frac{1}{1 + (2\Delta\omega/\kappa)^2} * \exp\left[-4\ln(2) \cdot (\Delta\omega/\sigma)^2\right], \qquad (5.6)$$

can be used to account for the vibrational broadening. The function is a convolution of a Lorentzian and a Gaussian function with FWHMs of  $\kappa$  and  $\sigma$ , respectively. The Lorentzian function represents the natural linewidth of the cavity resonance and the Gaussian function describes the effect of the vibrations. The fit of the two sets of data, shown by the red lines in Figs. 5.6 a, b allows us to deduce the width of the two components to be  $\sigma/2\pi = 2.29 \pm 0.10$  GHz and  $\kappa/2\pi = 1.66 \pm 0.11$  GHz. Note that to reduce the uncertainties of the two parameters, we have pre-determined the background levels of the transmission and reflection spectra (by far-detuning the cavity resonance) and fixed the center frequency of the cavity. Thus they did not enter as free parameters

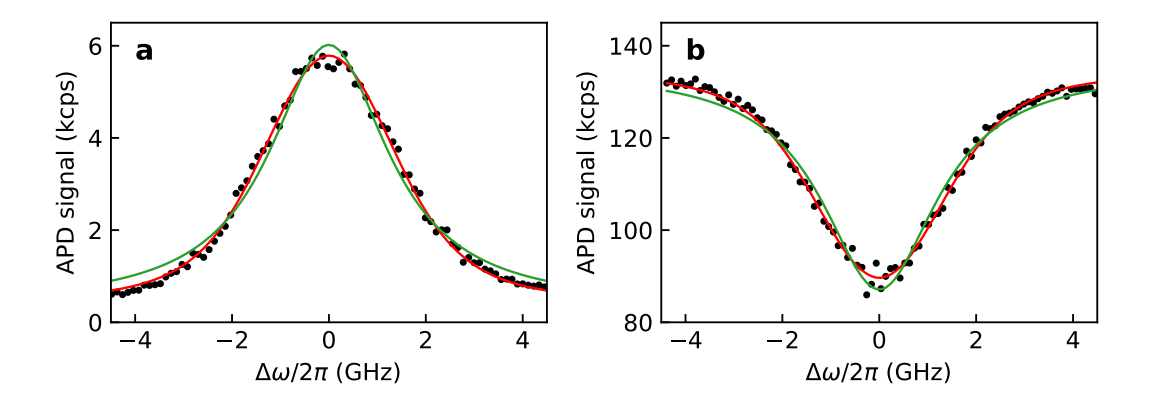


**Figure 5.6:** a, b, Measured transmission and reflection spectra of the cavity, respectively. The black dots represent the measured data. The red lines show fits to a Voigt function and green lines represent the fits to a Lorentizian function.

in the fitting. The FWHM of the Voigt profile  $\kappa'$  can be estimated using [115]

$$\kappa' \approx 0.535 \cdot \kappa + \sqrt{0.217 \cdot \kappa^2 + \sigma^2} \,, \tag{5.7}$$

to give  $\kappa'/2\pi \approx 3.32$  GHz.

Using the width of the Lorentzian component, we can calculate the intrinsic Q-factor of the cavity as  $Q = \omega_c/\kappa \approx 2.3 \times 10^5$ , where  $\omega_c/2\pi \approx 382880$  GHz denotes the center frequency of the cavity resonance. The apparent Q-factor (Q'), considering the vibration-broadening, is  $Q' = \omega_c/\kappa' \approx 1.2 \times 10^5$ .

The free spectral range (FSR) of the cavity is determined by scanning the laser frequency in a broader range, where two neighboring longitudinal modes at 784.1 nm and 853.5 nm are identified. The frequency spacing between the two modes of 31.09 THz corresponds to one FSR. We can then deduce the finesse of the cavity with  $\mathcal{F} = FSR/\kappa \approx 1.9 \times 10^4$ .

#### 5.2.2 Analyzing cavity vibration

To understand the origin of the residual vibrations, we measure the laser light reflected from the cavity using a fast photodiode. The laser is scanned slowly across the cavity resonance. The output of the photodiode is shown by the gray signal in Fig. 5.7 a. The signal oscillates as a result of the vibrations, when the laser frequency is tuned close to the cavity resonance. A time-average of the gray signal is displayed by the green curve, resembling the signal measured with an APD (as shown in Fig. 5.6 b, with integration

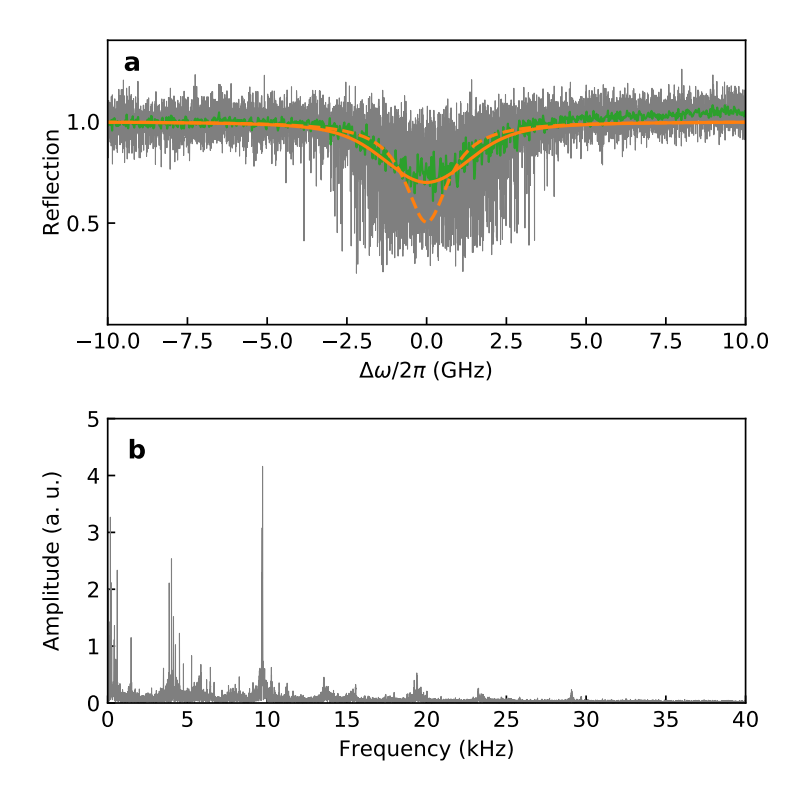


**Figure 5.7: a,** The signal in gray shows the reflection spectrum from the cavity measured with a fast photodiode. The green curve presents a time-average of the gray signal. The solid orange line represents a fit of the green to a Voigt function. The Lorentzian component of the Voigt fit is shown by the dashed orange line. **b,** Fourier spectrum of the vibrations, obtained by Fourier transforming the gray signal in **a**.

time of 50 ms per data point). The solid orange line represents a fit of the gray to a Voigt function, while the dashed orange line shows the Lorentzian component of the Voigt profile, indicating the reflection spectrum in the absence of vibrations.

Figure 5.7 **b** displays the Fourier spectrum of the photodiode signal. We observe that a few characteristic resonances at 4 kHz, 10 kHz, 14 kHz, 19 kHz, etc., arising from the eigen-oscillations of the mechanical system are the main sources of the vibrations. We note that these vibrations at the mechanical eigen-frequencies could not be compensated by the active feedback loop, as it amplifies them already at a low gain. In the experiment, we limited the bandwidth of the feedback loop to 100 Hz.

The vibrations at kilohertz-frequencies are much slower than the optical processes in the cavity (characterized by g,  $\kappa$ ,  $\gamma$ ) and much faster than the typical integration time of our measurements ( $\sim 50 \,\mathrm{ms}$  for each data point). To model the spectra of the coupled molecule-cavity system in the presence of vibrations, we first recall the expressions of

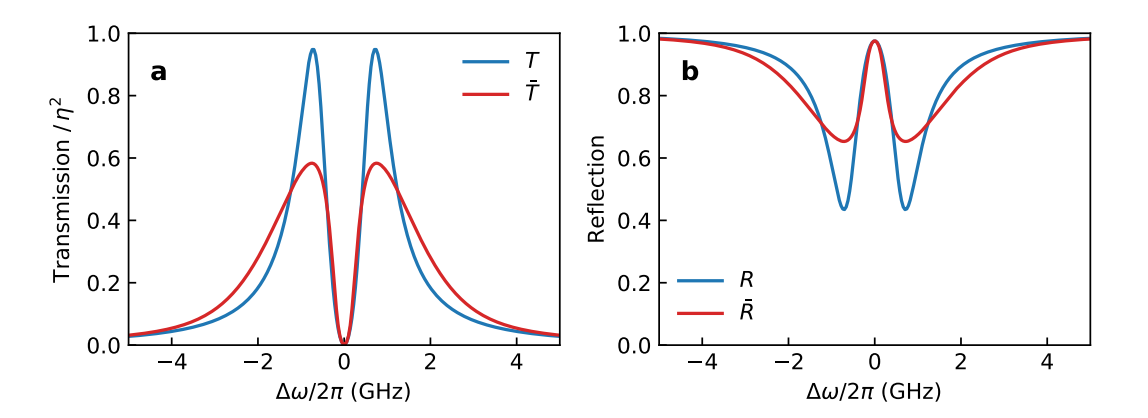


**Figure 5.8:** a, b, Transmission and reflection spectra of a resonantly coupled system. The blue lines represent the spectra with  $(\kappa, \gamma^0, \gamma')/2\pi = (1.66, 0.044, 1.21)$  GHz and  $\eta = 0.35$  without vibrational broadening. The red lines display results with a vibrational broadening of width  $\sigma/2\pi = 2.30$  GHz.

the complex coefficients r, t presented in chapter 2 for a vibration-free cavity

$$t = \eta \cdot \frac{-1}{1 - i\frac{\Delta\omega - \delta}{\kappa/2}} \cdot \left[ 1 - \frac{1}{1 + \left(i\frac{2\Delta\omega}{\gamma_{\text{cav}}} - \frac{\gamma^0}{\gamma_{\text{cav}}}\right) \left(i\frac{\Delta\omega - \delta}{\kappa/2} - 1\right)} \right],$$

$$r = 1 + t,$$
(5.8)

where  $\eta$  is a coefficient quantifying the in-/out-coupling efficiency of the cavity due to experimental imperfections in mode and impedance matches. The normalized transmission (reflection) coefficient in energy T(R) can be written as

$$T = |t|^2 ,$$

$$R = |r|^2 .$$
(5.9)

We can write the averaged transmission  $\bar{T}$  and reflection  $\bar{R}$  in the presence of vibrations as

$$\bar{T}(\delta) = \frac{\int G(\delta') \cdot T(\delta + \delta') \, d\delta'}{\int G(\delta') \, d\delta'},$$

$$\bar{R}(\delta) = \frac{\int G(\delta') \cdot R(\delta + \delta') \, d\delta'}{\int G(\delta') \, d\delta'},$$
(5.10)

where  $\delta'$  represents a deviation of the molecule-cavity detuning from the set value  $\delta$ . The occupation probability at each value of  $\delta'$  is modeled with a Gaussian function  $G(\delta') = \sqrt{4 \ln(2)/(\pi \sigma^2)} \cdot \exp\left[-4 \ln(2) \cdot (\delta'/\sigma)^2\right]$ .

The effect of vibrational broadening on the transmission and reflection spectra is illustrated in Figs. 5.8 **a**, **b**. The blue curves in the two plots display the spectra of a coupled system without considering vibrational broadening. The red curves show the spectra of the same system when vibrational broadening with width  $\sigma/2\pi=2.30\,\text{GHz}$  is present.

#### 5.3 Identifying a molecule in transmission

Having characterized the parameters of the cavity, we now study its coupling to single molecules. For this generation of dielectric coating, the 00ZPL wavelength (783 nm) is designed to be at the center of the band gap to minimize field penetration into the mirrors. In this case, the red-shifted fluorescence lies mostly within the band gap, thus does not couple out of the cavity efficiently.

Considering the high finesse of the cavity and hence a stronger molecule-cavity interaction, we expect to directly detect single molecules in the cavity's transmission spectrum. Figure 5.9 shows an example of identifying a molecule in the transmission signal. In this measurement, the cavity resonance is tuned stepwise from high to low frequencies. In each step, the laser frequency is scanned across the cavity resonance. At 382497 GHz, a molecule shows up as a Fano-shaped signal indicated by the black arrow.

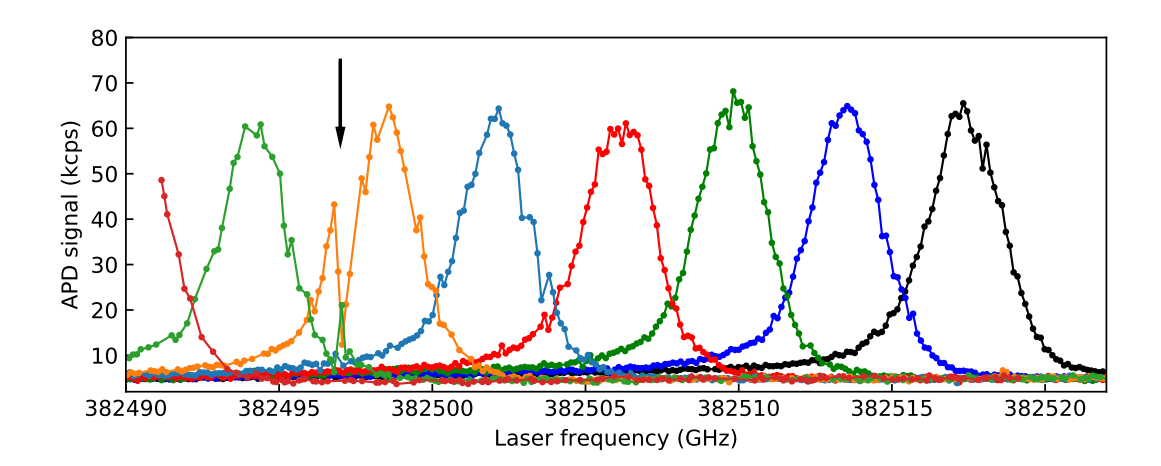


**Figure 5.9:** Searching for molecules in transmission. The colored dots display the measured transmission spectra at each frequency step of the cavity. A molecule coupled to the cavity introduces a modification to its transmission spectrum, as indicated by the black arrow.

#### 5.4 Resonant response of the molecule-cavity system

After a suitable molecule is identified, we first study its resonant coupling with the cavity mode. The blue dots in Fig. 5.10 a represent the measured transmission spectrum of an empty cavity. The solid blue line shows a fit to the measured data using a Voigt function. The red dots represent the transmission spectrum when the cavity is tuned on resonance with the molecule. The dip with a FWHM of around 600 MHz is a result of destructive interference of the molecular scattering with the cavity mode. The solid red line shows a theoretical fit using Eq. 5.10. The black dots display the measured signal when the laser frequency is far-detuned from the cavity resonance by about 20 GHz, providing a reference for the background level. The solid black line displays the average level of the measured background. A quantitative comparison of the three curves suggests that the presence of the molecule attenuates the resonant transmission of the cavity by more than 99%. This measurement is performed by detecting the cross-polarized reflection signal from the cavity (see chapter 3).

In Fig. 5.10 b, we present the same quantities measured for the transmitted light through the single-mode fiber hosting the micromirror. The solid lines represent the fits using the same group of cavity-QED parameters as for the data in a. The collection efficiency through the fiber is low due to the non-ideal mode matching between the cavity mode and the guided mode of the fiber, resulting in a lower signal to noise ratio. Nevertheless, the two sets of measurements provide the same information about the system and can be described using the same set of parameters.

Having examined the transmission spectra, we now perform the same measurements in reflection. In Fig.  $5.10\,\mathrm{c}$ , the blue dots display the cavity resonance measured in reflection while the black dots show the intensity of the reflected beam when it is  $20\,\mathrm{GHz}$  detuned from resonance. The empty cavity resonance does not dip to zero due to an imperfect mode matching and vibrational broadening. The red dots represent the reflection spectrum of the coupled system, revealing that the light is reflected to within  $1\,\%$  of the reflection from a far-detuned cavity.

The red dots in Fig.  $5.10\,\mathrm{d}$  display the fluorescence spectrum of the molecule when the cavity resonance is far-detuned. The solid red line represents a Lorentzian fit with a FWHM of  $44\pm5\,\mathrm{MHz}$ , revealing the unperturbed linewidth of the molecule and matches the typical values of DBT molecules in Ac crystals [52,64,114,116]. As mentioned before, the low signal to noise ratio of the fluorescence signal results from the high reflectivity of the dielectric mirrors at the frequencies of the red-shifted fluorescence. The fluorescence signal only leaks out via coupling to higher-order transver-

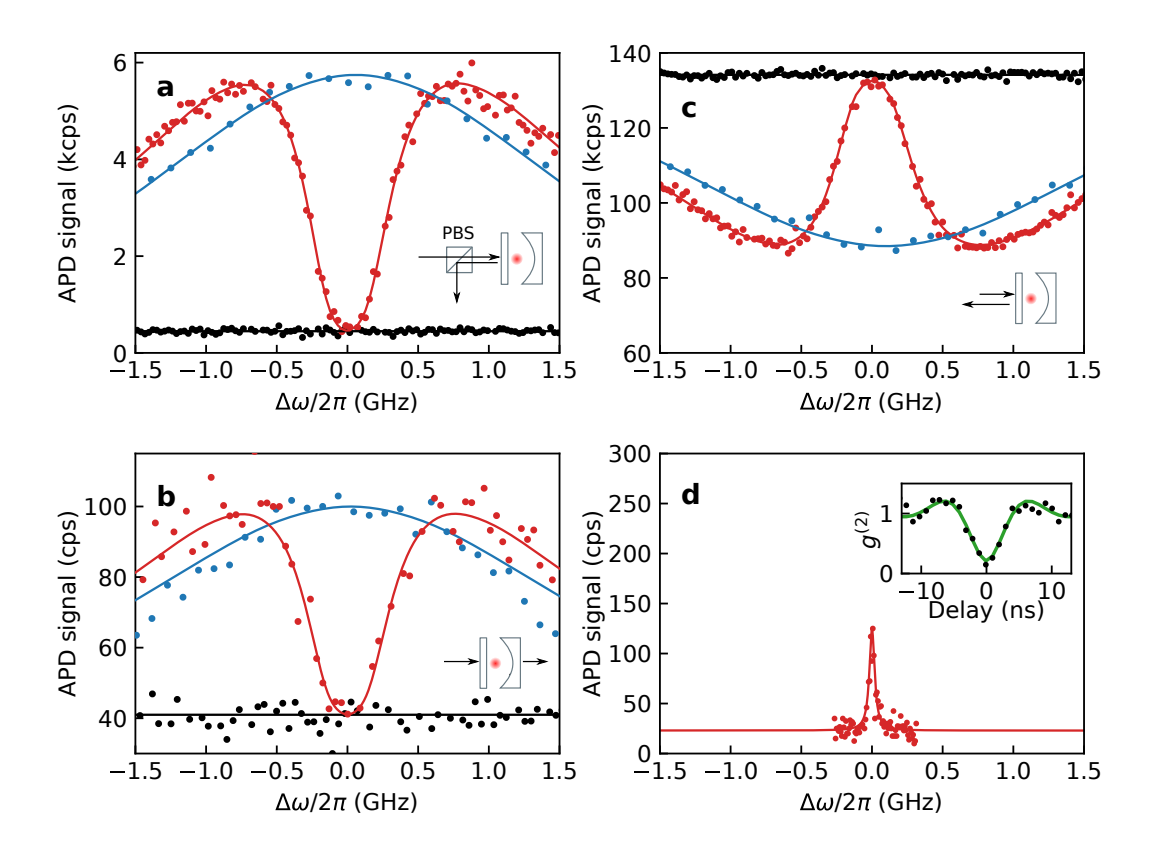


Figure 5.10: a, Cross-polarized reflection (CPR) spectrum of the coupled system. Black: intensity of the laser beam reflected from the cavity when it is detuned from the cavity and the molecular resonances, providing the background level. Blue: the CPR spectrum of the cavity when detuned from the molecule. Red: the CPR spectrum of the resonantly coupled molecule-cavity system. b, Same as in a but measured for the light transmitted through the single-mode fiber. c, Same as in a but measured in reflection without a cross polarizer. d, Fluorescence excitation spectrum of the same molecule recorded far detuned from the cavity resonance. The inset shows an intensity correlation of the fluorescence signal. A clear antibunching at zero time delay confirms that the observed signal comes from a single molecule. All solid curves denote theoretical fits.

sal modes of the cavity. The inset in Fig. 5.10 d displays the measured second-order intensity-correlation function (black dots) at the fluorescence peak. A theoretical fit to the measured data is performed, showing by the green line. The oscillations at the shoulders of the signal are signatures of Rabi-oscillations [117], as the measurement was performed at an elevated pump power. The resulting  $g^{(2)}(0) = 0.21 \pm 0.06$  confirms that the observed signal is from a single molecule.

#### 5.5 Cavity-QED parameters

The cavity-QED parameters of the system can be determined by comparing the linewidths of the molecule when the cavity is far-detuned ( $\gamma^0$ ) and when it is on resonance ( $\gamma'$ ). We follow the same analysis as in section 5.1.3 and express  $\gamma^0$  and  $\gamma'$  as

$$\gamma^{0} = \gamma_{\text{red}} + \gamma_{\text{zpl}},$$

$$\gamma' = \gamma_{\text{red}} + (1 + F) \cdot \gamma_{\text{zpl}}.$$
(5.11)

The values of  $\gamma^0$  and  $\gamma'$  are obtained from the spectral measurements to be  $44 \pm 5 \,\mathrm{MHz}$  and  $604 \pm 21 \,\mathrm{MHz}$ , respectively. Using these two values and considering that  $\gamma_{\mathrm{red}} \approx 2\gamma_{\mathrm{zpl}}$ , we determine the Purcell factor  $F = 38 \pm 5$  and the cooperativity  $C = 12.7 \pm 1.6$ . The conventions for F and C are explained in section 5.1.3. In short, F quantifies the modification to  $\gamma_{\mathrm{zpl}}^0$ , while C is normalized to the total decay rate  $\gamma^0$ . Using Eq. 5.4, we obtain the  $\beta$ -factor of the 00ZPL emission  $\beta_{\mathrm{zpl}} = 97.4 \pm 0.3\%$  and the cavity-modified branching ratio  $\alpha' = 95.1 \pm 0.6\%$ . The  $\beta$ -factor of the overall emission is  $\beta = \beta_{\mathrm{zpl}} \cdot \alpha' \approx 93\%$ . The three parameters close to unity indicate that the cavity changes the molecule to a nearly ideal two-level atom, and the emission of the molecule is strongly directional, i.e. preferentially into the cavity mode. The molecule-cavity coupling strength g can be deduced from the mode splitting plot which will be presented in the coming section.

We note that the estimation of the Purcell factor using Eq. 2.14 would result in F = 355, when assuming an effective refractive index of the medium n = 1.8. The discrepancy of the measured value of F = 38 from the ideal value is the result of several non-ideal factors. First, the misalignment of the DBT transition dipole to the **b**-axis of the anthracene crystal [64] can lead to a reduction of F by  $\sim 0.25$ . Second, a lack of control over the depth of the molecule in the crystal can introduce an offset of the molecule from the antinode of the cavity mode. An offset of 50 nm in depth would result in a reduction by a factor of 2. A displacement of about 80 nm would be sufficient to reduce the expected Purcell factor to the experimental value.

#### 5.6 Linewidth modification and Lamb shift

The fine tunability of the cavity allows us to study the molecule-cavity interaction in a controlled range of frequency detunings between them. Figure 5.11 displays a series

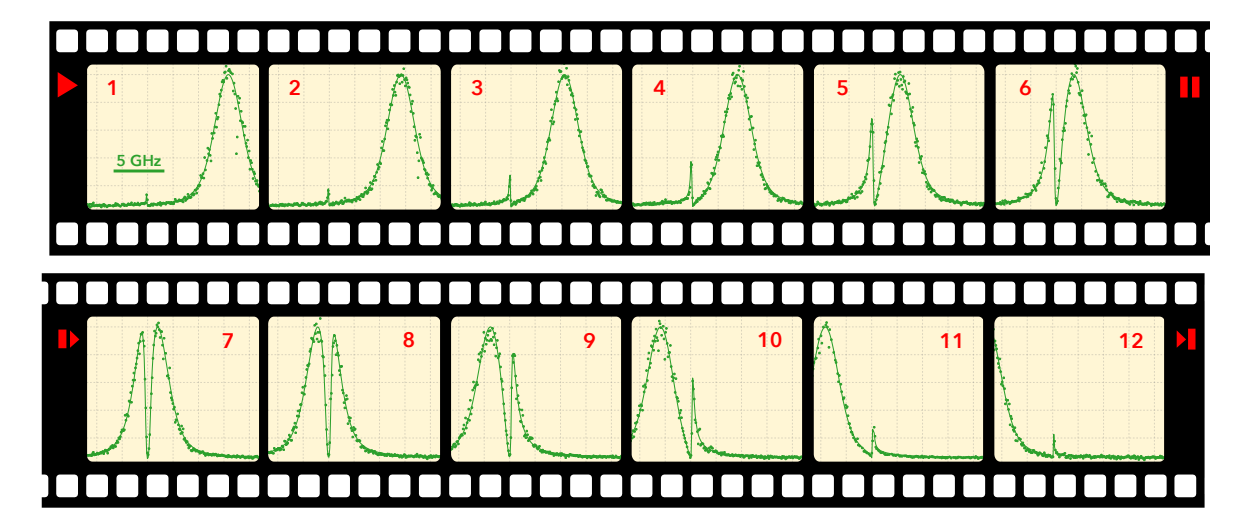


**Figure 5.11:** A series of transmission spectra through the coupled system when the cavity resonance is tuned across the molecular resonance. The dots display the measured data. The solid lines represent theoretical fits using Eq. 5.10.

of transmission spectra of the system when the cavity is tuned across the molecular resonance. The interference between the cavity mode and the light scattered by the molecule gives rise to Fano-shaped resonances which feature clear changes in lineshape and width.

We showed in chapter 2 that the normalized transmission spectrum of the system can be approximated to a product of the empty-cavity spectrum and a generalized Lorentzian function, which can be expressed as

$$T(\Delta\omega) = |t_0|^2 \cdot \frac{1 + a \cdot (\Delta\omega - \delta\omega_0)}{1 + \left(\frac{\Delta\omega - \delta\omega_0}{\gamma/2}\right)^2} , \qquad (5.12)$$

where  $t_0$  stands for the transmission coefficient of the empty cavity and a denotes the amplitude of the dispersive component. We first analyze the measured spectra in Fig. 5.11 using this model function to trace the changes in the molecular frequency and linewidth. Figures 5.12 **a**, **b** present the extracted frequency shift  $\delta\omega_0$  and linewidth  $\gamma$  of the molecule as a function of the molecule-cavity detuning  $\delta$ . The frequency of the 00ZPL transition is shifted towards blue or red, depending on the sign of  $\delta$ . This can be interpreted as modifications of the Lamb shift introduced by the cavity [54,55,118], i.e. the contribution of the vacuum fluctuations to the absolute value of the 00ZPL frequency. The cavity modifies the local density of states of the vacuum fields, leading to a shift of up to  $\pm 150\,\text{MHz}$ . The Purcell effect is evidenced by the broadening of the molecular linewidth from 44 MHz to about 600 MHz when the cavity is on resonance.

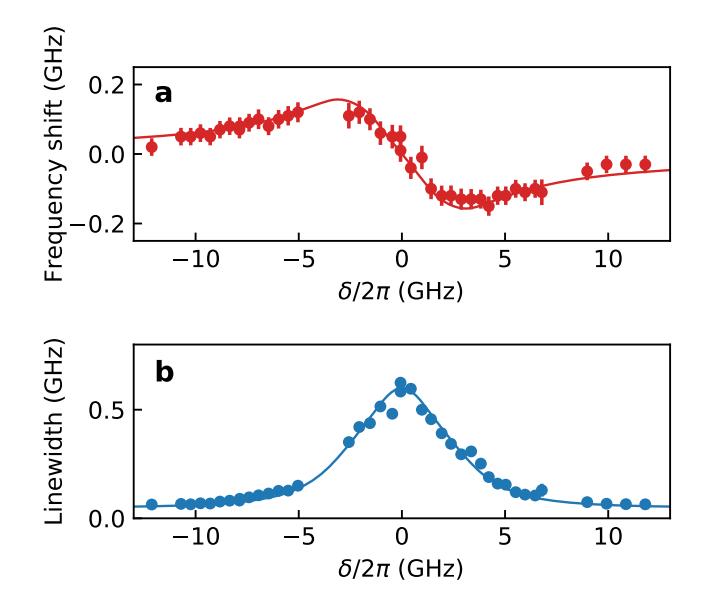


Figure 5.12: a, b, Shift in the 00ZPL transition frequency and the molecular linewidth versus the molecule-cavity detuning  $\delta$ . The colored dots represent the measured data. The solid lines show the corresponding quantities extracted from the theoretical spectra.

In the absence of the vibrational broadening of the cavity resonance, the frequency shift can be expressed as a dispersive function of  $\delta$  and the molecular linewidth is a Lorentzian function of  $\delta$  (see chapter 2). The vibrational broadening complicates the situation, making it difficult to obtain analytical expressions for the two quantities. To arrive at theoretical predictions for the measured data, we apply the same fitting routine to the theoretical spectra calculated using Eq. 5.10 and the deduced cavity-QED parameters. The obtained frequency shift and linewidth are plotted as the solid lines in Fig. 5.12 a and b.

#### 5.7 Onset of strong coupling

In the previous section, we treated the molecule and the cavity as uncoupled systems to trace the changes in the molecular frequency and linewidth. We now turn to analyzing the spectra using the rigorous theory introduced in chapter 2, where the molecule and the cavity are considered a coupled system.

The solid lines in Fig. 5.11 display the theoretical fits to the measured spectra using Eq. 5.10. The whole series is fitted using a single set of parameters  $(\kappa, \gamma^0, \gamma', \sigma)/2\pi = (1.66, 0.44, 1.21, 2.29)$  GHz. In Fig. 5.13, we plot the positions of the higher- and lower-energy transmission maxima as a function of the molecule-cavity detuning. The solid

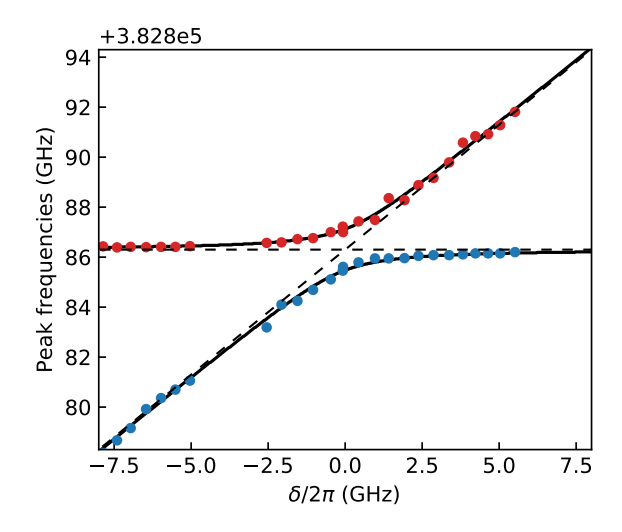
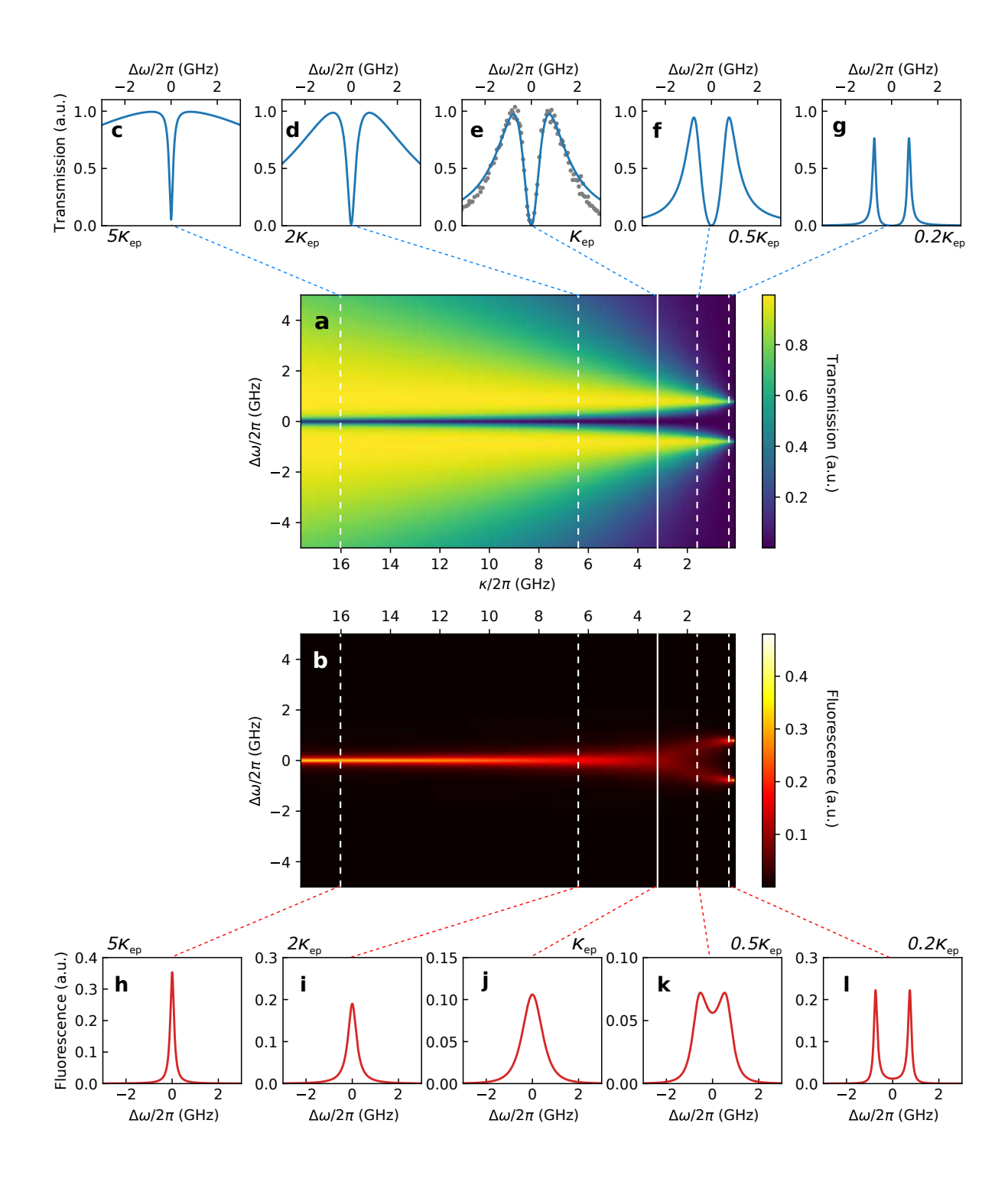


Figure 5.13: Frequency of the higher- (red dots) and lower- (blue dots) energy transmission peaks as a function of the molecule-cavity detuning. Black lines present the same quantities extracted from the fitted theoretical spectra. The amount of splitting at zero detuning corresponds to 2q.

lines display the same quantities extracted from the theoretical spectra. The amount of splitting between the two maxima at zero detuning equals 2g, allowing us to obtain  $g/2\pi = 0.79 \pm 0.3 \,\text{GHz}$ . We note that a variation of g between  $0.75 \,\text{GHz}$  to  $0.82 \,\text{GHz}$  is present in different measurements. This is due to slight differences in the lateral position of the molecule, after realignment of the cavity.

The mode-splitting in transmission is usually associated with strong coupling. However, a more decisive signature for entering the strong coupling regime is the bifurcation of eigenstates [27, 50], which occurs at the exceptional point (EP) of  $g = (\kappa - \gamma^0)/4$  and is observable in fluorescence, rather than in transmission [27, 50]. In our system,  $g \approx (\kappa - \gamma^0)/4$ , implying that the system is at the onset of strong coupling. To better assert our experimental regime and visualize the transition from weak to strong coupling, we calculate the transmission and fluorescence spectra of the system while scaling the cavity linewidth from its experiment value and keeping the measured value of g. The scaling corresponds to an experimental situation, where the mode volume of a cavity is kept unchanged but the finesse is increased or decreased.

Fig. 5.14 **a**, **b** display the calculated transmission and fluorescence spectra of the system with the horizontal axis denoting the linewidth of the cavity. The transmission spectrum  $T(\Delta\omega)$  is calculated using Eq. 5.8 and Eq. 5.9. The fluorescence spectra  $L(\Delta\omega)$  are obtained using  $L(\Delta\omega) = 1 - T(\Delta\omega) - R(\Delta\omega)$ .



**Figure 5.14: a**,**b**, Calculated transmission and fluorescence spectra of the coupled system as a function of the cavity linewidth  $\kappa$ , respectively. The solid white lines mark the location of the EP. **c-g**, Cross sectional transmission spectra at cavity linewidths displayed at the bottom of each plot and marked by the dashed white lines in **a**. The experimentally measured transmission spectrum is superposed on the calculated spectrum at the EP, shown by the gray dots in **e**. The lower panel (**h-l**) displays the same as the upper panel but for the fluorescence spectra. The cavity linewidth satisfying the EP condition  $\kappa_{\rm ep}$  amounts to  $(4g + \gamma^0)/2\pi = 3.2\,{\rm GHz}$ . See text for details.

**92** 5.8. Phase-shift

Given the measured values of g and  $\kappa$ , the cavity linewidth which satisfies the EP condition can be obtained with  $\kappa_{\rm ep} = (4g + \gamma^0)/2\pi = 3.2\,\rm GHz$ . In the upper panel of Fig. 5.14 (**c-g**), we plot the cross-sectional transmission spectra at different cavity linewidths expressed as multiples of  $\kappa_{\rm ep}$ . We find that the splitting of the transmission spectra appears independent of the cavity linewidth, i.e. even when the system is deeply in the weak-coupling regime (see **c**).

The location of the EP is marked out by the solid white line in **a**, and the corresponding transmission spectrum is represented by the blue line in Fig. 5.14 **e**. The measured transmission spectrum of the system is displayed by the gray dots in **e**. The close agreement between the experimental and the calculated EP spectrum confirms that our system is at the onset of the strong coupling. The small offsets at the shoulders of the spectra are a result of vibrational broadening of the cavity resonance, which leads to deviations of the measured spectrum from a Lorentzian profile.

The fluorescence spectra (see Figs. 5.14  $\bf b$  and  $\bf h$ - $\bf l$ ) evolve differently from the transmission spectra. In the weak-coupling regime, the fluorescence spectrum is a Lorentzian profile whose linewidth is the Purcell-enhanced linewidth of the molecule (see  $\bf h$ ,  $\bf i$ ). At the EP, the fluorescence spectrum becomes flat-topped (see  $\bf j$ , and Ref. [119]). After entering the strong coupling regime, the fluorescence spectrum splits into two peaks, as shown by Figs. 5.14  $\bf k$ ,  $\bf l$ .

#### 5.8 Phase-shift

As discussed in chapter 2, the scattering of light by a quantum emitter is accompanied by a phase shift. Previous experiments have observed phase shifts of up to three degrees with single atoms [120], ions [121,122] and molecules [123] in free space. By coupling an atom to a single-sided optical cavity [124], phase shifts of up to 180° can be measured in reflection [56,125]. The large phase shift originates from the difference in optical path length, when a photon enters the cavity or is reflected from the entrance mirror, controlled by the state of the atom. The light transmitted through a symmetric cavity has a maximum achievable phase shift of  $\pm 90^{\circ}$ . An experiment using a single atom in this geometry has shown a phase shift of  $\pm 34^{\circ}$  [126]. Considering the high cooperativity of our system, it is interesting to explore how large of a phase shift is imprinted by the molecule-cavity system on a transmitted laser beam.

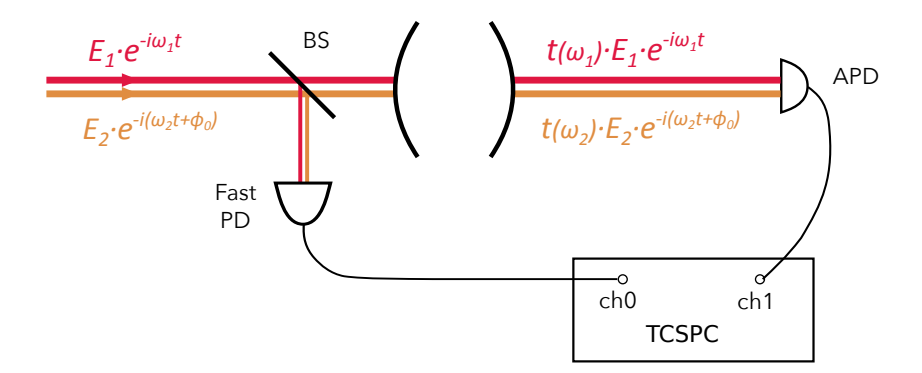


**Figure 5.15:** Illustration of the two-frequency interferometer. BS, beam sampler; Fast PD, fast photodiode; APD, avalanche photodiode; TCSPC, time-correlated single-photon counting device.

#### 5.8.1 A two-frequency interferometer

To measure the phase shift, we follow the scheme introduced in Ref. [123] and employ a two-frequency common-path interferometer. The concept of the interferometer is illustrated in Fig. 5.15. Two laser beams with electric fields  $|E_1| \cdot e^{-i\omega_1 t}$  and  $|E_2| \cdot e^{-i(\omega_2 t + \phi_0)}$  are combined and forwarded to the cavity. Here,  $\omega_1$  and  $\omega_2$  denote the frequency of the two laser beams and  $|E_1|$ ,  $|E_2|$  represent their electric field amplitudes, respectively. The two beams have an initial phase difference  $\phi_0$ . Before they enter the cavity, a beam sampler reflects part of the light onto a fast photodiode. The intensity on the photodiode can be written as

$$I_{\rm bs} = R_{\rm bs} \cdot \{ |E_1|^2 + |E_2|^2 + 2|E_1| \cdot |E_2| \cos[(\omega_2 - \omega_1)t + \phi_0] \}, \qquad (5.13)$$

where  $R_{\rm bs}$  denotes the reflectivity of the beam sampler. The intensity consists of two constant terms and a cosine term representing a beating signal at frequency  $\omega_2 - \omega_1$ . The starting phase of the beating signal is given by  $\phi_0$ .

The complex transmission coefficients of the cavity at  $\omega_1$  and  $\omega_2$  can be expressed as

$$t(\omega_1) = |t(\omega_1)| \cdot e^{-i\phi(\omega_1)},$$
  

$$t(\omega_2) = |t(\omega_2)| \cdot e^{-i\phi(\omega_2)}.$$
(5.14)

The intensity of the light transmitted through the cavity is then

$$I_{\rm t} = (1 - R_{\rm bs}) \cdot \{|t(\omega_1)|^2 \cdot |E_1|^2 + |t(\omega_2)|^2 \cdot |E_2|^2$$

**94** 5.8. Phase-shift

+ 2 
$$|E_1| \cdot |E_2| \cdot |t(\omega_1)| \cdot |t(\omega_2)| \cdot \cos[(\omega_2 - \omega_1)t - (\phi_2(\omega_2) - \phi_1(\omega_1)) + \phi_0] \}$$
, (5.15)

which also consists of two constant terms  $|t(\omega_1)|^2 \cdot |E_1|^2$ ,  $|t(\omega_2)|^2 \cdot |E_2|^2$  and a beating signal at frequency  $\omega_2 - \omega_1$ . The starting phase of the beating signal is shifted by  $\Delta \phi = \phi_2(\omega_2) - \phi_1(\omega_1)$  with respect to the initial phase difference  $\phi_0$ . The phase shift imprinted on the two beams is thus mapped onto the phase of the beating signal, which can be measured using time-correlated single-photon counting (TCSPC) techniques.

#### 5.8.2 Experimental implementation

Figure 5.16 a displays the schematic of the optical setup for generating two frequency-separated laser beams. The light from a Ti:sapphire laser is first sent through an AOM (AOM1: 3200-125, Gooch & Housego PLC) operating at 200 MHz for intensity stabilization. After passing AOM1, the first diffraction order is selected with an iris and sent to a second AOM (AOM2: EF 300-200, Brimrose Co), which is driven at a radio frequency of 330 MHz. After passing AOM2, the fundamental (zeroth) and the second diffraction order, which are frequency separated by twice the radio frequency (660 MHz) are selected and combined at a beamsplitter. A variable neutral-density filter is placed in the path of the zeroth-order beam to balance the two beams' intensities. The combined beam is coupled to a single-mode fiber which guides the light to the experiment. A photograph of the optical setup is shown in Fig. 5.16 b.

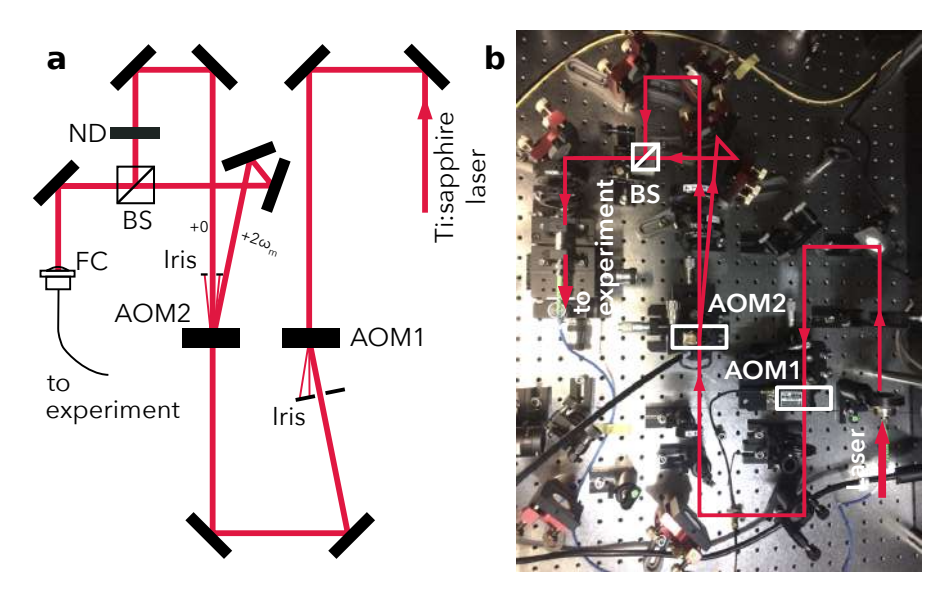


**Figure 5.16: a**, Schematics of the optical setup for generating two frequency-separated laser beams. AOM, acousto-optic modulator; ND, variable neutral density filter; BS, beamsplitter; FC, fiber coupler. **b**, A photograph of the experimental setup illustrated by **a**.

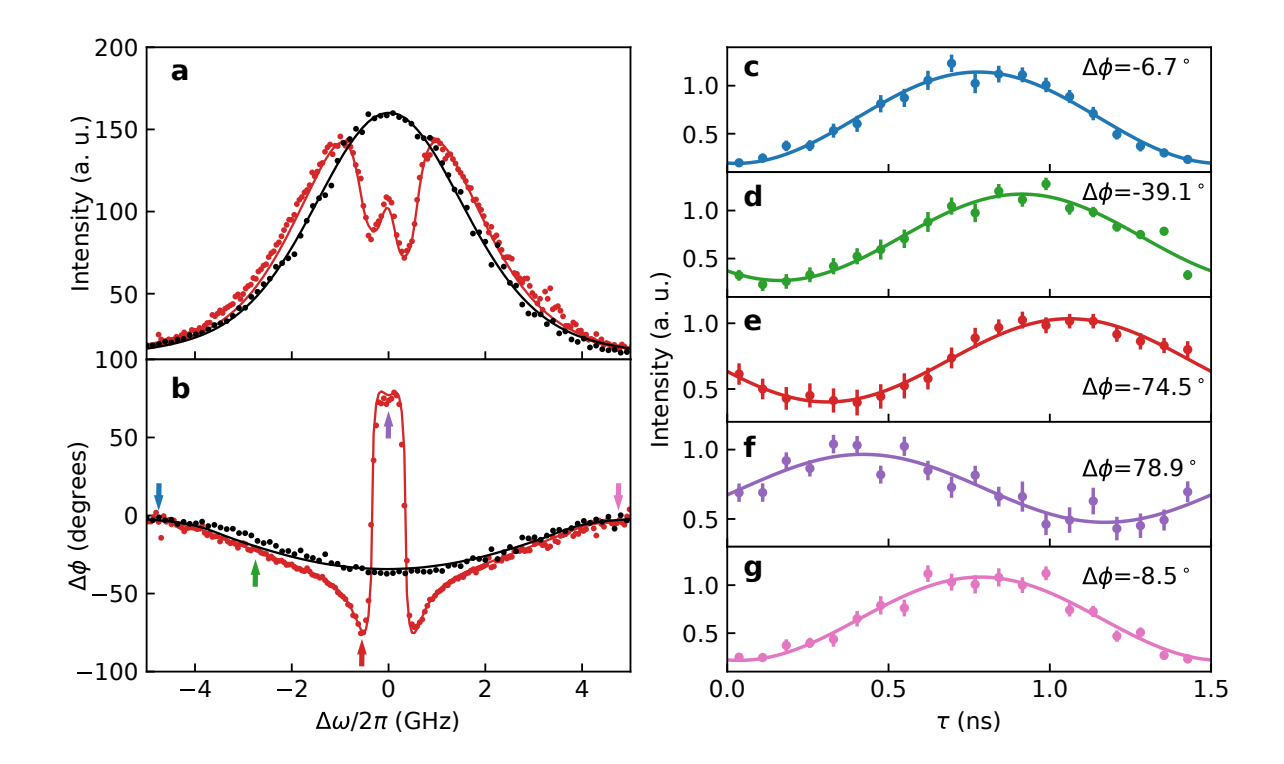


**Figure 5.17: a, b**, Transmitted laser intensity and starting phase of the beating signal as a function of the laser frequency detuning, respectively. The red dots represent the measured data from the resonantly coupled molecule-cavity system and black dots represent that on an empty cavity. All solid lines represent theoretical fits. An initial phase difference between the two laser beams of 198° is subtracted from the data in **b. c-g**, The colored dots represent the measured oscillation signals at the laser frequency detunings marked by the correspondingly colored arrows in **b**. The solid lines display fits to a sinusoidal function. The shifts in the starting phase are displayed in the legends.

Before the combined beam is sent to the cavity, a beam sampler reflects part of the beam and sends it to a fast avalanche photodetector (APD210, Menlo systems Inc.). The sinusoidal signal measured by this detector is fed to a TCSPC device (Picoharp300, PicoQuant GmbH) to serve as a trigger signal. The frequency of the Ti:sapphire laser is tuned across the resonance of the coupled molecule-cavity system, while the arrival time of each transmitted photon with respect to its previous trigger event is recorded by the TCSPC device. At each laser frequency, a histogram of the time delays of the photon detection events is generated. A sinusoidal fit to each of the histograms is performed to extract the starting phase of the beating signal.

Figure 5.17 a displays the transmitted intensity through the coupled system (red dots) and the empty cavity (black dots) versus the laser frequency detuning. The two dips around the zero detuning correspond to the extinction signals from each of the beams interacting with the molecule separately. The depth of each dip is about 50% of

**96** 5.8. Phase-shift

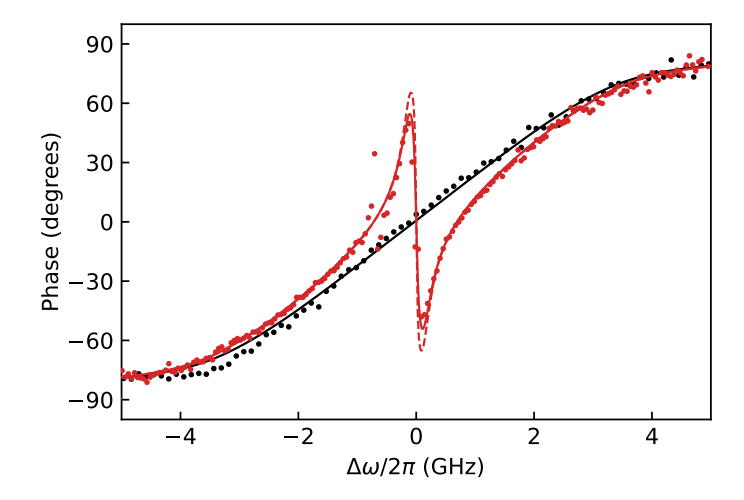


**Figure 5.18:** Red dots display the phase shift of a single laser beam after subtracting the effect of the other beam. The solid red line represents the theoretical prediction of the single-beam phase shift accounting for the saturation broadening of the molecule. The dashed red line represents the phase shift of a laser beam in the weak-excitation limit. The phase shift of an empty cavity is shown by the black dots (extracted from the measurement) and the black line (theoretical prediction). See text for details.

the maximal transmission. This is due to the fact that when one beam is tuned on resonance with the molecule, the second beam is off resonance by 660 MHz and introduces a background on the resonant signal. The red (black) dots in Fig. 5.17 b present the extracted starting phase of the beating signals for the resonantly coupled system (an empty cavity). The two steep transitions separated by 660 MHz result from the phase shift of each of the laser beams interacting with the molecule. The solid lines in Fig. 5.17 a, b represent parallel theoretical fits to the measured data. We note that the measurements are performed at a slightly higher excitation power to keep the integration times short. In the theoretical fit, we have kept the measured cavity-QED parameters fixed while allowing a small linewidth broadening ( $40 \pm 8 \,\mathrm{MHz}$ ) on the molecule to account for the saturation effect. A series of beating signals are displayed in Fig. 5.17 c-g to visualize the phase shift.

The data displayed in Fig. 5.17 b clearly show the effect of the molecule on the phase of the two laser beams. However, it will be more instructive to present the phase shift on a single laser beam. In Fig. 5.18, we plot the phase shift of a single beam after subtracting the effect of the second beam. The effect of the second beam is calculated using the fit parameters, by taking the difference in the phase of the beating signal for the experimental configuration and for the case where the second beam is far detuned (by 1 THz). The dots and the solid line represent the corresponding data in Fig. 5.17 b

after subtracting the effect of the second beam. The red dashed line in Fig. 5.18 displays the phase shift on a single beam when assuming no power broadening of the molecule.

98 5.8. Phase-shift

### Chapter 6

# Nonlinearity at the single-photon level

The content of the chapter is part of the following manuscript:

Turning a molecule into a coherent two-level quantum system by D. Wang, H. Kelkar, D.-M. Cano, D. Rattenbacher, A. Shkarin, T. Utikal, S. Götzinger and V. Sandoghdar, Nat. Phys. (2019), in press.

Some passages of the present text are similar to the text in the manuscript.

Having one photon interacting with another is at the ultimate limit of nonlinear optics. Conventional nonlinear optical experiments are performed with intense lasers and bulk materials [127]. This is very different from the regime where the incident light is weak or in particular at the level of single-photons [128].

Interestingly, it is possible to realize strong interactions between photons using a two-level system (TLS) in free-space [129] or coupled to a confined mode [130–132]. The photon-photon interaction arises from the fact that a TLS can only scatter one photon at a time. When the TLS is coupled very efficiently to a single mode, the scattered photon interferes strongly with a second photon in the mode, thus imprinting strong correlations on them. This effect can be utilized to realize functional operations for quantum optics, such as photon-sorting, Bell-state measurement and controlled-Z gate [131, 132].

In this chapter, we investigate the nonlinearity of the coupled molecule-cavity system at temperature  $T=4.2\,\mathrm{K}$ . We find that the system can be saturated with 0.44 photons per excited-state lifetime of the molecule. As a result of the strong nonlinearity, we observe changes in the photon correlations of the light transmitted through the system. To take one step further towards demonstrating photon-photon interactions, we perform measurements on the coupled system using single antibunched photons generated by a second molecule in a neighboring lab.

#### 6.1 Saturation of the system

We characterize the nonlinear response of the system by measuring the saturation of its steady-state transmission. The black dots in Fig. 6.1 a-d display a series of transmission spectra of the resonantly coupled molecule-cavity system measured at different laser powers. The red lines stand for the theoretical fits and the dashed green lines represent the transmission spectra of an empty cavity. The background level for each measurement is shown by the signal in blue. The incoming laser powers are measured in front of the cryostat and displayed in the legends.

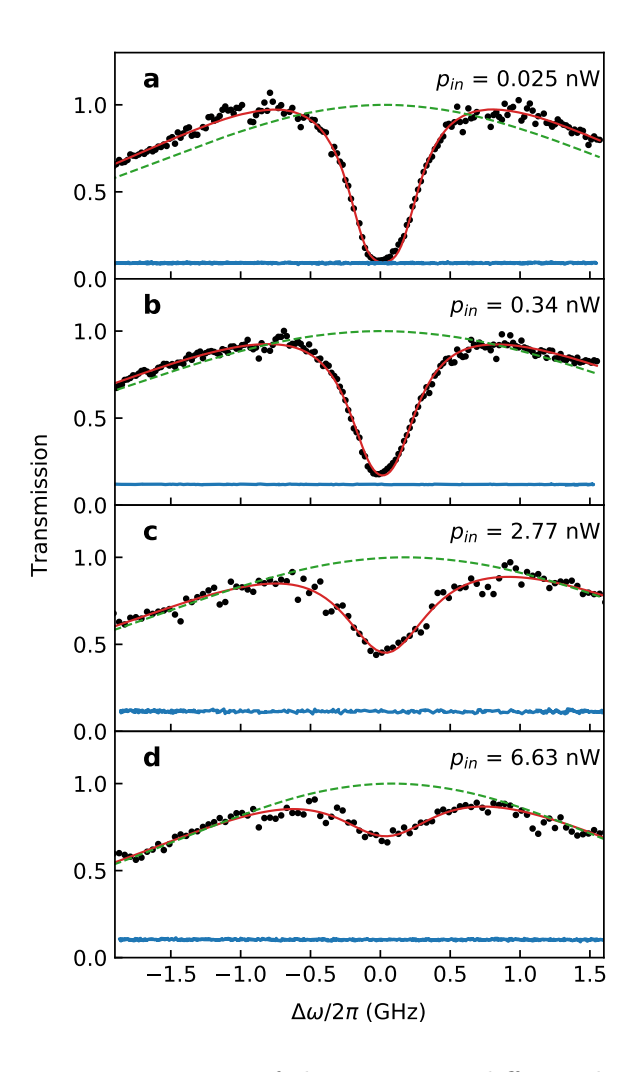


**Figure 6.1:** a-d, Transmission spectra of the system at different laser powers. The black dots represent the measured data and red curves show theoretical fits. The dashed green lines stand for the transmission spectra of an empty cavity, calculated using the fit parameters. The blue signals display the background levels measured by detuning the cavity resonance by approximately 20 GHz. The incident laser power for each measurement is displayed in the corresponding legend.

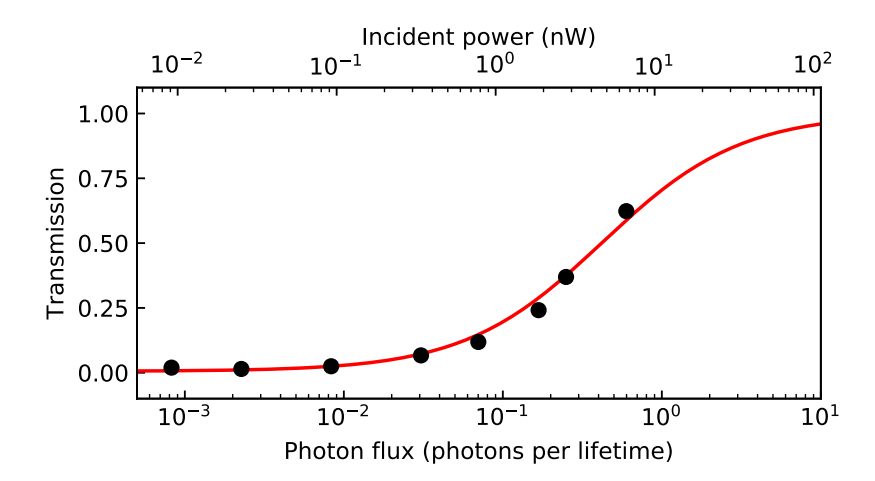


**Figure 6.2:** Saturation of the resonant transmission. The vertical axis denotes the resonant transmission of the coupled system normalized to that of the empty cavity. The upper horizontal axis presents the measured power before the cryostat window. The lower horizontal axis shows the estimated photon flux at the molecule per Purcell-enhanced lifetime of it. Black dots display the measured data. The red line represents a theoretical fit.

When the incident power is low, the coherent interaction between the molecule and the cavity modifies the transmission spectrum significantly, leading to a strong attenuation of the resonant transmission (see  $\mathbf{a}, \mathbf{b}$ ). As the laser power increases, the molecule is gradually saturated, accompanied by the reduction of the extinction signal and the broadening in the molecular linewidth (see  $\mathbf{c}, \mathbf{d}$ ).

The incident laser power can be calibrated to the photon flux  $n_{\rm in}$  through the cavity per excited-state lifetime of the molecule. We start from the measured laser powers, account for the transmission of the four window plates ( $\sim 87\%$ ), the incoupling efficiency to the cavity ( $\sim 10\%$ ) and the Fourier-limited lifetime of the molecule (264 ps). One photon per excited-state lifetime of the molecule translates to 11 nW of incident power in front of the cryostat. The incoupling efficiency is measured by monitoring the depth of the reflection dip from an empty cavity. This number is limited by the vibrational broadening and a polarization offset of the incident laser beam to allow for cross-polarized detection. When the incoming polarization is aligned to the cavity mode, the incoupling efficiency can be increased to  $\sim 34\%$  (see Fig. 5.10 b).

The resonant transmission of the coupled system normalized to that of the empty cavity is plotted as a function of the laser power in Fig. 6.2. The upper horizontal axis displays the measured incident powers in front of the cryostat, while the lower horizontal axis shows the calibrated photon flux per Purcell-enhanced lifetime of the molecule. The

red line represents a theoretical fit using

$$T = \left(1 - \frac{\beta}{1+S}\right)^2 + \beta^2 \cdot \frac{S}{(1+S)^2}.$$
 (6.1)

Here,  $S = n_{\rm in}/n_{\rm c}$  is the saturation parameter with  $n_{\rm c}$  the critical photon number to reach S = 1 (excited-state occupation probability of 25%). The fit gives  $n_{\rm c} = 0.44$ , meaning that only 0.44 photon per lifetime is necessary to reach S = 1. With one incident photon per lifetime, the system is expected to reach  $S \approx 2.3$ . This set of measurements is direct proof of the single-photon nonlinearly of the system.

#### 6.2 Photon statistics of the transmitted light

A system exhibiting single-photon nonlinearity should respond differently to incident Fock-states of different photon numbers. When probing the system with a coherent state, the light transmitted through the system should feature a change in its photon statistics.

In chapter 2, we introduced the theoretical model for describing the photon statistics of the transmitted light. The modification of photon statistics results from the dynamic exchange of excitation between the emitter and the cavity, and stems from the fact that a single emitter can only scatter one photon at a time [58–60]. In this section, we present the measurements of the photon statistics at controlled cavity and laser frequency detunings. We quantify the non-classicality of the observed signals by bounding them with a set of Schwarz-inequalities.

#### 6.2.1 Resonant transmission: strong photon-bunching

We first set both the cavity resonance and the laser frequency on resonance with the molecule. The light transmitted through the system (via cross-polarized detection in reflection) is sent to a Hanbury Brown and Twiss (HBT) setup consisting of a 50:50 beamsplitter and two fast avalanche photodetectors (APD: PDM100, Micro Photon Devices). The black dots in Fig. 6.3 a display the measured second-order correlation versus the time delay  $\tau$  between the signals from the two APDs. A strong photon bunching at zero time delay is observed with a peak height of  $g^{(2)}(0) \approx 21$ .

The origin of photon bunching in the regime of  $C > \sqrt{2}$  is explained in chapter 2. In this regime, the two-photon transmission has a higher probability than that of single-

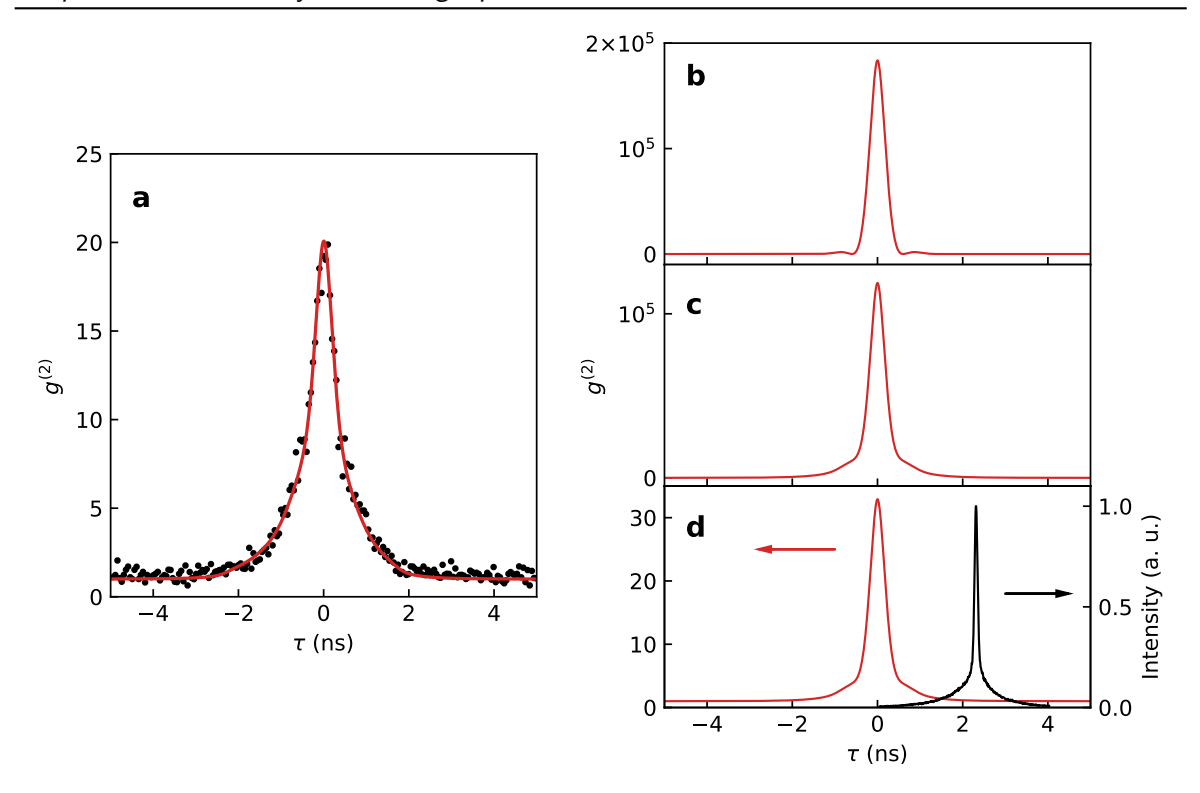


**Figure 6.3: a**, Black dots display the measured intensity-correlation function of the resonantly transmitted light. Photon bunching with a maximal value of 21 is observed at zero time delay. The red line represents a theoretical fit considering the vibrational broadening, background light and the instrument response. **b**, Intensity-correlation function calculated using the fit parameters but excluding the three factors mentioned above. **c**, Same as in **b** but including the vibrational broadening and background light. The signal in black displays the instrumental response function. The offset of about 2 ns is added intentionally for the clarity of the signal.

photons. As a result, the probability of finding two-photon states in the transmitted light is higher than that given by Poissonian statistics.

In fact, an estimation using the formula  $g^{(2)}(0) = (1 - C^2)^2$  would give  $g^{(2)}(0) \approx 25700$  for C = 12.7, which is much larger than the observed value. It turns out that some extra factors need to be taken into account to explain the observed signal. First, the vibrational perturbations to the cavity lead to a change in the molecule-cavity detuning during the measurement. Second, the instrumental response function (IRF) broadens and reduces the amplitude of the bunching peak. Lastly, Poissonian background light on the detectors lifts the background level of the  $g^{(2)}$  signal. The contribution of the background light becomes particularly significant at high values of extinction. A complete model accounting for the three factors can be expressed as

$$g_{\text{exp}}^{(2)}(\tau) = 1 + \left[ \frac{\int G(\delta') \cdot T(\delta')^2 \cdot g^{(2)}(\delta'; \tau) \,d\delta'}{\int G(\delta') \cdot T(\delta')^2 \,d\delta'} * f_{\text{IRF}}(\tau) \right] \cdot (1 + r_{\text{bkg}})^{-2}, \tag{6.2}$$

where  $T(\delta')$  denotes the transmission of the coupled system at the molecule-cavity detuning of  $\delta'$ ,  $f_{\rm IRF}$  stands for the instrumental response function and  $r_{\rm bkg}$  is the ratio of background-light intensity to that of the signal. The red solid line in Fig. 6.3 a displays the theoretical fit to the measured data using this model function. Figures 6.3 b-d present the effect of the three factors on  $g^{(2)}(\tau)$ .

Figure 6.3 **b** displays the intensity-correlation function calculated using the fit parameters but neglecting the effects of the three factors, where the photon bunching reaches  $g^{(2)}(0) \approx 1.8 \times 10^5$ . The value is larger than the estimated value of 25700, since we consider here a vibration-free cavity which leads to a larger C. The intensity-correlation function accounting for the vibrational broadening is displayed in Figure 6.3 **c**. The background light falling on the detectors further reduces the amplitude of the bunching, shown by the red line in Fig. 6.3 **d**. The black line in the same plot displays the measured IRF of the system. A convolution of the red and the black curves results in the fit curve for the measured data shown by the red solid line in Fig. 6.3 **a**. The background light is the main source of the reduction of the photon bunching. We note that the strong attenuation in transmission to the value of  $(1 - \beta)^2 \approx 0.5\%$  results in a small signal to background ratio for the measurements.

Nevertheless, the observed  $g^{(2)}(0) \approx 21$  is among the highest values of photon bunching reported from a single emitter [17,125,133–135] and is promising for realizing a photon sorter [131,132,134].

# 6.2.2 Detuned transmission: from classical to non-classical fluctuations

The fine frequency control of the open Fabry-Pérot cavity allows us to explore the variations in photon statistics at different cavity and laser frequency detunings. The black dots in Fig. 6.4 **a-f** display the measured intensity-correlation functions on the lower-frequency transmission peak when the cavity resonance is tuned from the blue to the red side of the molecule. The theoretical fits using Eqs. 6.2, 2.60 and 2.61 are shown by the solid red lines. The corresponding transmission spectra for the measurements in **a-f** are shown in **g-l** with the cavity detunings displayed in the legends and the laser frequencies marked by the dashed orange lines.

In Fig. 6.4 **a-e**, the intensity-correlation functions appear 'W'-shaped, with the value of  $g^{(2)}(0)$  changing from 0.85 to 1.1 and then back to 1. The width of the 'W'-shaped feature decreases as the cavity is tuned closer to the molecule. In chapter 2, we showed

that the intracavity field a can be expressed as the sum of the driving field E and the scattered field from the molecule  $g\sigma_{-}$ . The former is a coherent state following Poissonian statistics and the latter takes the properties of the resonant scattering by a single atom, which is antibunched. At large molecule-cavity detunings, the main contribution to the lower-frequency transmission peak is from the molecular scattering. The signal appears therefore antibunched (see a, b). When the cavity is tuned to the blue side of the molecule, the lower-frequency transmission peak changes from 'molecule'-like to 'cavity'-like. The intracavity field is mainly from the driving field E, which follows Poissonian statistics and does not feature a correlation (see f). The reduction in the feature width from a to d results from the Purcell effect, i.e. the lifetime of the molecule is reduced as the cavity is tuned closer to the molecule. The oscillatory behavior around zero time delay is a result of the wavefunction collapse when a photon leaves the cavity, which leads to a sudden change in the amplitude of the intracavity field (see Ref. [60]).

Using the measured intensity-correlation functions, one can classify the intensity fluctuation of the field under study as classical or nonclassical. In Ref. [59], a set of three inequalities were summarized to bound the intensity fluctuation of a classical field:

$$g^{(2)}(0) \ge 1, \tag{6.3}$$

$$g^{(2)}(\tau) \le g^{(2)}(0), \tag{6.4}$$

$$|g^{(2)}(\tau) - 1| \le |g^{(2)}(0) - 1|.$$
 (6.5)

All three inequalities can be derived from the Cauchy-Schwarz inequality [59]. The first inequality shows that a classical light field cannot show antibunching, i.e. the intensity fluctuation of a classical field is bounded by the shot noise [136]. The second shows that the  $g^{(2)}$ -function of a classical field cannot exceed its value at zero time delay. The third is derived by decomposing the intensity into its mean value and the fluctuation, implying that the maximal deviation of the  $g^{(2)}$ -function from one should appear at zero time delay. A violation of one of the three inequalities means that the field under study is nonclassical.

The solid blue lines in Fig 6.4 **a-e** mark the levels of  $g^{(2)}(0)$  in each of the plots, while the dashed blue lines show the levels of  $2 - g^{(2)}(0)$ . The areas in between the two lines are within the bound of Eq. 6.5. The numbers listed in the upper right corners of Fig 6.4 **a-f** indicate the inequalities violated in each data set. For larger cavity detunings (**a-b**), all three inequalities are violated. In this regime, the field is nonclassical since the main contribution comes from the scattering of the molecule.

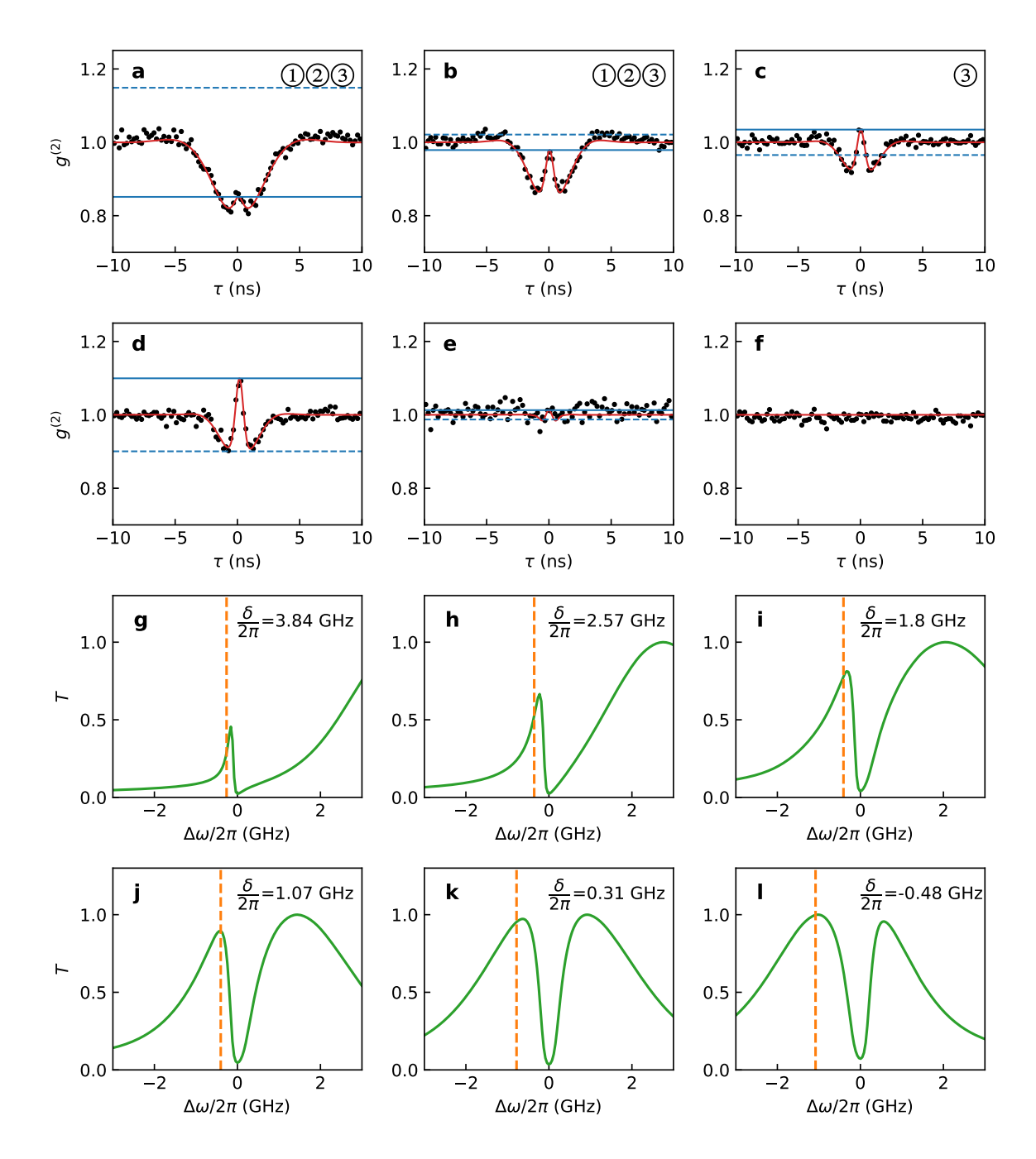


**Figure 6.4:** Photon statistics measured on the lower-frequency transmission peak at different cavity detunings. **a-f**, Measured  $g^{(2)}$ -functions (black dots) and theoretical fits (red solid lines) at cavity detunings illustrated by the transmission spectra in **g-l**, respectively. The solid blue lines mark the levels of  $g^{(2)}(0)$ , while the dashed blue lines indicate the levels of  $2 - g^{(2)}(0)$ . The numbers in the upper right corner of each plot show the inequalities (see Eqs. 6.3-6.5) violated by the data. **g-l**, Transmission spectra (green curves) and laser frequencies (dashed orange lines) for the measurements in **a-f**. The cavity detuning for each measurement is displayed in the upper right corner.

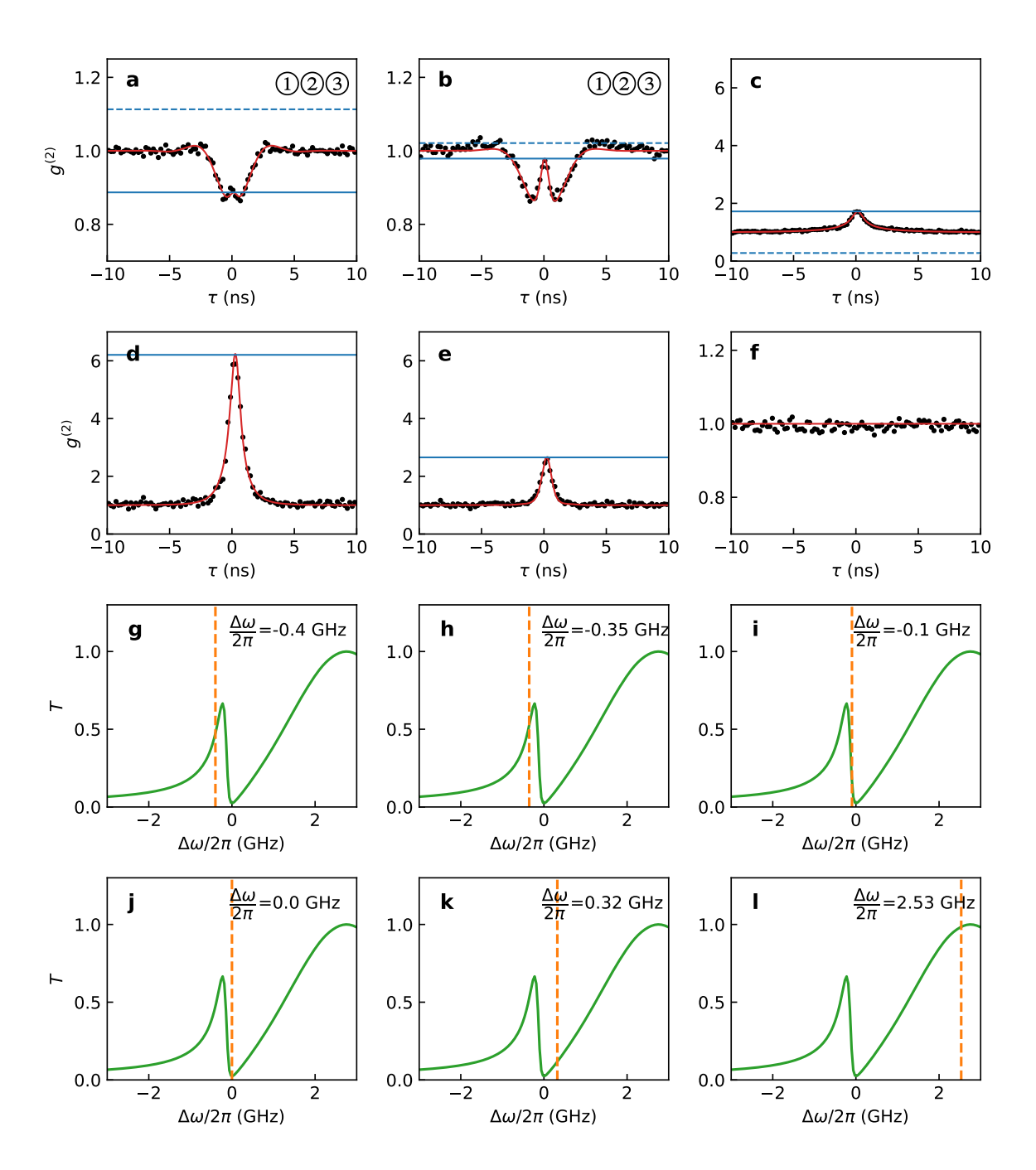


**Figure 6.5:** Photon statistics measured at various laser frequencies and at a fixed cavity detuning. **a-f**, The black dots represent the  $g^{(2)}$ -functions measured at laser frequencies marked by the dashed orange lines in **g-l**, respectively. The red solid lines display the theoretical fits to the measured data. The solid blue lines mark the levels of  $g^{(2)}(0)$  and the dashed blue lines indicate the levels of  $2 - g^{(2)}(0)$ . The annotations in the upper right corners denote the inequalities violated by the corresponding sets of data. **g-l**, Transmission spectra (green curves) and laser frequencies (dashed orange lines) for the measurements in **a-f**. Laser frequency detunings with respect to the molecule are noted in the upper right corner of each plot.

As the cavity detuning decreases ( $\mathbf{d}$ ,  $\mathbf{e}$ ,  $\mathbf{f}$ ), the  $g^{(2)}$ -functions fall within the bounds of all three inequalities and are thus classical. At an intermediate detuning ( $\mathbf{c}$ ), the signal peaks and shows slight bunching at zero time delay, but the third inequality is still violated since the antibunching exceeds the bounds set by the blue lines.

So far, we have studied the effects of the cavity detuning. A similar series of measurements is performed at a fixed cavity detuning but at different laser frequencies. Figure 6.5 displays the intensity-correlation functions measured when the molecule-cavity detuning is fixed at 2.57 GHz and the laser frequency is tuned from the red to the blue side of the lower-frequency transmission peak. In Fig. 6.5 a-f, we observe similar transitions of nonclassical to classical intensity fluctuations, as the laser frequency is tuned from the 'molecule'-like peak towards the 'cavity'-like one.

In summary, the observed intensity-correlation functions reveal the rich temporal dynamics in the molecule-cavity system. In contrast to the structural effects such as spectral modifications which can be modeled classically [61], the dynamic effects lead to nonclassical photon correlations, which is a result of pure quantum mechanical phenomena [60].

#### 6.3 Interfacing the molecule with single-photons

An efficiently coupled emitter-cavity system is promising for realizing quantum gates between an emitter and a photon, or between single photons [124, 137–139]. Although proof-of-principle demonstrations in this direction have been carried out [9, 125, 140], most of the experiments use attenuated laser pulses to mimic single antibunched photons. An explicit demonstration of this goal would require the efficient generation of two narrow-band single photons and their synchronized arrival at the emitter-cavity system. In this section, we demonstrate a further step towards this goal by coupling a stream of single photons to the molecule in the cavity.

We follow the methods described in Ref. [141] to generate frequency-tunable single photons from a second molecule. First, a DBT-doped anthracene crystal is prepared and placed on a fused-silica substrate. On the substrate, Indium-Tin-Oxide (ITO) electrodes are fabricated and arranged in an inter-digitated fashion, as displayed in Fig. 6.6 a. The spacing between an electrode and its neighboring counter-electrode is  $15 \,\mu\text{m}$ . The sample is cooled to  $1.4 \,\text{K}$  in a cryostat located in a neighboring lab. A DBT molecule ('source'-molecule) in the same frequency range as the molecule in the cavity ('target'-molecule) is identified through high-resolution spectroscopy and microscopy.

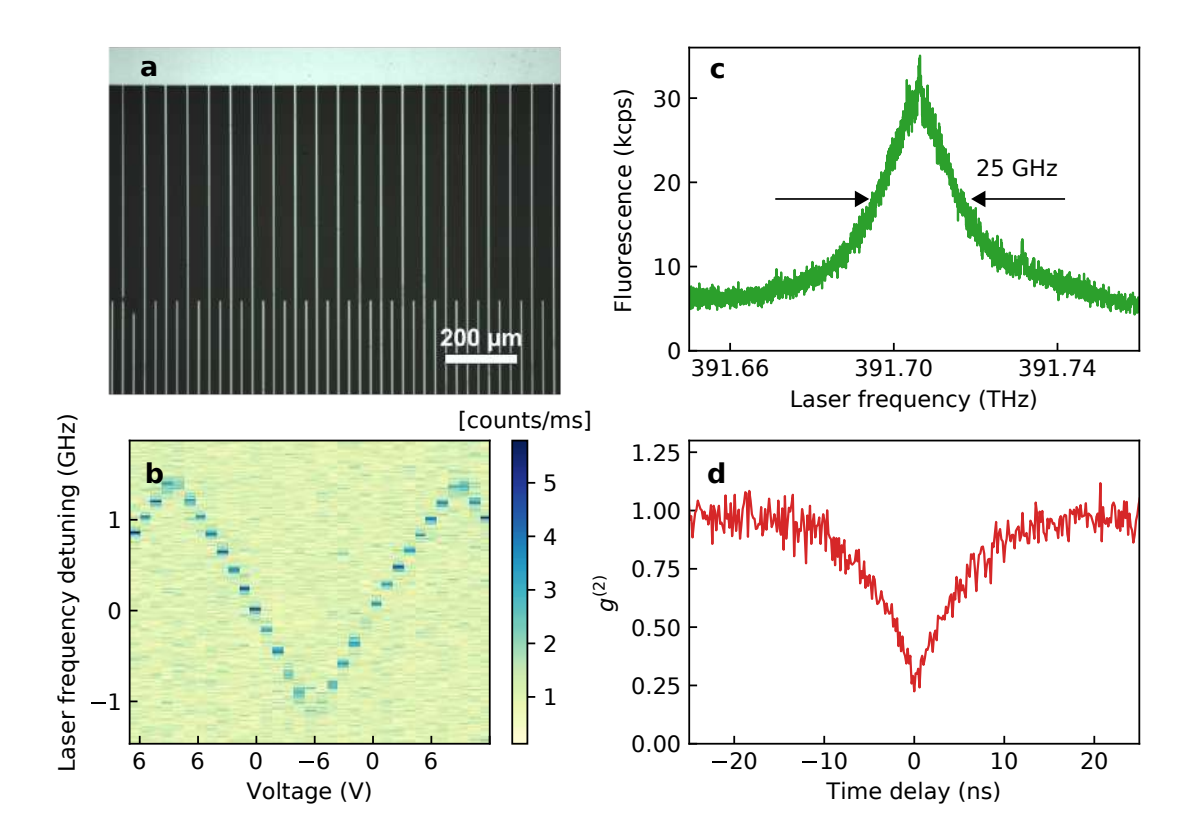


Figure 6.6: a, Optical microscope image of the interdigitated ITO electrodes on a fused silica substrate. The spacing between an electrode and its neighboring counter-electrode (lower part) is  $15\,\mu\mathrm{m}$ . b, Frequency tuning of the source-molecule. The horizontal axis shows the applied voltage in a triangular waveform. The vertical axis denotes the detuning of the laser frequency with respect to the target-molecule. The color bar presents the fluorescence count rates on the detector, in counts per millisecond. c, Fluorescence excitation spectrum of the source-molecule to a  $|e,v\neq 0\rangle$  level. d, Intensity autocorrelation measurement on the emitted 00ZPL photons.

The transition frequency of the source-molecule can be tuned using the DC Stark effect by applying a voltage to the electrodes. The fluorescence excitation spectra of the source molecule via its 00ZPL transition as a function of the applied voltage are displayed in Fig. 6.6 b, where the source molecule is tuned by 0.17 GHz/V in the frequency range (-1.2, 1.2) GHz with respect to the target-molecule. The linewidth of the transition is 41 MHz.

The source molecule is then excited to a higher vibronic level of its electronic excited state  $(|e, v \neq 0\rangle)$  using a Ti:sapphire laser. Its fluorescence emission is collected by an aspheric lens. A narrow bandpass filter is placed in the beam path to select the emission at the 00ZPL. Figure 6.6 c displays a fluorescence excitation spectrum of the vibronic level. About 30,000 counts per second are detected at the local optical table. An intensity autocorrelation measurement is performed on the 00ZPL emission to con-

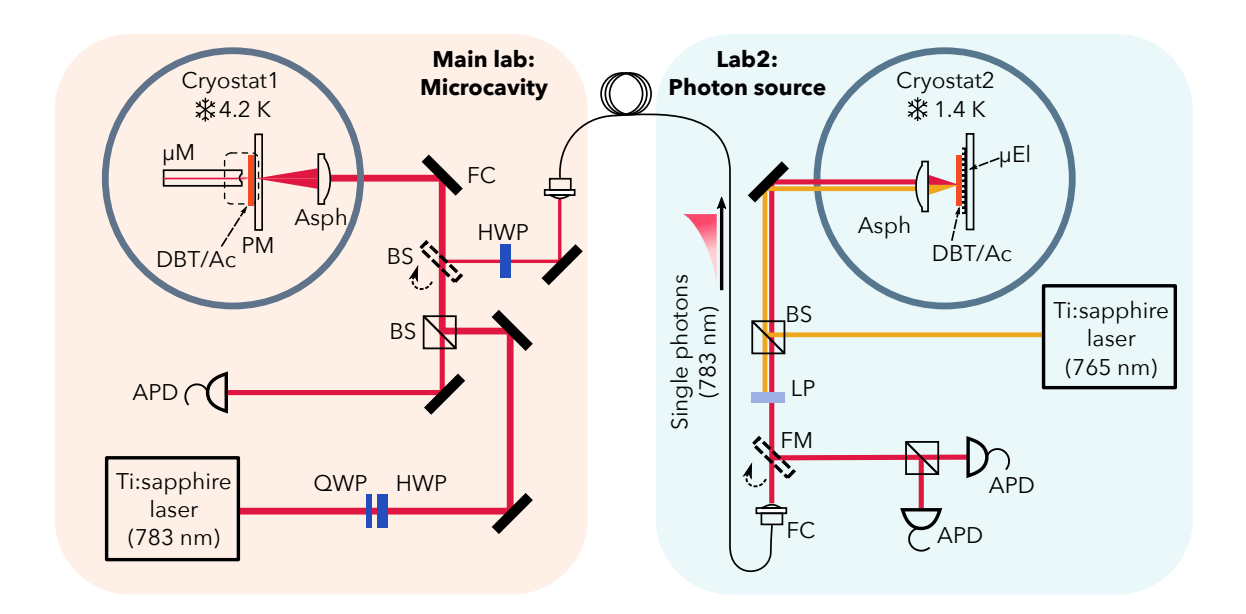
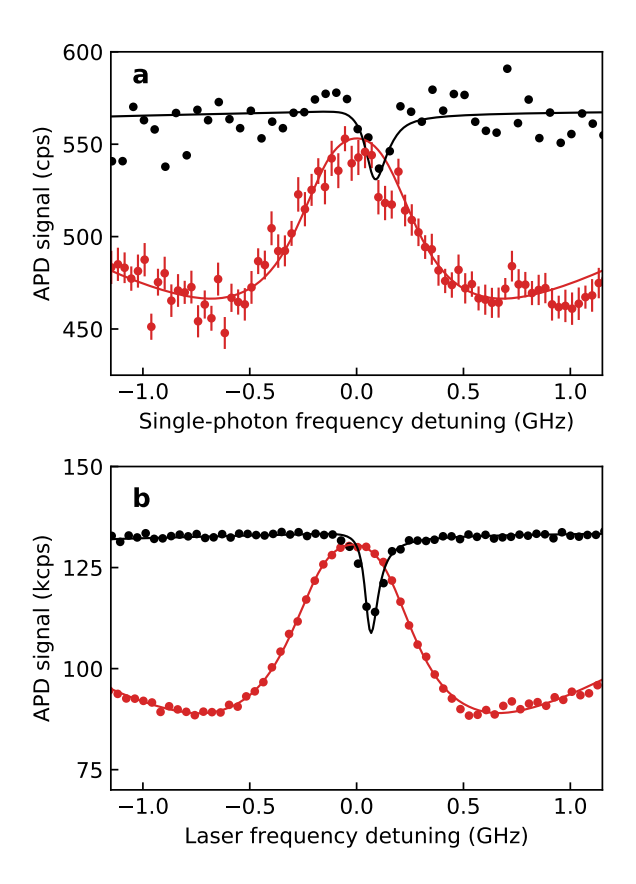


Figure 6.7: Schematic of the optical setup in the two labs. A second cryostat (Cryostat2) in a neighboring lab hosts the single-photon source. A stream of single photons emitted by the source-molecule is guided to the main lab hosting the microcavity via a single-mode fiber.  $\mu$ El: microelectrodes; DBT/Ac: anthracene crystal doped with DBT molecules; BS: beamsplitter; LP: long-pass filter; FM: flip mirror; FC: fiber coupler; Asph: aspheric lens; APD: avalanche photodiode; HWP: half-wave plate; QWP: quarter-wave plate; PM: planar mirror;  $\mu$ M: micromirror. See texts for details.

firm the single-photon nature of the detected fluorescence. The output is displayed in Fig. 6.6 d, where an antibunching at zero time delay with  $g^{(2)}(0) = 0.25$  confirms the purity of the photon source.

The single photons are then coupled into a single-mode fiber and guided to the microcavity experiment. The photons are coupled out of the fiber and sent through a half-wave plate which aligns their polarization to the cavity mode. A beam splitter then reflects 50% of the photons to the cryostat, where they are focused by the aspheric lens and coupled into the cavity. The reflected photons are collimated by the same aspheric lens and detected by an APD.

In the next step, we tune the frequency of the single-photons by applying a voltage to the electrodes. The red dots in Fig.  $6.8\,\mathrm{a}$  display the reflection spectrum of single-photons from the target-molecule. A peak in reflection with a width of about  $600\,\mathrm{MHz}$  is observed as a result of the efficient interaction of the single-photons with the target-molecule. Although the signal-to-noise ratio is lower, the observed signal shows the same trend as that presented in Fig.  $5.10\,\mathrm{c}$ . To calibrate the signal, we detune the cavity resonance to lower frequency by about  $5.5\,\mathrm{GHz}$ . The black dots in the same plot show the intensity of the single-photons reflected from the detuned cavity. Here,



**Figure 6.8: a**, Reflected intensity of the single-photons as a function of their frequency detuning with respect to the target-molecule. The red dots present the reflection spectrum from the resonantly-coupled molecule-cavity system. The black dots present the reflection spectrum when the cavity is detuned by 5.5 GHz from the target-molecule. The error bars indicate the shot noise. The solid lines show the theoretical fits considering a weak laser beam with a linewidth of 41 MHz. **b**, The same as in **a** but measured with a weak laser beam.

a notable dip appears at a slightly blue-shifted frequency with respect to the target-molecule. The small dip stems from destructive interference of the molecular scattering and the cavity field. At this detuning, a small Purcell factor (F = 3.3) is still present, thus the photons scattered by the target-molecule are captured with a high efficiency by the cavity mode and give rise to the reflection dip. The slight blue shift of the dip results from the cavity-modified Lamb shift discussed in chapter 5.6. A quantitative description is given by the theoretical fits shown by the solid lines. The fits follow Eq. 5.10 and consider a weak incoming laser beam with a linewidth of 41 MHz.

To further verify the observations in Fig. 6.8 a, we repeat the measurements using a weak laser beam. Figure 6.8 b presents the reflection spectra from the resonantly coupled (red) and cavity-detuned (black) systems measured by the weak laser beam, showing the same features as in a. We note that the depth and width of the dip in the

detuned spectrum somewhat differs from that measured by the single photons. The deviations originate from the linewidth difference of the single photons  $(41 \,\mathrm{MHz})$  and the laser beam  $(< 1 \,\mathrm{MHz})$ .

In summary, we have demonstrated a nearly perfect reflection of single antibunched photons by a single molecule enabled by the microcavity. In the next step, the source-molecule can be excited using a pulsed laser. The periodically spaced single-photons can be converted to two-photon pulses via temporal multiplexing [142]. Using this platform, exciting experiments such as single-photon pump-probe on a single molecule can be performed to further explore the limits of nonlinear optics.

# Chapter 7

#### Conclusion and outlook

In this thesis, we have demonstrated the strong modification of a single molecule's radiative properties by coupling it to an open and tunable microcavity at liquid helium temperatures. The resonant coupling to the cavity enhanced selectively the 00ZPL transition by a factor of  $\sim 40$ , thus changing its branching ratio from  $\sim 30\%$  to 95% and converting the molecule to a nearly ideal two-level system. The strong radiative enhancement also led to a nearly perfect coupling of the molecular emission to the cavity mode with  $\beta = 93\%$ . The highly efficient photon-emitter interaction gave rise to several unprecedented linear and nonlinear effects in molecular systems, such as 99% extinction of the cavity transmission, 66° phase shift of a laser beam as well as saturation with less than half a photon per lifetime and the generation of nonclassical few-photon states of light. Furthermore, we demonstrated efficient coupling of single molecular photons to the coupled system. Our achievements pave the way for building linear and nonlinear quantum photonic circuits based on organic platforms.

The established experimental platform is a suitable testbed for several further investigations:

1. It would be interesting to realize a single-molecule photon source which generates synchronized multi-photon states. The brightness of the current single-photon source can be improved by using a solid immersion lens [43] or a cryogenically compatible antenna structure [143]. The single-photon stream from the source molecule can be resorted using active temporal multiplexing [142] to allow synchronized incidences of two or more photons on the molecule. The system is then ready for demonstrating photon-photon interactions mediated by a single molecule, i.e. a single-photon 'pump-probe' experiment. This experiment will be a nonlinear optical experiment at its limit.

- 2. By structuring electrodes on the planar mirror, the resonance frequencies of single molecules in the cavity mode can be tuned with respect to each other. This will allow one to perform controlled studies of the interaction between two or more molecules mediated by the cavity mode. We expect to observe coherent dipole-dipole coupling in a two-molecule coupled system [144] and cooperative effects such as polaritonic states and light localization in a system with a controlled number of molecules [145, 146].
- 3. The open nature of the microcavity makes it suitable for integration with other species of solid-state emitters, such as rare earth ions (REIs) [18, 19, 21]. REIs are promising solid-state platforms for realizing a quantum memory with long coherence time [20, 147]. However, the electric dipole-forbidden nature of their intrashell-4f transitions leads to long excited-state lifetimes and thus low photon yields. For example, single Pr<sup>3+</sup> ions embedded in yttrium orthosilicate can be detected with only ~500 counts per second [19, 148]. By coupling them to the microcavity, the excited-stated lifetime can be reduced by up to 400 times, which will provide considerable count rate enhancement and at the same time make the radiative rates dominate over the effects of spectral broadening [148].

- [1] Waldman, G. Introduction to Light: The Physics of Light, Vision, and Color (Dover Publications, 2002).
- [2] Fox, M. Quantum Optics: An Introduction (Oxford University Press, 2006).
- [3] Demtröder, W. Laser Spectroscopy (Springer-Verlag Berlin Heidelberg, 2014).
- [4] Kimble, H. J. The quantum internet. *Nature* **453**, 1023–1030 (2008).
- [5] Cirac, J. I., Zoller, P., Kimble, H. J. & Mabuchi, H. Quantum state transfer and entanglement distribution among distant nodes in a quantum network. *Phys. Rev. Lett.* **78**, 3221–3224 (1997).
- [6] Volz, J. et al. Observation of entanglement of a single photon with a trapped atom. Phys. Rev. Lett. 96, 030404 (2006).
- [7] Wilk, T., Webster, S. C., Kuhn, A. & Rempe, G. Single-atom single-photon quantum interface. *Science* **317**, 488–490 (2007).
- [8] Ritter, S. et al. An elementary quantum network of single atoms in optical cavities. *Nature* **484**, 195–200 (2012).
- [9] Reiserer, A. & Rempe, G. Cavity-based quantum networks with single atoms and optical photons. *Rev. Mod. Phys.* 87, 1379–1418 (2015).
- [10] Blinov, B. B., Moehring, D. L., Duan, L.-M. & Monroe, C. Observation of entanglement between a single trapped atom and a single photon. *Nature* 428, 153–157 (2004).
- [11] Duan, L.-M. & Monroe, C. Colloquium: Quantum networks with trapped ions. Rev. Mod. Phys. 82, 1209–1224 (2010).
- [12] Stute, A. et al. Quantum-state transfer from an ion to a photon. Nat. Photon. 7, 219–222 (2013).

[13] Gao, W. B., Fallahi, P., Togan, E., Miguel-Sanchez, J. & Imamoglu, A. Observation of entanglement between a quantum dot spin and a single photon. *Nature* 491, 426–430 (2012).

- [14] Delley, Y. L., Kroner, M., Faelt, S., Wegscheider, W. & İmamoğlu, A. Deterministic entanglement between a propagating photon and a singlet-triplet qubit in an optically active quantum dot molecule. *Phys. Rev. B* **96**, 241410(R) (2017).
- [15] Togan, E. et al. Quantum entanglement between an optical photon and a solid-state spin qubit. Nature 466, 730–734 (2010).
- [16] Bernien, H. et al. Heralded entanglement between solid-state qubits separated by three metres. Nature 497, 86–90 (2013).
- [17] Sipahigil, A. et al. An integrated diamond nanophotonics platform for quantum-optical networks. Science **354**, 847–850 (2016).
- [18] Kolesov, R. et al. Optical detection of a single rare-earth ion in a crystal. Nat. Commun. 3, 1029 (2012).
- [19] Utikal, T. *et al.* Spectroscopic detection and state preparation of a single praseodymium ion in a crystal. *Nat. Commun.* **5**, 3627 (2014).
- [20] Zhong, M. et al. Optically addressable nuclear spins in a solid with a six-hour coherence time. Nature 517, 177–180 (2015).
- [21] Dibos, A. M., Raha, M., Phenicie, C. M. & Thompson, J. D. Atomic source of single photons in the telecom band. *Phys. Rev. Lett.* **120**, 243601 (2018).
- [22] Moerner, W., Orrit, M., Wild, U. & Basché, T. (eds.) Single-Molecule Optical Detection, Imaging and Spectroscopy (Wiley, 1996).
- [23] Lounis, B. & Orrit, M. Single-photon sources. Rep. Prog. Phys. 68, 1129–1179 (2005).
- [24] Aharonovich, I., Englund, D. & Toth, M. Solid-state single-photon emitters. *Nat. Photon.* **10**, 631–641 (2016).
- [25] Vahala, K. J. Optical microcavities. *Nature* **424**, 839–846 (2003).
- [26] Purcell, E. M. Proceedings of the American physical society. Phys. Rev. 69, 674–674 (1946).
- [27] Berman, P. R. (ed.) Cavity quantum electrodynamics (Academic Press, 1994).

[28] Haroche, S. & Raimond, J. Exploring the Quantum: Atoms, Cavities, and Photons (Oxford University Press, 2006).

- [29] Madsen, K. H. *et al.* Efficient out-coupling of high-purity single photons from a coherent quantum dot in a photonic-crystal cavity. *Phys. Rev. B* **90**, 155303 (2014).
- [30] Grange, T. et al. Cavity-funneled generation of indistinguishable single photons from strongly dissipative quantum emitters. Phys. Rev. Lett. 114, 193601 (2015).
- [31] Somaschi, N. et al. Near-optimal single-photon sources in the solid state. Nat. Photon. 10, 340–345 (2016).
- [32] Bogdanović, S. et al. Robust nano-fabrication of an integrated platform for spin control in a tunable microcavity. APL Photonics 2, 126101 (2017).
- [33] Riedel, D. et al. Deterministic enhancement of coherent photon generation from a nitrogen-vacancy center in ultrapure diamond. Phys. Rev. X 7, 031040 (2017).
- [34] Walther, H., Varcoe, B. T. H., Englert, B.-G. & Becker, T. Cavity quantum electrodynamics. *Rep. Prog. Phys.* **69**, 1325–1382 (2006).
- [35] Kimble, H. J. Strong interactions of single atoms and photons in cavity QED. *Phys. Scr.* **T76**, 127–137 (1998).
- [36] Klessinger, M. & Michl, J. Excited states and photochemistry of organic molecules (Wiley-VCH, 1995).
- [37] Toninelli, C. et al. Near-infrared single-photons from aligned molecules in ultrathin crystalline films at room temperature. Opt. Express 18, 6577–6582 (2010).
- [38] Kasha, M. Characterization of electronic transitions in complex molecules. *Discuss. Faraday Soc.* **9**, 14–19 (1950).
- [39] Franck, J. & Dymond, E. G. Elementary processes of photochemical reactions. Trans. Faraday Soc. 21, 536–542 (1926).
- [40] Condon, E. A theory of intensity distribution in band systems. *Phys. Rev.* **28**, 1182–1201 (1926).
- [41] Nicolet, A. A. L. *et al.* Single dibenzoterrylene molecules in an anthracene crystal: Main insertion sites. *ChemPhysChem* **8**, 1929–1936 (2007).
- [42] Vogel, W. & Welsch, D.-G. Quantum optics (WILEY-VCH, 2006).

[43] Maser, A. J. Few-photon coherent nonlinear optics with a single molecule. Doctoral Thesis, Friedrich-Alexander-Universität Erlangen-Nürnberg (2017).

- [44] Türschmann, P. Coherent Coupling of Single Organic Dye Molecules to Optical Nanoguides. Doctoral Thesis, Friedrich-Alexander-Universität Erlangen-Nürnberg (2018).
- [45] Einstein, A. Strahlungs-emission und absorption nach der quantentheorie. Verhandlungen der Deutsche Physikalische Gesellschaft 18, 318–323 (1916).
- [46] Loudon, R. The Quantum Theory of Light (Oxford University Press, 2000).
- [47] Milonni, P. W. The Quantum Vacuum: An Introduction to Quantum Electrodynamics (Academic Press, 1994).
- [48] Sauvan, C., Hugonin, J. P., Maksymov, I. S. & Lalanne, P. Theory of the spontaneous optical emission of nanosize photonic and plasmon resonators. *Phys. Rev. Lett.* **110**, 237401 (2013).
- [49] Petermann, K. Calculated spontaneous emission factor for doubleheterostructure injection lasers with gain-induced waveguiding. *IEEE J. Quan*tum Electron. 15, 566–570 (1979).
- [50] Choi, Y. et al. Quasieigenstate coalescence in an atom-cavity quantum composite. Phys. Rev. Lett. 104, 153601 (2010).
- [51] Auffèves-Garnier, A., Simon, C., Gérard, J. M. & Poizat, J. P. Giant optical nonlinearity induced by a single two-level system interacting with a cavity in the Purcell regime. *Phys. Rev. A* **75**, 053823 (2007).
- [52] Nicolet, A. A. L., Hofmann, C., Kol'chenko, M. A., Kozankiewicz, B. & Orrit, M. Single dibenzoterrylene molecules in an anthracene crystal: Spectroscopy and photophysics. *ChemPhysChem* 8, 1215–1220 (2007).
- [53] Fano, U. Effects of configuration interaction on intensities and phase shifts. Phys. Rev. 124, 1866–1878 (1961).
- [54] Heinzen, D. J. & Feld, M. S. Vacuum radiative level shift and spontaneousemission linewidth of an atom in an optical resonator. *Phys. Rev. Lett.* 59, 2623–2626 (1987).
- [55] Lamb, W. E. & Retherford, R. C. Fine structure of the hydrogen atom by a microwave method. *Phys. Rev.* **72**, 241–243 (1947).

[56] Reiserer, A., Ritter, S. & Rempe, G. Nondestructive detection of an optical photon. *Science* **342**, 1349–1351 (2013).

- [57] Stobińska, M., Alber, G. & Leuchs, G. Perfect excitation of a matter qubit by a single photon in free space. *Europhys. Lett.* **86**, 14007 (2009).
- [58] Carmichael, H. J. Photon antibunching and squeezing for a single atom in a resonant cavity. *Phys. Rev. Lett.* **55**, 2790–2793 (1985).
- [59] Rice, P. R. & Carmichael, H. J. Single-atom cavity-enhanced absorption I: Photon statistics in the bad-cavity limit. *IEEE J. Quantum Electron.* 24, 1351–1366 (1988).
- [60] Carmichael, H. J. & Rice, P. R. Quantum interference and collapse of the wavefunction in cavity QED. Opt. Commun. 82, 73–79 (1991).
- [61] Zhu, Y. et al. Vacuum Rabi splitting as a feature of linear-dispersion theory: Analysis and experimental observations. Phys. Rev. Lett. 64, 2499–2502 (1990).
- [62] Schwoerer, M. & Wolf, H. C. Purification of Materials, Crystal Growth and Preparation of Thin Films (Wiley-VCH, 2008).
- [63] Nakada, I. The optical properties of anthracene single crystals. J. Phys. Soc. Jpn. 17, 113–118 (1962).
- [64] Wang, D. et al. Coherent coupling of a single molecule to a scanning fabry-perot microcavity. Phys. Rev. X 7, 021014 (2017).
- [65] Orrit, M. & Bernard, J. Single pentacene molecules detected by fluorescence excitation in a p-terphenyl crystal. *Phys. Rev. Lett.* **65**, 2716–2719 (1990).
- [66] Raimond, J. M., Brune, M. & Haroche, S. Manipulating quantum entanglement with atoms and photons in a cavity. *Rev. Mod. Phys.* **73**, 565–582 (2001).
- [67] Thompson, R. J., Rempe, G. & Kimble, H. J. Observation of normal-mode splitting for an atom in an optical cavity. *Phys. Rev. Lett.* **68**, 1132–1135 (1992).
- [68] Rempe, G., Thompson, R. J., Kimble, H. J. & Lalezari, R. Measurement of ultralow losses in an optical interferometer. *Opt. Lett.* **17**, 363–365 (1992).
- [69] Hood, C. J., Kimble, H. J. & Ye, J. Characterization of high-finesse mirrors: Loss, phase shifts, and mode structure in an optical cavity. *Phys. Rev. A* 64, 033804 (2001).
- [70] Gérard, J. M. et al. Enhanced spontaneous emission by quantum boxes in a monolithic optical microcavity. Phys. Rev. Lett. 81, 1110–1113 (1998).

[71] Reithmaier, J. P. *et al.* Strong coupling in a single quantum dot–semiconductor microcavity system. *Nature* **432**, 197–200 (2004).

- [72] Yoshie, T. *et al.* Vacuum rabi splitting with a single quantum dot in a photonic crystal nanocavity. *Nature* **432**, 200–203 (2004).
- [73] Senellart, P., Solomon, G. & White, A. High-performance semiconductor quantum-dot single-photon sources. *Nat. Nanotech.* **12**, 1026–1039 (2017).
- [74] Steinmetz, T. et al. Stable fiber-based fabry-pérot cavity. Appl. Phys. Lett. 89, 111110 (2006).
- [75] Hunger, D. et al. A fiber Fabry–Perot cavity with high finesse. New J. Phys. 12, 065038 (2010).
- [76] Hunger, D., Deutsch, C., Barbour, R. J., Warburton, R. J. & Reichel, J. Laser micro-fabrication of concave, low-roughness features in silica. AIP Advances 2, 012119 (2012).
- [77] Toninelli, C. et al. A scanning microcavity for in situ control of single-molecule emission. Appl. Phys. Lett. 97, 021107 (2010).
- [78] Dolan, P. R., Hughes, G. M., Grazioso, F., Patton, B. R. & Smith, J. M. Femtoliter tunable optical cavity arrays. *Opt. Lett.* **35**, 3556–3558 (2010).
- [79] Kelkar, H. et al. Sensing nanoparticles with a cantilever-based scannable optical cavity of low finesse and sub- $\lambda^3$  volume. Phys. Rev. Applied 4, 054010 (2015).
- [80] Muller, A., Flagg, E. B., Metcalfe, M., Lawall, J. & Solomon, G. S. Coupling an epitaxial quantum dot to a fiber-based external-mirror microcavity. *Appl. Phys. Lett.* **95**, 173101 (2009).
- [81] Miguel-Sánchez, J. et al. Cavity quantum electrodynamics with charge-controlled quantum dots coupled to a fiber fabry–perot cavity. New J. Phys. 15, 045002 (2013).
- [82] Greuter, L., Starosielec, S., Kuhlmann, A. V. & Warburton, R. J. Towards high-cooperativity strong coupling of a quantum dot in a tunable microcavity. *Phys. Rev. B* **92**, 045302 (2015).
- [83] Johnson, S. *et al.* Tunable cavity coupling of the zero phonon line of a nitrogen-vacancy defect in diamond. *New J. Phys.* **17**, 122003 (2015).

[84] Albrecht, R. et al. Narrow-band single photon emission at room temperature based on a single nitrogen-vacancy center coupled to an all-fiber-cavity. Appl. Phys. Lett. 105, 073113 (2014).

- [85] Kaupp, H. et al. Purcell-enhanced single-photon emission from nitrogen-vacancy centers coupled to a tunable microcavity. Phys. Rev. Applied 6, 054010 (2016).
- [86] Benedikter, J. et al. Cavity-enhanced single-photon source based on the siliconvacancy center in diamond. *Phys. Rev. Applied* 7, 024031 (2017).
- [87] Vallance, C., Trichet, A. A. P., James, D., Dolan, P. R. & Smith, J. M. Open-access microcavities for chemical sensing. *Nanotechnology* **27**, 274003 (2016).
- [88] Mader, M., Reichel, J., Hänsch, T. W. & Hunger, D. A scanning cavity microscope. *Nat. Commun.* **6**, 7249 (2015).
- [89] Hümmer, T. et al. Cavity-enhanced raman microscopy of individual carbon nanotubes. Nat. Commun. 7, 12155 (2016).
- [90] Casabone, B. et al. Cavity-enhanced spectroscopy of a few-ion ensemble in  $Eu^{3+}:Y_2O_3$ . New J. Phys. **20**, 095006 (2018).
- [91] Aspelmeyer, M., Kippenberg, T. J. & Marquardt, F. Cavity optomechanics. Rev. Mod. Phys. 86, 1391–1452 (2014).
- [92] Muller, A., Flagg, E. B., Lawall, J. R. & Solomon, G. S. Ultrahigh-finesse, low-mode-volume Fabry-Perot microcavity. *Opt. Lett.* **35**, 2293–2295 (2010).
- [93] Orloff, J., Swanson, L. & Utlaut, M. High Resolution Focused Ion Beams: FIB and its Applications (Springer US, 2003).
- [94] Trichet, A. A. P., Dolan, P. R., Coles, D. M., Hughes, G. M. & Smith, J. M. Topographic control of open-access microcavities at the nanometer scale. Opt. Express 23, 17205–17216 (2015).
- [95] Pellerin, J. G., Griffis, D. P. & Russell, P. E. Focused ion beam machining of Si, GaAs, and InP. J. Vac. Sci. Tech. B 8, 1945–1950 (1990).
- [96] Hung, N., Fu, Y. & Ali, M. Focused ion beam machining of silicon. J. Mater. Process. Tech. 127, 256 – 260 (2002).
- [97] Slocum, A. Kinematic couplings: A review of design principles and applications. *Int. J. Mach. Tool. Manu.* **50**, 310–327 (2010).
- [98] Hansch, T. W. & Couillaud, B. Laser frequency stabilization by polarization spectroscopy of a reflecting reference cavity. *Opt. Commun.* **35**, 441–444 (1980).

[99] Harry, G., Bodiya, T. & DeSalvo, R. Optical Coatings and Thermal Noise in Precision Measurement (Cambridge University Press, 2012).

- [100] Vollmer, F. & Yang, L. Review label-free detection with high-Q microcavities: a review of biosensing mechanisms for integrated devices. *Nanophotonics* 1, 267– 291 (2012).
- [101] Bennett, H. E. & Porteus, J. O. Relation between surface roughness and specular reflectance at normal incidence. J. Opt. Soc. Am. 51, 123–129 (1961).
- [102] Svelto, O. Principles of Lasers (Springer US, 2010).
- [103] Silfvast, W. Laser Fundamentals (Cambridge University Press, 2008).
- [104] Greuter, L. et al. A small mode volume tunable microcavity: Development and characterization. Appl. Phys. Lett. 105, 121105 (2014).
- [105] Arnold, S., Khoshsima, M., Teraoka, I., Holler, S. & Vollmer, F. Shift of whispering-gallery modes in microspheres by protein adsorption. Opt. Lett. 28, 272–274 (2003).
- [106] Baaske, M. D., Foreman, M. R. & Vollmer, F. Single-molecule nucleic acid interactions monitored on a label-free microcavity biosensor platform. *Nat. Nanotech.* 9, 933–939 (2014).
- [107] Newton, R. Scattering Theory of Waves and Particles (Springer-Verlag Berlin Heidelberg, 1982).
- [108] Koenderink, A. F., Kafesaki, M., Buchler, B. C. & Sandoghdar, V. Controlling the resonance of a photonic crystal microcavity by a near-field probe. *Phys. Rev. Lett.* **95**, 153904 (2005).
- [109] Håkanson, U. et al. Coupling of plasmonic nanoparticles to their environments in the context of van der Waals-Casimir interactions. Phys. Rev. B 77, 155408 (2008).
- [110] Pinchuk, A., Hilger, A., Plessen, G. v. & Kreibig, U. Substrate effect on the optical response of silver nanoparticles. *Nanotechnology* **15**, 1890–1896 (2004).
- [111] Wokaun, A., Gordon, J. P. & Liao, P. F. Radiation damping in surface-enhanced raman scattering. *Phys. Rev. Lett.* **48**, 957–960 (1982).
- [112] Ruesink, F., Doeleman, H. M., Hendrikx, R., Koenderink, A. F. & Verhagen, E. Perturbing open cavities: Anomalous resonance frequency shifts in a hybrid cavity-nanoantenna system. *Phys. Rev. Lett.* 115, 203904 (2015).

[113] Lee, K. G. *et al.* A planar dielectric antenna for directional single-photon emission and near-unity collection efficiency. *Nat. Photon.* **5**, 166–169 (2011).

- [114] Trebbia, J.-B., Ruf, H., Tamarat, P. & Lounis, B. Efficient generation of near infra-red single photons from the zero-phonon line of a single molecule. *Opt. Express* 17, 23986–23991 (2009).
- [115] Olivero, J. & Longbothum, R. Empirical fits to the Voigt line width: A brief review. J. Quant. Spectrosc. Radiat. Transf. 17, 233–236 (1977).
- [116] Pazzagli, S. et al. Self-assembled nanocrystals of polycyclic aromatic hydrocarbons show photostable single-photon emission. ACS Nano 12, 4295–4303 (2018).
- [117] Wrigge, G., Gerhardt, I., Hwang, J., Zumofen, G. & Sandoghdar, V. Efficient coupling of photons to a single molecule and the observation of its resonance fluorescence. *Nat. Phys.* 4, 60–66 (2008).
- [118] Scully, M. & Zubairy, M. Quantum Optics (Cambridge University Press, 1997).
- [119] Khitrova, G., Gibbs, H. M., Kira, M., Koch, S. W. & Scherer, A. Vacuum Rabi splitting in semiconductors. *Nat. Phys.* **2**, 81–90 (2006).
- [120] Aljunid, S. A. et al. Phase shift of a weak coherent beam induced by a single atom. Phys. Rev. Lett. 103, 153601 (2009).
- [121] Hétet, G., Slodička, L., Röck, N. & Blatt, R. Free-space read-out and control of single-ion dispersion using quantum interference. *Phys. Rev. A* 88, 041804 (2013).
- [122] Fischer, M. et al. Shifting the phase of a coherent beam with a <sup>174</sup>Yb<sup>+</sup> ion: influence of the scattering cross section. Appl. Phys. B **123**, 48 (2017).
- [123] Pototschnig, M. et al. Controlling the phase of a light beam with a single molecule. Phys. Rev. Lett. 107, 063001 (2011).
- [124] Duan, L.-M. & Kimble, H. J. Scalable photonic quantum computation through cavity-assisted interactions. *Phys. Rev. Lett.* **92**, 127902 (2004).
- [125] Tiecke, T. G. et al. Nanophotonic quantum phase switch with a single atom. Nature 508, 241–244 (2014).
- [126] Turchette, Q. A., Hood, C. J., Lange, W., Mabuchi, H. & Kimble, H. J. Measurement of conditional phase shifts for quantum logic. *Phys. Rev. Lett.* 75, 4710–4713 (1995).

- [127] Boyd, R. W. Nonlinear Optics (Academic Press, 2008).
- [128] Chang, D. E., Vuletić, V. & Lukin, M. D. Quantum nonlinear optics photon by photon. *Nat. Photon.* **8**, 685–694 (2014).
- [129] Maser, A., Gmeiner, B., Utikal, T., Götzinger, S. & Sandoghdar, V. Few-photon coherent nonlinear optics with a single molecule. *Nat. Photon.* 10, 450–453 (2016).
- [130] Shen, J.-T. & Fan, S. Strongly correlated two-photon transport in a onedimensional waveguide coupled to a two-level system. *Phys. Rev. Lett.* 98, 153003 (2007).
- [131] Witthaut, D., Lukin, M. D. & Sørensen, A. S. Photon sorters and QND detectors using single photon emitters. *Europhys. Lett.* **97**, 50007 (2012).
- [132] Ralph, T. C., Söllner, I., Mahmoodian, S., White, A. G. & Lodahl, P. Photon sorting, efficient bell measurements, and a deterministic controlled-Z gate using a passive two-level nonlinearity. *Phys. Rev. Lett.* **114**, 173603 (2015).
- [133] Snijders, H. et al. Purification of a single-photon nonlinearity. Nat. Commun. 7, 12578 (2016).
- [134] Bennett, A. J. et al. A semiconductor photon-sorter. Nat. Nanotech. 11, 857–860 (2016).
- [135] Javadi, A. et al. Single-photon non-linear optics with a quantum dot in a waveguide. Nat. Commun. 6, 8655 (2015).
- [136] Paul, H. Photon antibunching. Rev. Mod. Phys. 54, 1061–1102 (1982).
- [137] Kok, P. & Lovett, B. Introduction to Optical Quantum Information Processing (Cambridge University Press, 2010).
- [138] Hwang, J. & Hinds, E. A. Dye molecules as single-photon sources and large optical nonlinearities on a chip. New J. Phys. 13, 085009 (2011).
- [139] Nysteen, A., McCutcheon, D. P. S., Heuck, M., Mørk, J. & Englund, D. R. Limitations of two-level emitters as nonlinearities in two-photon controlled-phase gates. *Phys. Rev. A* 95, 062304 (2017).
- [140] Hacker, B., Welte, S., Rempe, G. & Ritter, S. A photon–photon quantum gate based on a single atom in an optical resonator. *Nature* **536**, 193–196 (2016).
- [141] Rezus, Y. L. A. et al. Single-photon spectroscopy of a single molecule. Phys. Rev. Lett. 108, 093601 (2012).

[142] Wang, H. et al. High-efficiency multiphoton boson sampling. Nat. Photon. 11, 361–365 (2017).

- [143] Chen, X.-W., Götzinger, S. & Sandoghdar, V. 99% efficiency in collecting photons from a single emitter. *Opt. Lett.* **36**, 3545–3547 (2011).
- [144] Hettich, C. *et al.* Nanometer resolution and coherent optical dipole coupling of two individual molecules. *Science* **298**, 385–389 (2002).
- [145] Diniz, I. et al. Strongly coupling a cavity to inhomogeneous ensembles of emitters: Potential for long-lived solid-state quantum memories. Phys. Rev. A 84, 063810 (2011).
- [146] Haakh, H. R., Faez, S. & Sandoghdar, V. Polaritonic normal-mode splitting and light localization in a one-dimensional nanoguide. *Phys. Rev. A* 94, 053840 (2016).
- [147] Afzelius, M. et al. Demonstration of atomic frequency comb memory for light with spin-wave storage. Phys. Rev. Lett. 104, 040503 (2010).
- [148] Eichhammer, E., Utikal, T., Götzinger, S. & Sandoghdar, V. Spectroscopic detection of single Pr<sup>3+</sup> ions on the <sup>3</sup>H<sub>4</sub>-<sup>1</sup>D<sub>2</sub> transition. New J. Phys. **17**, 083018 (2015).

# Acknowledgement

I would like to express my thanks to all the people who have supported me in the past five and a half years. This experiment has been long and often stressful. Its success would have not been possible without your supports.

First, I am very grateful to my supervisor, Vahid, who guided me through this work. His creative and enthusiastic mind has influenced me deeply. I will take on the 'Sandoghdar'-spirit I gained over these years in my career.

Working with Hrishi, my lab supervisor, was one of the luckiest experience I had. He introduced me to this experiment and contributed enormously to its success. He is always calm and has 'in-pocket' solutions to the problems in the lab. Hi Hrishi, it was a great experience!

I would like to thank Stephan, for helping me debugging the countless problems and ease my mental stresses. A thank you to Tobi, who managed excellently the lab facilities and kept every instrument in its place; a big thanks to Diego, from whom we gained insightful theoretical understandings of this project; to Maks, who took his time for every tiny and fine mechanical pieces in the cryostat.

A thank you to Rich, Liu, Matt, Eugene, Nama, Korenobu... for making my time out of the lab also enjoyable.

A thank you to all the nanos, for constructing a warm and stimulating working environment and for all the free smiles I got every morning! It was so great to be a part of you!

### **Appendix**

#### **Numerical simulations**

The cavity mode profiles presented in Fig. 4.3 of this thesis are obtained by performing full-numerical simulations (COMSOL Multiphysics) considering a Gaussian excitation profile on the planar mirror. The simulation box has a length of  $7\lambda$ , which is surrounded by perfect matched layers and scattering boundary conditions. The typical mesh sizes are below  $\lambda/10$  close to the two mirrors and  $\lambda/4$  in other regions. To treat the extensive number of degrees of freedom arising from the layered-dielectric structure, symmetry of the linearly polarized cavity mode is imposed by calculating a quarter of the cavity volume with perfect electric and perfect magnetic conductor boundary conditions. The mesh size within the dielectric layers is chosen to be as small as  $\lambda/35$ .

To determine the mode volume of the cavity, we use the definition of V given in Ref. [48] which is derived based on the concept of quasinormal modes. This formulation solves the problem of the divergence of lossy eigenmodes and the ambiguity of the integration over the simulation volume. It also correctly recovers the well-known Purcell formula,  $F = (3/4\pi^2)(\lambda/n)^3 \text{Re}(Q/V)$ , i.e. the emission enhancement due to a single lossy mode with respect to an isotropic medium of refractive index n. The mode volume has the following definition

$$V = \int_{\forall V \in \text{ simulation}} \frac{\epsilon_0 \mathbf{E}(\mathbf{r}) \overline{\epsilon}(\mathbf{r}) \mathbf{E}(\mathbf{r}) - \mu_0 \mathbf{H}(\mathbf{r}) \mathbf{H}(\mathbf{r})}{2\epsilon_0 n^2 [\mathbf{E}(\mathbf{r_0}) \cdot \mathbf{u}]^2} d\mathbf{r}^3, \tag{1}$$

where  $\epsilon(\mathbf{r})$ ,  $\mathbf{E}(\mathbf{r})$  and  $\mathbf{H}(\mathbf{r})$  stand for the electric permittivity, electric and magnetic fields at point  $\mathbf{r}$  in the simulation volume, respectively.  $\mu_0$  represents the vacuum permeability. n is the refractive index of the medium inside the cavity.  $\mathbf{r_0}$  denotes the position of the emitter and  $\mathbf{u}$  is a unit vector pointing in the direction of the emitter.